Evaluation of Location Sharing Networks and Wearable-based Human Activity Recognition to Improve Occupational Safety in Forestry

A Dissertation
Presented in Partial Fulfillment of the Requirements for the
Degree of Doctor of Philosophy
with a
Major in Natural Resources
in the
College of Graduate Studies
University of Idaho
by
Eloise G. Zimbelman

Approved by:
Major Professor: Robert F. Keefe, Ph.D.
Committee Members: Crystal A. Kolden, Ph.D.; Eva K. Strand, Ph.D.; Lee A. Vierling, Ph.D.
Department Administrator: P. Charles Goebel, Ph.D.

May 2022

Abstract

Availability of real-time location sharing devices that use global navigation satellite system (GNSS) positioning paired with radio frequency (RF) transmission (GNSS-RF) and wearable devices equipped with inertial measurement unit (IMU) and other sensors provide opportunities to improve occupational safety in forestry using new techniques and methodologies based on human activity recognition. Forestry is among the most hazardous professions in the United States. In particular, logging and wildland firefighting occur in remote, off-grid environments that often lack traditional cellular communications infrastructure and involve frequent interactions among ground workers, heavy equipment, and dynamic terrain- and weather-related hazards. GNSS-RF location sharing, geofencing, mesh networking, and wearable-based human activity recognition modeling can increase situational awareness (SA) among these workers. The overall goals of this dissertation are to assess the factors affecting the performance and accuracy of a variety of location sharing networks and to demonstrate the feasibility of using wearable sensors to quantify forestry work activities. The work consists of four chapters. In the first, I develop the concept of GNSS-RF mobile geofences and model the intersections of mobile and stationary geofences in order to characterize the factors affecting the timing of intersection alerts. This field study provides the basis for evaluating the feasibility of using real-time safe work areas and incident avoidance alert systems for person-to-person and machine-to-machine interactions in dynamic forestry environments. The second chapter evaluates the effects of forest stand characteristics, topography, and line-of-sight (LOS) obstructions on radio signal propagation, positional accuracy, and geofence alert timing using a network of GNSS-RF transponders. The third chapter assesses the overall performance of smartphone-based GNSS-RF mesh networks and develops Dirichlet regression models to predict network connectivity using lidar and satellite remote sensing data. In the final chapter, I present the first use of wearable sensors to develop human activity recognition models that quantify occupational work in forestry using machine learning. Collectively, this research provides the basis for using real-time GNSS-RF based location sharing, geofencing, and wearable-based human activity recognition systems to improve SA and inform smart alerts to reduce fatal and near-fatal incidents among natural resource professionals.

Acknowledgments

Thank you to my major professor, Dr. Robert F. Keefe, for your dedication to mentoring and advising me throughout this process. Your enthusiasm for research has inspired me to continue developing into an independent scholar and your guidance, expertise, and commitment to student success are much appreciated. My gratitude extends to my graduate committee members: Drs. Crystal Kolden, Eva Strand, and Lee Vierling. Thank you all for providing guidance and helpful feedback. Many thanks to my friends and community in Moscow for making my time in graduate school so memorable.

I would also like to thank everyone who assisted with various aspects of field work throughout this research. Simone Cox and Lucas Moura de Abreu supported the field experiment in Chapter 2; Molly Rard, Rebecca Ramsey, Kevin Cannon, and Andrew Naughton aided in experiment setup, stand inventory, and data collection for Chapter 3; and my father, David Zimbelman, my partner, Tim Bak, and Ryer Becker provided valuable assistance with sampling for Chapter 4. This work would also not have been possible without the private landowners who provided access to their land for data collection for Chapter 4, as well as the support of state and regional industrial timberland owners and the loggers who participated in the sampling for Chapter 5.

Lastly, I extend my gratitude to the programs whose financial support made this research possible: the U.S. Centers for Disease Control and Prevention (CDC) National Institute for Occupational Safety and Health (NIOSH) grant number 5 U01 OH010841; and the University of Washington Pacific Northwest Agricultural Safety and Health (PNASH) Center Pilot Project subaward number UWSC10722.

Dedication

I dedicate this dissertation to my friends and family for their support and encouragement. Special thanks to my parents for instilling in me the value of an education and for their continued support of my academic pursuits. And to my partner, Tim, for always believing in me and providing reassurance and encouragement.

Table of Contents

List of Tables

List of Figures

Statement of Contribution

Eloise G. Zimbelman was primarily responsible for study design, planning, investigation, data collection and analysis, and manuscript completion for the research studies presented in this dissertation. Co-authors contributed to Chapter 2 by providing feedback and support during primary manuscript preparation. Dr. Keefe contributed to procuring funding and initial project planning for all research conducted during this dissertation and assisted with primary manuscript editing efforts.

Chapter 1: Introduction

1.1 Logging and Wildland Firefighter Safety

Farming, fishing, and forestry occupations are among the most hazardous occupations in the United States, with fatal work injury rates ranging from 20.9 to 27.0 cases per 100,000 full-time equivalent workers between 2010 and 2020 (U.S. Bureau of Labor Statistics 2021). With between 68.9 and 135.9 fatal occupational injuries per 100,000 full-time equivalent workers between 2010 and 2020, logging is particularly dangerous. As a result, logging is consistently ranked as one of the most dangerous occupations in the United States, with the highest fatal work injury rate from 2012 to 2016 and in 2018 and the second highest fatal work injury rate in 2010, 2011, 2017, 2019, and 2020 (Figure 1.1). Fosbroke et al. (1997) performed an in-depth analysis of national fatality data from the National Institute for Occupational Safety and Health (NIOSH) National Traumatic Occupational Fatalities (NTOF) surveillance system (Fosbroke et al. 1997). They calculated the lifetime risks for the most hazardous occupations in the United States and found logging to have the highest risk of fatal injury (Fosbroke et al. 1997). Some dangers associated with timber harvesting stem from the hazards posed by adverse weather and uneven terrain (Sygnatur 1998), but many injuries result from being struck by objects such as trees, limbs, or machines as well as exertion (Lefort et al. 2003). While the increasing mechanization of logging has contributed to a decrease in injury rates (Axelsson 1998; Bell 2002; Bonauto et al. 2019), ground crew members working alongside equipment, hand fallers manually felling trees with chainsaws, and choker setters working on cable logging operations remain at high risk (Shaffer and Milburn 1999; Lefort et al. 2003; Lagerstrom et al. 2017). In particular, logging in the Inland Northwest often occurs on steep slopes and necessitates the use of cable systems (Keefe et al. 2014a), which creates numerous high-risk safety situations such as manual felling, the potential for rolling logs, and the close proximity of ground crews and heavy equipment. Many cable logging accidents are the result of low visibility between yarder operators and the ground crew (Keefe and Eitel 2013).

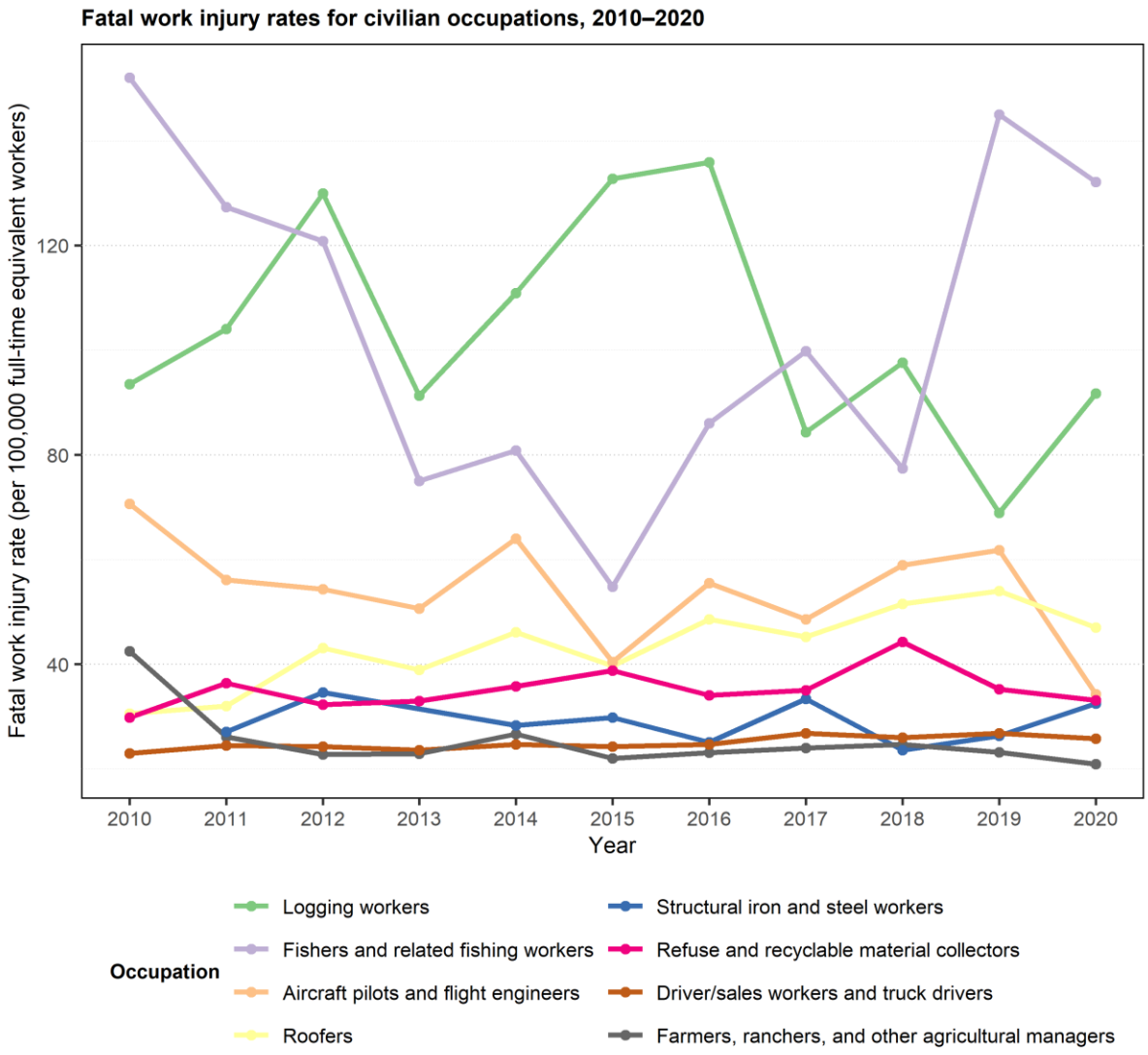

Figure 1.1. Fatal work injury rates for civilian occupations with some of the highest rates of fatal injuries from 2010 to 2020.

Wildland firefighting is also a high-risk occupation, with 480 fatalities between 1990 and 2016 (Risk Management Committee 2017). From 2001 to 2012, the leading causes of death among wildland firefighters were vehicle- and aviation-related incidents as well as medical events, such as strokes and heart attacks (Butler et al. 2017). Fire entrapments are another frequent cause of fatalities among firefighters (Butler et al. 2017; Risk Management Committee 2017). Heart attacks, vehicle and aircraft accidents, and entrapments represented 79% of the 170 wildland firefighter deaths between 2007 and 2016 (Risk Management Committee 2017). Efforts have been made to increase safety and reduce injuries and fatalities among firefighters (Risk Management Committee 2017) and most recently, the 2019 John D. Dingell, Jr. Conservation, Management, and Recreation Act required

implementation of a system to monitor the locations of all Federal type 1 wildland fire resources in the United States to improve safety (Murkowski 2019). Both logging and wildland firefighting involve frequent interactions among ground workers, heavy equipment, and dynamic terrain- and weather-related hazards. Additionally, this work occurs in remote, off-grid environments that often lack traditional cellular communications infrastructure. Thus, the use of real-time positional information as well as wearable-based activity recognition modeling have the potential to mitigate hazards by enhancing communication, safety, and situational awareness (SA) on active timber sales and in wildland firefighting.

1.2 Real-time Positioning for Situational Awareness

Advances in location- and data-sharing technologies such as real-time positioning systems, geofencing, activity recognition, and mesh networking have a range of potential applications in natural resources (Keefe et al. 2019a). The Global Positioning System (GPS) is a radio navigation system that became fully functional in 1993 (Mai 2015). GPS consists of 24 satellites which were launched by the Department of Defense and are configured such that at least four satellites are always visible at any point on Earth (Johnson and Barton 2004). Global navigation satellite system (GNSS) positioning is a more general term that encompasses all global satellite-based positioning systems such as GPS, GLONASS, Galileo, and BeiDou. Real-time GNSS tracking has become an integral part of various industries, such as precision agriculture (Stafford 2000; Zhang et al. 2002; Liaghat and Balasundram 2010), livestock management (Kawamura et al. 2005; Spink et al. 2013; Fogarty et al. 2018), and transportation (Mintsis et al. 2004; Higuera de Frutos and Castro 2014; Van Brummelen et al. 2018). In natural resources, previous applications of GNSS technology have largely focused on wildlife (Moen et al. 1996; Ryan et al. 2004; Lewis et al. 2007; Tomkiewicz et al. 2010; Brown et al. 2012; Quaglietta et al. 2012; Wall et al. 2014; Zeller et al. 2014; Kays et al. 2015), cattle grazing (Turner et al. 2000; Swain et al. 2008; Handcock et al. 2009), and a range of forest management applications, including locating forest inventory plots (Evans et al. 1992; Bilodeau et al. 1993), delineating harvest unit boundaries (Bilodeau et al. 1993), locating (Bilodeau et al. 1993) and planning (Cavalli and Grigolato 2010) forest roads, tracking harvesting equipment and log trucks (Veal et al. 2001; Devlin and McDonnell 2009; Spinelli et al. 2015), assessing site disturbance of harvesting machines (McDonald et al. 2002), calculating productivity from time-study data (McDonald and Fulton 2005; Gallo et al. 2013; Strandgard and Mitchell 2015), and quantifying production efficiency (Becker et al. 2017).

While traditional GNSS receivers allow users to see their own positions, GNSS-RF devices link GNSS positional information with radio frequency (RF) transmission of coordinates to enable real-time positioning among individuals and equipment in remote areas (Grayson et al. 2016; Becker et al. 2017; Wempe and Keefe 2017). GNSS-RF transponders include recreational or public safety devices, military-grade units designed for defense applications, and smartphone-based solutions that enable voice or text communication in areas lacking cellular service. Recently, consumer-grade GNSS-RF systems have been promoted as a possible solution to monitor the current safety status and location of individuals relative to workplace hazards in order to improve SA on logging operations (Keefe et al. 2014b; Grayson et al. 2016; Wempe and Keefe 2017; Newman et al. 2018; Wempe et al. 2019). Many newer GNSS-RF units form mesh networks, in which each device can relay data to other nodes in the network (Marina and Das 2001; Tseng et al. 2002). This enables communication among users who do not have a direct line-of-sight (LOS) connection (Tseng et al. 2002), which may offer more robust network connections in rugged, vegetated terrain. Before real-time positioning systems are implemented on active logging operations, in wildland firefighting, and for other applications in natural resources, the accuracy of GNSS-RF transmitters must be evaluated in order to determine appropriate and inappropriate uses for the technology.

The expansion of GNSS services has facilitated the development of geofencing, in which virtual perimeters are used to mark geographic zones (Reclus 2013). Mobile objects are tracked in real-time as they move around the zone and the geofence can detect proximity of these mobile objects to the virtual perimeter (Reclus 2013). While geofences have been used for agricultural (Anderson et al. 2004; Butler et al. 2006; Luxhøj 2015), wildlife (Gill et al. 2006; Licht et al. 2010; Monteiro et al. 2010; Wall et al. 2014; Sheppard et al. 2015; Weise et al. 2019), construction (Carbonari et al. 2011; Song and Eldin 2012), transportation (Reclus and Drouard 2009; Oliveira et al. 2013), and marketing (Greenwald et al. 2011) applications, they have only been implemented in forestry to a very limited extent (Grayson et al. 2016; Daniel et al. 2017; Wempe and Keefe 2017). There are a variety of situations on active logging operations in which it may be appropriate to deploy geofences around people, vehicles, equipment, or other objects in motion, in addition to stationary objects or areas. For example, mobile geofences could define safe working areas around manual fallers, log loaders and processors, and the skyline carriages on cable harvesting operations. Stationary geofences could mark harvest unit boundaries, streamside management zones, and hazardous terrain features. When other ground workers or equipment operators carrying GNSS-enabled personal location devices (PLDs) come into contact with these zones, alerts could be triggered. Thus, the use of both mobile and stationary geofences could ultimately improve safety by increasing general SA among workers on harvest units.

1.3 Wearable-based Human Activity Recognition

In addition to real-time positioning information available from GNSS-RF systems and geofences, data from wearable sensors in smartphones and smartwatches may also provide opportunities for quantifying occupational tasks in forestry (Keefe et al. 2019b) to ultimately improve health and safety as well as precision forestry. The high-resolution data collected by these sensors can be used for activity recognition modeling, in which the device automatically detects different human physical activities (Chen et al. 2012). While purpose-built sensors exist, inertial measurement units (IMUs) have become smaller, more accurate, and less expensive in recent years, and they have been widely integrated into common wearable devices, such as smartphones and smartwatches (Chen and Shen 2017). Inertial sensors have been used to develop a variety of human activity recognition models for everyday activities, recreation, and fitness applications (Bao and Intille 2004; Mathie et al. 2004; Ermes et al. 2008; Wu et al. 2012; Mitchell et al. 2013; Stöggl et al. 2014; Micucci et al. 2017), but very little activity recognition based on wearable sensors has focused on workplace activities (Ward et al. 2006; Stiefmeier et al. 2008; Joshua and Varghese 2011; Akhavian and Behzadan 2016; Valero et al. 2016). Utilizing wearable sensors to develop occupational activity recognition models in forestry represents an initial step toward quantifying work activities on logging operations with much higher frequency and resolution than has been previously accomplished. These model predictions could be leveraged to increase situational awareness by informing loggers and equipment operators of their own and their coworkers' job activity status in near real-time. Wearable-based human work activity recognition in forestry is a novel approach that could supplement GNSS positional information to further improve communication and safety on logging operations. Future pairing of activity recognition model predictions, personal health metrics, and real-time location sharing could foster the development of smart alerts in the context of incident prevention, notification, or response.

1.4 Dissertation Objectives

The overall goal of my research is to evaluate the factors that affect the positioning and communication quality of GNSS-RF devices and to characterize the ability of wearable sensors to predict work activities on active logging operations. In order to determine how real-time positioning, geofencing, mesh networking, and wearable technology could be implemented to improve safety on logging operations and in wildland firefighting, this dissertation addresses four main research objectives: 1) develop the concept of GNSS-RF mobile geofences and model the intersections of mobile and stationary geofences as mixtures of bivariate normal error distributions; 2) evaluate the

effects of forest stand characteristics, topography, and other LOS obstructions on the radio signal propagation quality, positional accuracy, and time-to-signal accuracy of geofence crossings for a network of GNSS-RF transponders; 3) characterize and predict the connectivity of smartphone-based GNSS-RF mesh networks using lidar- and satellite-derived terrain and vegetation metrics; and 4) create smartwatch-based human activity recognition models for rigging crew workers on cable logging operations to support and inform the optimal use of wearable devices that quantify occupational work activities in forestry.

By addressing these four objectives, this research provides insight into opportunities for the use of location sharing networks and wearable-based human activity recognition for occupational safety applications in forestry. In related research not included in the dissertation (Keefe et al. 2019b), I also conducted analysis to develop the first human activity recognition models for hand fallers using smartphone IMU sensors. Ultimately, GNSS-RF communication, mobile and stationary geofences, mesh networking, and human activity recognition are important advances that comprise a real-time location- and data-sharing system that functions off the grid, increasing communication and SA in remote, forested environments to improve safety. While these studies are focused on logging and wildland firefighting, there are many opportunities to use similar real-time positioning and human activity recognition techniques in a variety of applications in natural resources, including emergency response, defense, wildlife ecology and management, transportation, and recreation.

1.5 Literature Cited

Akhavian R, Behzadan AH. Smartphone-based construction workers' activity recognition and classification. Autom Constr. 2016 Nov;71(2):198–209. doi:10.1016/j.autcon.2016.08.015.

Anderson DM, Nolen B, Fredrickson E, Havstad K, Hale C, Nayak P. Representing spatially explicit Directional Virtual Fencing (DVF) data. In: Proceedings of the 24th Annual ESRI International User Conference. San Diego, CA, USA; 2004.

Axelsson S-Ă. The mechanization of logging operations in Sweden and its effect on occupational safety and health. J For Eng. 1998 Jun 1;9(2):25–31. doi:10.1080/08435243.1998.10702715.

Bao L, Intille SS. Activity recognition from user-annotated acceleration data. In: Ferscha A, Mattern F, editors. Proceedings of the Second International Conference on Pervasive Computing. Linz/Vienna, Austria: Springer, Berlin, Heidelberg; 2004. p. 1–17. (Lecture Notes in Computer Science). doi:10.1007/978-3-540-24646-6_1.

Becker RM, Keefe RF, Anderson NM. Use of real-time GNSS-RF data to characterize the swing movements of forestry equipment. Forests. 2017 Feb;8(2):44. doi:10.3390/f8020044.

Bell JL. Changes in logging injury rates associated with use of feller-bunchers in West Virginia. J Safety Res. 2002 Dec;33(4):463–71. doi:10.1016/S0022-4375(02)00048-8.

Bilodeau J-M, Gosselin S, Lowell K, Edwards G, Gold C. Operational integration of GPS into forest management activities which use a GIS to monitor forest operations. In: Proceedings of the GIS'93 Symposium. Vancouver, BC, Canada; 1993. p. 195–200.

Bonauto DK, Wuellner SE, Marcum JL, Adams DA. Injury rate comparisons for nonmechanized and mechanized logging operations, Washington State, 2005-2014. J Agromedicine. 2019 Apr;24(2):205–14. doi:10.1080/1059924X.2019.1566106.

Brown DD, LaPoint S, Kays R, Heidrich W, Kümmeth F, Wikelski M. Accelerometer-informed GPS telemetry: reducing the trade-off between resolution and longevity. Wildl Soc Bull. 2012 Mar;36(1):139–46. doi:10.1002/wsb.111.

Butler C, Marsh S, Domitrovich JW, Helmkamp J. Wildland firefighter deaths in the United States: A comparison of existing surveillance systems. J Occup Environ Hyg. 2017 Apr;14(4):258–70. doi:10.1080/15459624.2016.1250004.

Butler Z, Corke P, Peterson R, Rus D. From robots to animals: virtual fences for controlling cattle. Int J Robot Res. 2006 May;25(5–6):485–508. doi:10.1177/0278364906065375.

Carbonari A, Giretti A, Naticchia B. A proactive system for real-time safety management in construction sites. Autom Constr. 2011 Oct;20(6):686–98. doi:10.1016/j.autcon.2011.04.019.

Cavalli R, Grigolato S. Influence of characteristics and extension of a forest road network on the supply cost of forest woodchips. J For Res. 2010 Jun;15(3):202–9. doi:10.1007/s10310-009-0170-4.

Chen L, Hoey J, Nugent CD, Cook DJ, Yu Z. Sensor-based activity recognition. IEEE Trans Syst Man Cybern Part C Appl Rev. 2012 Nov;42(6):790–808. doi:10.1109/TSMCC.2012.2198883.

Chen Y, Shen C. Performance analysis of smartphone-sensor behavior for human activity recognition. IEEE Access. 2017;5:3095–110. doi:10.1109/ACCESS.2017.2676168.

Daniel MJ, Gallagher T, McDonald T, Mitchell D. Utilization of phone application technology to record log truck movements in the southeastern U.S. In: Proceedings of the 2017 Council on Forest Engineering Meeting [Internet]. Bangor, ME, USA; 2017 [cited 2019 Apr 25]. Available from: https://www.fs.usda.gov/treesearch/pubs/57602

Devlin GJ, McDonnell K. Performance accuracy of real-time GPS asset tracking systems for timber haulage trucks travelling on both internal forest road and public road networks. Int J For Eng. 2009 Jan;20(1):45–9. doi:10.1080/14942119.2009.10702575.

Ermes M, Pärkkä J, Mäntyjärvi J, Korhonen I. Detection of daily activities and sports with wearable sensors in controlled and uncontrolled conditions. IEEE Trans Inf Technol Biomed. 2008 Jan;12(1):20–6. doi:10.1109/TITB.2007.899496.

Evans DL, Carraway RW, Simmons GT. Use of global positioning system (GPS) for forest plot location. South J Appl For. 1992 May;16(2):67–70. doi:10.1093/sjaf/16.2.67.

Fogarty ES, Swain DL, Cronin G, Trotter M. Autonomous on-animal sensors in sheep research: a systematic review. Comput Electron Agric. 2018 Jul;150:245–56. doi:10.1016/j.compag.2018.04.017.

Fosbroke DE, Kisner SM, Myers JR. Working lifetime risk of occupational fatal injury. Am J Ind Med. 1997;31(4):459–67. doi:10.1002/(SICI)1097-0274(199704)31:4<459::AID-AJIM13>3.0.CO;2-Z.

Gallo R, Grigolato S, Cavalli R, Mazzetto F. GNSS-based operational monitoring devices for forest logging operation chains. J Agric Eng. 2013 Sep;44(2s):140–4. doi:10.4081/jae.2013.269.

Gill E, Fox BM, Kreisel J. Emerging commercial opportunities based on combined communication–navigation services. Acta Astronaut. 2006;59(1–5):100–6. doi:10.1016/j.actaastro.2006.02.004.

Grayson LM, Keefe RF, Tinkham WT, Eitel JUH, Saralecos JD, Smith AMS, et al. Accuracy of WAAS-enabled GPS-RF warning signals when crossing a terrestrial geofence. Sensors. 2016 Jun;16(6):912. doi:10.3390/s16060912.

Greenwald A, Hampel G, Phadke C, Poosala V. An economically viable solution to geofencing for mass-market applications. Bell Labs Tech J. 2011 Sep;16(2):21–38. doi:10.1002/bltj.20500.

Handcock RN, Swain DL, Bishop-Hurley GJ, Patison KP, Wark T, Valencia P, et al. Monitoring animal behaviour and environmental interactions using wireless sensor networks, GPS collars and satellite remote sensing. Sensors. 2009 May;9(5):3586–603. doi:10.3390/s90503586.

Higuera de Frutos S, Castro M. Using smartphones as a very low-cost tool for road inventories. Transp Res Part C Emerg Technol. 2014 Jan;38:136–45. doi:10.1016/j.trc.2013.11.012.

Johnson CE, Barton CC. Where in the world are my field plots? Using GPS effectively in environmental field studies. Front Ecol Environ. 2004;2(9):475–82. doi:10.1890/1540-9295(2004)002[0475:WITWAM]2.0.CO;2.

Joshua L, Varghese K. Accelerometer-based activity recognition in construction. J Comput Civ Eng. 2011 Sep;25(5):370–9. doi:10.1061/(ASCE)CP.1943-5487.0000097.

Kawamura K, Akiyama T, Yokota H, Tsutsumi M, Yasuda T, Watanabe O, et al. Quantifying grazing intensities using geographic information systems and satellite remote sensing in the Xilingol steppe region, Inner Mongolia, China. Agric Ecosyst Environ. 2005 May;107(1):83–93. doi:10.1016/j.agee.2004.09.008.

Kays R, Crofoot MC, Jetz W, Wikelski M. Terrestrial animal tracking as an eye on life and planet. Science. 2015 Jun;348(6240):aaa2478. doi:10.1126/science.aaa2478.

Keefe R, Anderson N, Hogland J, Muhlenfeld K. Woody biomass logistics. In: Karlen DL, editor. Cellulosic Energy Cropping Systems. 1st ed. John Wiley & Sons, Ltd.; 2014a. p. 251–79.

Keefe RF, Eitel JUH. Application of carriage-mounted agricultural cameras to improve safety in cable logging operations. In: Proceedings of the 2013 Annual Meeting of the Council on Forest Engineering [Internet]. Missoula, MT, USA; 2013. Available from: https://www.researchgate.net/profile/Robert_Keefe4/publication/313038138_Application_of_carriage-mounted_agricultural_cameras_to_improve_safety_in_cable_logging_operations/links/588e3f1092851cef1362ca6a/Application-of-carriage-mounted-agricultural-cameras-to-improve-safety-in-cable-logging-operations.pdf

Keefe RF, Eitel JUH, Smith AMS, Tinkham WT. Applications of multi transmitter GPS-VHF in forest operations. In: Proceedings of the 47th International Symposium on Forestry Mechanization and 5th International Forest Engineering Conference [Internet]. Gerardmer, France; 2014b. Available from: http://fec2014.fcba.fr/wp-content/uploads/sites/4/2014/11/a189.pdf

Keefe RF, Wempe AM, Becker RM, Zimbelman EG, Nagler ES, Gilbert SL, et al. Positioning methods and the use of location and activity data in forests. Forests. 2019a May;10(5):458. doi:10.3390/f10050458.

Keefe RF, Zimbelman EG, Wempe AM. Use of smartphone sensors to quantify the productive cycle elements of hand fallers on industrial cable logging operations. Int J For Eng. 2019b May;30(2):132–43. doi:10.1080/14942119.2019.1572489.

Lagerstrom E, Magzamen S, Rosecrance J. A mixed-methods analysis of logging injuries in Montana and Idaho. Am J Ind Med. 2017 Dec;60(12):1077–87. doi:10.1002/ajim.22759.

Lefort AJ Jr, de Hoop CF, Pine JC, Marx BD. Characteristics of injuries in the logging industry of Louisiana, USA: 1986 to 1998. Int J For Eng. 2003;14(2):75–89. doi:10.1080/14942119.2003.10702480.

Lewis JS, Rachlow JL, Garton EO, Vierling LA. Effects of habitat on GPS collar performance: using data screening to reduce location error. J Appl Ecol. 2007;44(3):663–71. doi:10.1111/j.1365-2664.2007.01286.x.

Liaghat S, Balasundram SK. A review: the role of remote sensing in precision agriculture. Am J Agric Biol Sci. 2010 Mar 31;5(1):50–5. doi:10.3844/ajabssp.2010.50.55.

Licht DS, Millspaugh JJ, Kunkel KE, Kochanny CO, Peterson RO. Using small populations of wolves for ecosystem restoration and stewardship. BioScience. 2010 Feb;60(2):147–53. doi:10.1525/bio.2010.60.2.9.

Luxhøj JT. A socio-technical model for analyzing safety risk of unmanned aircraft systems (UAS): an application to precision agriculture. Procedia Manuf. 2015 Jan;3:928–35. doi:10.1016/j.promfg.2015.07.140.

Mai T. Global Positioning System History [Internet]. NASA. 2015 [cited 2019 Feb 6]. Available from: http://www.nasa.gov/directorates/heo/scan/communications/policy/GPS_History.html

Marina MK, Das SR. On-demand multipath distance vector routing in ad hoc networks. In: Proceedings of the Ninth International Conference on Network Protocols (ICNP 2001). Riverside, CA, USA: IEEE; 2001. p. 14–23. doi:10.1109/ICNP.2001.992756.

Mathie MJ, Celler BG, Lovell NH, Coster ACF. Classification of basic daily movements using a triaxial accelerometer. Med Biol Eng Comput. 2004 Sep;42(5):679–87. doi:10.1007/BF02347551.

McDonald TP, Carter EA, Taylor SE. Using the global positioning system to map disturbance patterns of forest harvesting machinery. Can J For Res. 2002 Feb;32(2):310–9. doi:10.1139/x01-189.

McDonald TP, Fulton JP. Automated time study of skidders using global positioning system data. Comput Electron Agric. 2005 Jul;48(1):19–37. doi:10.1016/j.compag.2005.01.004.

Micucci D, Mobilio M, Napoletano P. UniMiB SHAR: a dataset for human activity recognition using acceleration data from smartphones. Appl Sci. 2017 Oct;7(10):1101. doi:10.3390/app7101101.

Mintsis G, Basbas S, Papaioannou P, Taxiltaris C, Tziavos IN. Applications of GPS technology in the land transportation system. Eur J Oper Res. 2004 Jan 16;152(2):399–409. doi:10.1016/S0377-2217(03)00032-8.

Mitchell E, Monaghan D, O'Connor NE. Classification of sporting activities using smartphone accelerometers. Sensors. 2013 Apr;13(4):5317–37. doi:10.3390/s130405317.

Moen R, Pastor J, Cohen Y, Schwartz CC. Effects of moose movement and habitat use on GPS collar performance. J Wildl Manag. 1996;60(3):659–68. doi:10.2307/3802085.

Monteiro S, Vázquez X, Long R. Improving fishery law enforcement in marine protected areas. Aegean Rev Law Sea Marit Law. 2010 Feb;1(1):95–109. doi:10.1007/s12180-009-0002-6.

Murkowski L. Text - S.47 - 116th Congress (2019-2020): John D. Dingell, Jr. Conservation, Management, and Recreation Act [Internet]. 2019 [cited 2022 Apr 1]. Available from: https://www.congress.gov/bill/116th-congress/senate-bill/47/text

Newman SM, Keefe RF, Brooks RH, Ahonen EQ, Wempe AM. Human factors affecting logging injury incidents in Idaho and the potential for real-time location-sharing technology to improve safety. Safety. 2018 Dec;4(4):43. doi:10.3390/safety4040043.

Oliveira RR, Noguez FC, Costa CA, Barbosa JL, Prado MP. SWTRACK: An intelligent model for cargo tracking based on off-the-shelf mobile devices. Expert Syst Appl. 2013 May;40(6):2023–31. doi:10.1016/j.eswa.2012.10.021.

Quaglietta L, Martins BH, de Jongh A, Mira A, Boitani L. A low-cost GPS GSM/GPRS telemetry system: performance in stationary field tests and preliminary data on wild otters (Lutra lutra). PLoS ONE. 2012 Jan;7(1):e29235. doi:10.1371/journal.pone.0029235.

Reclus F. Geofencing. In: Nait-Sidi-Moh A, Bakhouya M, Gaber J, Wack M, editors. Geopositioning and Mobility [Internet]. Hoboken, NJ: John Wiley & Sons, Ltd; 2013. p. 127–54. doi:10.1002/9781118743751.ch6.

Reclus F, Drouard K. Geofencing for fleet & freight management. In: Proceedings of the 2009 9th International Conference on Intelligent Transport Systems Telecommunications (ITST). Lille, France: IEEE; 2009. p. 353–6. doi:10.1109/ITST.2009.5399328.

Risk Management Committee. NWCG report on wildland firefighter fatalities in the United States: 2007-2016 [Internet]. National Wildfire Coordinating Group; 2017 Dec. Report No.: PMS 841. Available from: https://www.nwcg.gov/publications/841

Ryan PG, Petersen SL, Peters G, Grémillet D. GPS tracking a marine predator: the effects of precision, resolution and sampling rate on foraging tracks of African Penguins. Mar Biol. 2004 Aug 1;145(2):215–23. doi:10.1007/s00227-004-1328-4.

Shaffer RM, Milburn JS. Injuries on feller-buncher/grapple skidder logging operations in the Southeastern United States. For Prod J. 1999 Aug;49(7/8):24–6.

Sheppard JK, McGann A, Lanzone M, Swaisgood RR. An autonomous GPS geofence alert system to curtail avian fatalities at wind farms. Anim Biotelemetry. 2015 Oct;3:43. doi:10.1186/s40317-015-0087-y.

Song L, Eldin NN. Adaptive real-time tracking and simulation of heavy construction operations for look-ahead scheduling. Autom Constr. 2012 Nov;27:32–9. doi:10.1016/j.autcon.2012.05.007.

Spinelli R, Magagnotti N, Pari L, De Francesco F. A comparison of tractor-trailer units and high-speed forwarders used in Alpine forestry. Scand J For Res. 2015 Jul;30(5):470–7. doi:10.1080/02827581.2015.1012113.

Spink A, Cresswell B, Kölzsch A, van Langevelde F, Neefjes M, Noldus LPJJ, et al. Animal behaviour analysis with GPS and 3D accelerometers. In Leuven, Belgium; 2013 [cited 2019 Apr 26]. p. 229–39. Available from: https://library.wur.nl/WebQuery/wurpubs/443086

Stafford JV. Implementing precision agriculture in the 21st century. J Agric Eng Res. 2000 Jul;76(3):267–75. doi:10.1006/jaer.2000.0577.

Stiefmeier T, Roggen D, Ogris G, Lukowicz P, Tröster G. Wearable activity tracking in car manufacturing. IEEE Pervasive Comput. 2008 Apr;7(2):42–50. doi:10.1109/MPRV.2008.40.

Stöggl T, Holst A, Jonasson A, Andersson E, Wunsch T, Norström C, et al. Automatic classification of the sub-techniques (gears) used in cross-country ski skating employing a mobile phone. Sensors. 2014 Nov;14(11):20589–601. doi:10.3390/s141120589.

Strandgard M, Mitchell R. Automated time study of forwarders using GPS and a vibration sensor. Croat J For Eng. 2015 Oct;36(2):175–84.

Swain DL, Wark T, Bishop-Hurley GJ. Using high fix rate GPS data to determine the relationships between fix rate, prediction errors and patch selection. Ecol Model. 2008 Apr;212(3):273–9. doi:10.1016/j.ecolmodel.2007.10.027.

Sygnatur EF. Logging is perilous work. Compens Work Cond. 1998;3:3–9.

Tomkiewicz SM, Fuller MR, Kie JG, Bates KK. Global positioning system and associated technologies in animal behaviour and ecological research. Philos Trans R Soc B Biol Sci. 2010 Jul;365(1550):2163–76. doi:10.1098/rstb.2010.0090.

Tseng Y-C, Ni S-Y, Chen Y-S, Sheu J-P. The broadcast storm problem in a mobile ad hoc network. Wirel Netw. 2002 Mar;8(2):153–67. doi:10.1023/A:1013763825347.

Turner LW, Udal MC, Larson BT, Shearer SA. Monitoring cattle behavior and pasture use with GPS and GIS. Can J Anim Sci. 2000 Sep;80(3):405–13. doi:10.4141/A99-093.

U.S. Bureau of Labor Statistics. Census of Fatal Occupational Injuries (CFOI) - Current and Revised Data [Internet]. 2021 [cited 2021 Dec 22]. Available from: https://www.bls.gov/iif/oshcfoi1.htm#rates

Valero E, Sivanathan A, Bosché F, Abdel-Wahab M. Musculoskeletal disorders in construction: A review and a novel system for activity tracking with body area network. Appl Ergon. 2016 May;54:120–30. doi:10.1016/j.apergo.2015.11.020.

Van Brummelen J, O'Brien M, Gruyer D, Najjaran H. Autonomous vehicle perception: The technology of today and tomorrow. Transp Res Part C Emerg Technol. 2018 Apr;89:384–406. doi:10.1016/j.trc.2018.02.012.

Veal MW, Taylor SE, McDonald TP, McLemore DK, Dunn MR. Accuracy of tracking forest machines with GPS. Trans ASAE. 2001;44(6):1903–11. doi:10.13031/2013.6978.

Wall J, Wittemyer G, Klinkenberg B, Douglas-Hamilton I. Novel opportunities for wildlife conservation and research with real-time monitoring. Ecol Appl. 2014 Jun;24(4):593–601. doi:10.1890/13-1971.1.

Ward JA, Lukowicz P, Tröster G, Starner TE. Activity recognition of assembly tasks using body-worn microphones and accelerometers. IEEE Trans Pattern Anal Mach Intell. 2006 Oct;28(10):1553–67. doi:10.1109/TPAMI.2006.197.

Weise FJ, Hauptmeier H, Stratford KJ, Hayward MW, Aal K, Heuer M, et al. Lions at the gates: trans-disciplinary design of an early warning system to improve human-lion coexistence. Front Ecol Evol. 2019 Jan;6:242. doi:10.3389/fevo.2018.00242.

Wempe AM, Keefe RF. Characterizing rigging crew proximity to hazards on cable logging operations using GNSS-RF: Effect of GNSS positioning error on worker safety status. Forests. 2017 Sep;8(10):357. doi:10.3390/f8100357.

Wempe AM, Keefe RF, Newman SM, Paveglio TB. Intent to adopt location sharing for logging safety applications. Safety. 2019 Mar;5(1):7. doi:10.3390/safety5010007.

Wu W, Dasgupta S, Ramirez EE, Peterson C, Norman GJ. Classification accuracies of physical activities using smartphone motion sensors. J Med Internet Res. 2012;14(5):e130. doi:10.2196/jmir.2208.

Zeller KA, McGarigal K, Beier P, Cushman SA, Vickers TW, Boyce WM. Sensitivity of landscape resistance estimates based on point selection functions to scale and behavioral state: pumas as a case study. Landsc Ecol. 2014 Mar;29(3):541–57. doi:10.1007/s10980-014-9991-4.

Zhang N, Wang M, Wang N. Precision agriculture - a worldwide overview. Comput Electron Agric. 2002 Nov;36(2):113–32. doi:10.1016/S0168-1699(02)00096-0.

Chapter 2: Hazards in Motion: Development of Mobile Geofences for Use in Logging Safety

Published In:

Zimbelman EG, Keefe RF, Strand EK, Kolden CA, Wempe AM. Hazards in motion: Development of mobile geofences for use in logging safety. Sensors. 2017 Apr;17(4):822. doi:10.3390/s17040822.

2.1 Abstract

Logging is one of the most hazardous occupations in the United States. Real-time positioning that uses global navigation satellite system (GNSS) technology paired with radio frequency transmission (GNSS-RF) has the potential to reduce fatal and non-fatal accidents on logging operations through the use of geofences that define safe work areas. Until recently, most geofences have been static boundaries. The aim of this study was to evaluate factors affecting mobile geofence accuracy in order to determine whether virtual safety zones around moving ground workers or equipment are a viable option for improving situational awareness on active timber sales. We evaluated the effects of walking pace, transmission interval, geofence radius, and intersection angle on geofence alert delay using a replicated field experiment. Simulation was then used to validate field results and calculate the proportion of GNSS error bearings resulting in early alerts. The interaction of geofence radius and intersection angle affected safety geofence alert delay in the field experiment. The most inaccurate alerts were negative, representing early warning. The magnitude of this effect was largest at the greatest intersection angles. Simulation analysis supported these field results and also showed that larger GNSS error corresponded to greater variability in alert delay. Increasing intersection angle resulted in a larger proportion of directional GNSS error that triggered incorrect, early warnings. Because the accuracy of geofence alerts varied greatly depending on GNSS error and angle of approach, geofencing for occupational safety is most appropriate for general situational awareness unless real-time correction methods to improve accuracy or higher quality GNSS-RF transponders are used.

2.2 Introduction

Logging involves frequent interactions among ground workers, heavy equipment, and dynamic terrain- and weather-related hazards, leading to many high-risk safety situations. As a result,

logging is consistently ranked as one of the most hazardous occupations in the United States [1]. Fosbroke et al. analyzed national fatality data from the National Institute for Occupational Safety and Health (NIOSH) National Traumatic Occupational Fatalities (NTOF) surveillance system for the years 1990 and 1991 and found logging to have the highest lifetime risk of fatal injury [2]. Logging also has high rates of fatal and non-fatal injuries internationally [3,4]. The increasing mechanization of logging has been shown to reduce accident frequency, primarily by protecting workers in enclosed cabs from falling trees [5,6]. However, fatal injuries remain common, despite mechanization and stricter safety standards imposed by the U.S. Occupational Safety and Health Administration (OSHA) [7,8]. According to the U.S. Bureau of Labor Statistics, logging had the highest fatal work injury rate of civilian occupations in 2015 [9]. Direct contacts with trees and logs are responsible for a large portion of fatal injuries to loggers [1]. In particular, cable logging leads to many accidents resulting from manual falling with chainsaws, rolling logs, and close proximity of ground crews and heavy equipment. Low visibility between yarder operators and the ground crew contributes to many cable logging accidents [10].

Global navigation satellite system (GNSS) technology is used widely in positioning, navigation and timing (PNT). Utilizing real-time GNSS positioning information has the potential to mitigate hazards by enhancing communication and situational awareness on active timber sales. However, canopy cover in forested environments reduces GNSS accuracy, which has hindered widespread adoption of real-time positioning in forestry [11]. Sources of error in GNSS measurements include the number and arrangement of GNSS satellites as well as signal obstruction by forest canopy, topography, and buildings [12]. Of the three commonly recognized classes of GNSS receivers (survey-, mapping-, and recreation-grade), recreation-grade receivers are the least expensive, but also tend to provide the least accurate GNSS positional information [13]. We chose to work with a recreation-grade receiver because of the low cost and potential for widespread adoption. Previous studies have reported on the horizontal positional accuracy of stationary recreation-grade GNSS units. Using six recreation-grade GNSS units, Wing determined that the average error of the most accurate receiver was 2 m or less in open conditions, 3 m or less in young forest, and 9 m or less in closed canopy [14]. In a similar study, Wing calculated average errors of 2.5 m, 5.5 m, and 3.8 m in open, young, and mature stands, respectively [15]. Andersen et al. reported root mean squared error (RMSE) values of 3–7 m in a range of stand conditions in Alaska [16]. Bettinger and Fei calculated mean RMSE of 11.9 m and 6.6 m in young and mature loblolly pine stands, respectively, and 7.9 m in mature oak-hickory forest [13].

The expansion of GNSS services has led to the development of geofencing, which consists of delineating a geographic zone with a virtual perimeter [17]. This boundary can be a fixed radius around a designated point of interest or a polygon whose corners are defined by the user [18]. As tracked mobile objects move across the geofence, alarms may be signaled [18]. This system has great potential for monitoring the movement of people, equipment, vehicles and other mobile assets [19]. Currently, geofencing is used in fields such as transportation and logistics [19], fleet management [20], and mobile marketing and social networking [21]. Geofencing services have also been proposed for use in mobile tourism, through which visitors may receive personalized notifications based on their location within defined areas [22]. Song and Eldin proposed using geofencing to monitor heavy equipment and construction events in real-time on building construction and worksite operations [23]. Pestana et al. found that geofences can support airport operations by improving safety and efficiency [24] and Wawrzyniak and Hyla evaluated the use of geofencing technology to assist navigation of inland waterways [25]. Finally, in the defense and security sector, some governments have analyzed the potential for using geofences as tools to prevent terrorist attacks involving hazardous material transport [19].

In natural resources, geofence alerts have been suggested as a way to monitor fishing activity near exclusive economic zones (EEZ) [26] and as an indicator of marine protection areas [27]. Licht et al. described the use of geofences in real-time animal tracking [28] and Sheppard et al. proposed the use of geofencing to reduce bird mortalities at wind farms [29]. Wall et al. developed software for a real-time wildlife monitoring system that utilizes multiple movement algorithms [30]. In agriculture, Butler et al. developed a dynamic virtual fence algorithm as a fenceless method for herding cows [31] and Anderson et al. used a patented method called Directional Virtual Fencing to contain cattle within a moving virtual paddock [32]. Geofence techniques are also being considered to minimize potential collisions among Unmanned Aircraft Systems used in precision agriculture [33]. Other industries have investigated the use of real-time positioning and geofences for safety applications. Carbonari et al. developed a safety system for construction using ultra-wideband tracking and virtual fencing to warn workers of hazardous areas [34]. Information derived from GNSS units has been considered as a tool for improving operational monitoring and time studies in forest operations [35,36]. Combined global navigation satellite system-radio frequency transmission (GNSS-RF) systems integrate GNSS with radio transmission of location coordinates to facilitate position sharing among individuals and equipment working in the woods [37,38]. The use of multi transmitter GNSS-RF systems has been proposed for logging safety as well as for other applications in forest operations [37–39].

There are many situations on active logging operations, in wildland firefighting, transportation, recreation, and bioenergy fields in which it may be appropriate to deploy geofences around people, vehicles, equipment, animals, or other objects in motion, rather than around stationary objects or areas. For many of these safety applications in natural resources, the situational awareness of workers or recreationists could be improved if geofences were used in a mobile rather than stationary context. This is especially true in logging and wildland firefighting, two occupations that involve numerous interactions among ground workers, heavy equipment and dynamic terrain- and weather-related hazards. For example, mobile geofences could define safe working areas around manual fallers, log loaders and processors on ground-based logging operations, as well as around skyline carriages when using cable systems. When other ground workers or equipment operators wearing GNSS- or radio frequency identification (RFID)-enabled personal location devices (PLDs) pass into hazard zones delineated by geofences, alarms could be triggered so that equipment operators are aware of their presence. Mobile geofences might also be used to define early warning perimeters around log trucks to indicate their location driving on active haul roads or around vehicles carrying hazardous materials. Few studies have documented the accuracy of geofence alerts concerning their use in logging applications. Grayson et al. performed a replicated field experiment to determine how speed, intersection angle, and distance between the tracked object and GNSS receiver affect fixed location geofence accuracy using speeds corresponding to log trucks and skidders [38].

Until recently, geofences have primarily been used as static boundaries. A few exceptions include Guo et al., who developed a model for dynamic geofences centered on moving vehicles for use in accident prevention [40], as well as the algorithms described in Butler et al. and Anderson et al. [31,32]. There also is limited data on the effects of speed and transmission interval on mobile GNSS accuracy in forestry. Veal et al. measured the accuracy of tracking forest machines using GPS and found that equipment speed did not affect position accuracy [41]. However, the difference among equipment speeds evaluated was relatively small [41]. Grayson et al. found larger error associated with geofence crossing delays at slower speeds [38]. Piedallu and Gégout found that recording interval had a small effect on GPS accuracy and observed improved accuracy when moving from a 1-s to 5-s recording interval [42]. They observed smaller improvements in accuracy moving from 5-s to 10-s to 15-s recording intervals and this effect was mainly noticeable in closed canopy rather than in the open [42]. However, other studies have found either increases in location time [43], larger positional errors [44], or lower fix success rates [45] associated with longer intervals between recordings.

In this paper, we expand on the concept of mobile geofences based on GNSS-RF technology for use in forestry as moving, circular safety zones around people and heavy equipment on active logging operations, a concept illustrated in Figure 2.1. We considered both traditional proximity alerts, as well as the overlap among multiple circular geofences of varying radii. To do this, a replicated experiment on the University of Idaho Experimental Forest was conducted to test the null hypothesis that walking pace, transmission interval, geofence size (radius), and the angle at which a geofence intersects a stationary point do not affect geofence alert delay. Our focus was primarily on the development of mobile safety geofences for manual fallers on logging operations due to the high number of fatal accidents that continue to occur during hand falling of timber. In order to provide a general method for analysis of mobile GNSS points in motion and associated geofences, simulation was used to describe the properties of circular geofences of varying sizes as they pass near one another or overlap, and the associated safety warning signals. We assumed GNSS error arises from a bivariate normal probability density. Our objective in doing so was to determine whether geofences and geofence alerts associated with recreation-grade GNSS-RF systems are suitable for occupational safety uses in remote, natural resource environments.

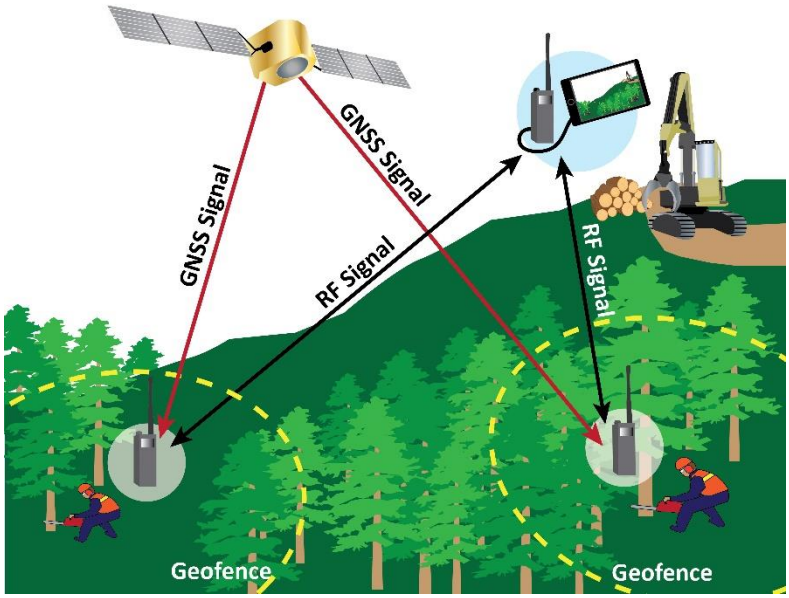

Figure 2.1. Illustration of the potential use of global navigation satellite system (GNSS) technology paired with radio frequency transmission (GNSS-RF) on a timber sale. GNSS-RF personal location devices (PLDs) receive positional information from GNSS satellites and send that information to nearby units using radio frequency transmission. In this figure, geofences with radii of approximately two tree lengths surround the manual fallers, delineating virtual perimeters associated with occupational hazards. Audible or sensory (e.g., vibration) alerts are triggered when other PLDs cross into the hazard areas, which move with individual workers.

2.3 Materials and Methods

Two Garmin Alpha 100 handheld GNSS-RF units (Garmin, Olathe, Kansas, USA) were used with seven T5 transponders serving as PLDs to collect position measurements. T5 PLDs receive GNSS coordinates and relay them to handheld devices via radio frequency at user-defined intervals ranging from 2.5 to 120 s. The Garmin Alpha 100 units plot and record the positions of the PLDs, as well as their own positions at these same time intervals.

The experiment was carried out in Stand 358 of the East Hatter Creek unit of the University of Idaho Experimental Forest. Stand 358 has been managed using the seed tree regeneration method and was treated (harvested) in the year 2000. There were approximately 15–20 seed trees per hectare at 50-cm or greater diameter at breast height (DBH) in the residual overstory and 800 trees per hectare at 10-cm DBH in the regenerating cohort. The canopy was open and the terrain was gently rolling. Within the stand, a manual faller carrying a saw walked repeatedly along a fixed 300-m route with a T5 PLD recording the path, as shown in Figure 2.2.

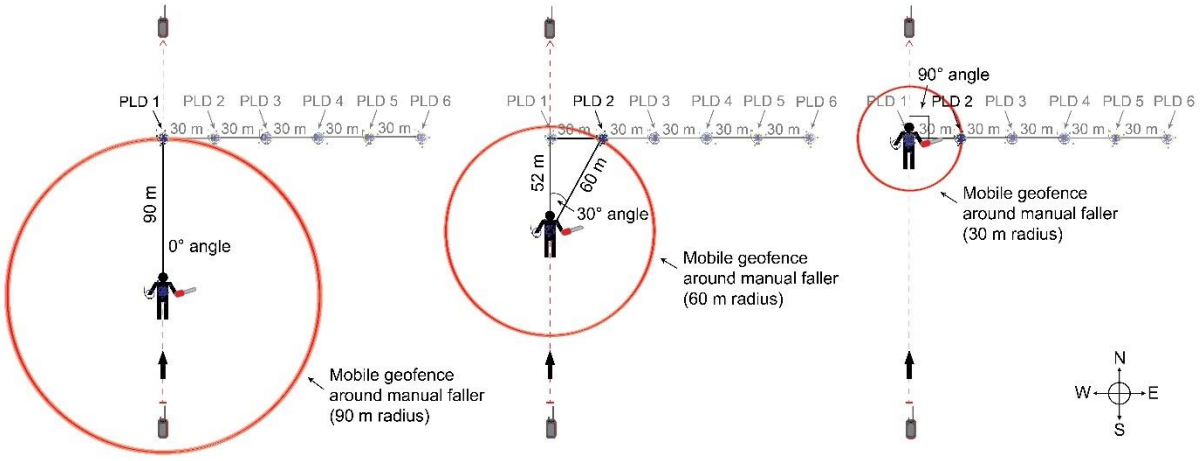

Figure 2.2. Illustration showing field experiment setup. The manual faller carried a T5 transponder (PLD) and a chainsaw along a 300-m route. Alpha 100 units recorded the GNSS data and were located at the start and end of the route. The six stationary PLDs located perpendicular to the route are shown. This figure shows the manual faller surrounded by mobile geofences of three radii, illustrating three possible intersection angles.

The route was oriented north-south in order to minimize variation in the longitudinal coordinates associated with unit resolution. Six T5 PLDs were placed 1 m above the ground on wooden stakes perpendicular to the designated route. PLD 1 was located in the middle of the route 150 m from the start point. Moving due east from PLD 1, PLDs 2–6 were placed in 30-m increments. Two Alpha 100 handheld units mounted on wooden stakes 1 m above the ground recorded the PLD data during the experiment. One Alpha 100 was located at the start point and the second was at the end point. The experiment was an incomplete randomized block design. The manual faller walked

along the route at three different paces as dictated by a digital metronome (30 bpm, 45 bpm, and 60 bpm), in combination with three different PLD transmission intervals (2.5 s, 5 s, and 10 s). The experiment was conducted over the course of three days, with each day representing one block. Each of the nine pace and transmission interval combinations appeared once per block and treatments were assigned at random. The manual faller was surrounded by seven different geofence radii (30, 45, 60, 75, 90, 105, and 120 m). These seven geofence radii combined with the six PLD locations described above resulted in 23 unique combinations of geofence radii and intersection angles, after excluding factor-level combinations that were not realized (Table 2.1). Intersection angle is the difference in azimuth formed between the vector heading of the walking path and the vector connecting the moving faller and stationary PLD at the time of intersection. Figure 2.2 shows three radius-angle combinations and illustrates how intersection angle is defined.

Table 2.1. Table showing the seven different mobile geofence radii and their intersections with the six different PLDs. The resulting intersection angles are shown.

PLD	Radius (m)	Angle (Degrees)
1	30	0
2	30	90
1	45	0
2	45	42
1	60	0
2	60	30
3	60	90
1	75	0
2	75	24
3	75	53
1	90	0
2	90	19
3	90	42
4	90	90
1	105	0
2	105	17
3	105	35
4	105	59
1	120	0
2	120	14
3	120	30
4	120	49
5	120	90

Beginning at the start point, the route was marked by brightly-colored pin flags every 10 m using a compass and 91-m fiberglass tape. Because the Garmin system does not support mobile geofencing, all of the locations at which the mobile geofence (at all seven radii) would first theoretically intersect each stationary PLD point were calculated. Prior to data collection, a fiberglass tape was used to flag these intersection points along the route. The locations of all flagged points

along the route and of the six stationary PLDs were recorded at the beginning of the experiment using a survey-grade Topcon GR-3 GNSS base station and rover (Topcon Positioning Systems, Tokyo, Japan). This system has a specified accuracy of 10 mm. As the manual faller walked the route, the time at which he or she passed each flag was recorded using a custom script running in the R statistical programming environment [46] on a Windows tablet.

Intersection times recorded in the field represented the times at which the mobile geofence should have first intersected the stationary PLDs. The predicted times of intersection were calculated based on the ellipsoid distance between the GNSS coordinates recorded by the manual faller's PLD and the stationary PLDs using the *distGeo* function in the R *geosphere* package [47]. In order to quantify the magnitude of signal delay, intersection times observed in the field were subtracted from the predicted intersection times using the following formula:

$$D_i = P_i - O_i, \quad (1)$$

where D_i is the delay for the *i*th intersection, P_i is the predicted intersection time for the *i*th intersection calculated using the recorded GNSS coordinates, and O_i is the field-recorded National Institute of Standards and Technology (NIST) time when the faller crossed the *i*th intersection point.

Using this method, positive time delays indicate geofence crossing alerts that would have occurred after the faller had actually crossed the geofence. Likewise, negative delays represent alerts that would have been triggered prior to the faller crossing the geofence. A linear mixed-effects model was used to account for correlation within each block and within each pass along the route because the assumption of within-block independence of errors was not satisfied for conventional analysis of variance (ANOVA). The mixed-effects model was fit using the *lme* function in the R *nlme* package [48]. The model was fit using all factor-level combinations as fixed effects and the block and pass along the route as random effects. The pass along the route was nested within each block. The error correlation was incorporated using an autoregressive structure. ANOVA was used to determine the significance of the fixed effect terms in the model. Normality was an issue with the initial model, so a square root transformation was applied to the intersection delay such that negative delays remained negative and positive delays remained positive.

A simulation script was also written in R to evaluate the geofence alert delay as a mobile geofence intersected a stationary geofence. Eight mobile geofence radii (50, 60, 70, 80, 90, 100, 110, and 120 m) were combined with 91 stationary PLD locations (0–180 m, in 2-m increments) perpendicular to the midpoint of a 500-m route. Each stationary PLD was surrounded by a 50-m radius geofence. The center point of the mobile geofence was advanced in 2-m increments along the

route, with 1000 cycles per treatment. Both the fixed PLD locations and the moving center point of the mobile geofence were assumed to have bivariate Gaussian probability density, such that their intersection was a mixture of the two distributions. This error was applied in R using five standard deviations (1, 2, 3, 4, and 5 m) representing varying levels of GNSS accuracy. To characterize the simulation results, the *nls* function in R [46] was used to fit a non-linear exponential model of the following form:

$$D_{ijkl} = \beta_0 + \beta_1 * e^{(\beta_2 * a_j)} + \beta_3 * s_k + \beta_4 * r_l + \varepsilon_i, \quad (2)$$

where D_{ijkl} is *i*th time delay, a_j is the *j*th intersection angle, s_k is the *k*th standard deviation, and r_l is the *l*th geofence radius.

To better understand the results from both the field experiment and simulation, the proportion of error bearings resulting in early alerts was calculated for the intersection of a mobile geofence with a stationary geofence. We assumed that a GNSS point is equally likely to be moved in 360 directions (bearings) from its true location due to error. Thus, a certain proportion of those potential errors might move the point (and thus the geofence surrounding it) in a way that would cause an early intersection alert. This proportion depends on geofence radius, approach angle, true distance between the two GNSS points, and error magnitude. For our calculations, both geofences had 50-m radii. The mobile and stationary geofences were oriented such that the angle at the true intersection point would be 0°, 22.5°, 45°, 67.5°, and 90°. Within each of these five approach orientations (intersection angles), we placed the mobile geofence at four starting locations (1, 4, 7, and 10 m from the true intersection point) and moved each three distances (1, 3, and 5 m) from this initial location along vectors with bearing angles from 0° to 359°. For each factor-level combination, the proportion of these 360 error angles that resulted in an early alert was calculated.

2.4 Results

2.4.1 Field Results

Incorporating an autoregressive correlation structure into the mixed-effects model of the field results resulted in an improved model with a lower Akaike Information Criterion (AIC) and lower log likelihood ($p < 0.0001$) (Table 2.2). ANOVA on this model showed that the interaction between radius-angle combination and pace ($p < 0.0001$) as well as the radius-angle combination ($p < 0.0001$) affected intersection delay. However, the assumption of normality was not met so the model was refit using a square root transformation of the delay. In the resulting model, ANOVA indicated that only the radius-angle combination affected intersection alert delay ($p < 0.0001$) (Table 2.3).

Table 2.2. Analysis of variance (ANOVA) results comparing models with and without autoregressive error structure. Model 1 was fit without correlated errors while Model 2 was fit with autoregressive error structure.

Model	DF [1]	AIC [2]	BIC [3]	Log Lik [4]	Test	L Ratio [5]	*p*-Value [6]
1	210	4394.911	5325.49	−1987.456	-	-	-
2	211	4162.837	5097.848	−1870.418	1 vs. 2	234.074	<0.0001

[1] Model degrees of freedom; [2] Akaike Information Criterion; [3] Bayesian Information Criterion; [4] Restricted log likelihood; [5] Likelihood ratio; [6] *p*-value associated with likelihood ratio statistic.

Table 2.3. ANOVA results from the full model showing all main effects and interactions. The response was the square root of the alert delay and the model was fit using autoregressive error structure.

Model Term	Num DF [1]	Den DF [2]	*F*-Statistic [3]	*p*-Value [4]
(Intercept)	1	396	8.43367	0.0039
Rad Ang	22	396	76.00023	<0.0001
Pace	2	16	1.24997	0.313
TI	2	16	1.16111	0.3382
RadAng: Pace	44	396	0.937	0.5896
RadAng: TI	44	396	0.83993	0.7571
Pace: TI	4	16	0.60202	0.6667
RadAng:Pace: TI	88	396	1.24072	0.0874

[1] Numerator degrees of freedom; [2] Denominator degrees of freedom; [3] *F*-statistic for Wald tests for model terms; [4] *p*-value associated with Wald tests for model terms.

Alert delay for the entire field experiment ranged from −73 s to 54 s. The most inaccurate alerts tended to be negative and were observed at the slower paces and largest angles. Figure 2.3 illustrates the geofence alert delay as a function of the radius-angle combinations grouped by the three levels of walking pace (30, 45, and 60 bpm). It shows a more negative alert delay, meaning an earlier alert, as the angle of intersection increases. There also appears to be greater variability in the intersection alert delay at slower paces. Finally, the alert delay is less negative at faster paces with the most negative delays occurring at the slowest pace at the largest angles. These more negative delays correspond to earlier hazard alerts.

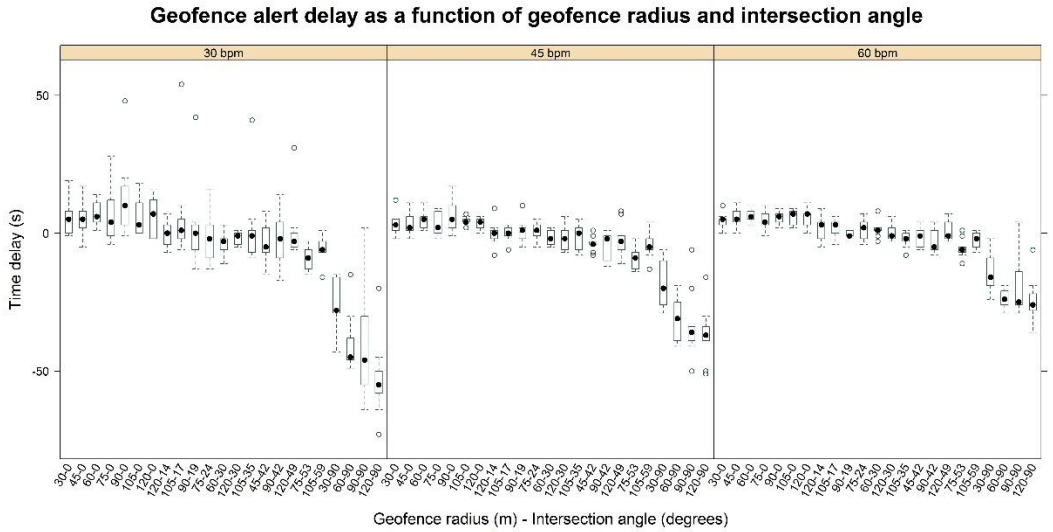

Figure 2.3. Box-and-whisker plot of field results showing geofence intersection alert delay as a function of the geofence radius-intersection angle combinations. The panels are grouped by pace (30, 45, and 60 bpm).

To relate the magnitude of alert delay to distance, Figure 2.4 shows the distance traveled over time as a function of the mean observed speed for each level of walking pace used in the field experiment. For the most positive delay observed (54 s), the faller would have walked 29.4, 42.6, or 56.8 m past the geofence at the 30-, 45-, and 60-bpm paces, respectively. For the most negative delay observed (−73 s), an alert would have been received when the faller was 39.8, 57.6, or 76.8 m from reaching the geofence boundary at the 30-, 45-, and 60-bpm paces, respectively.

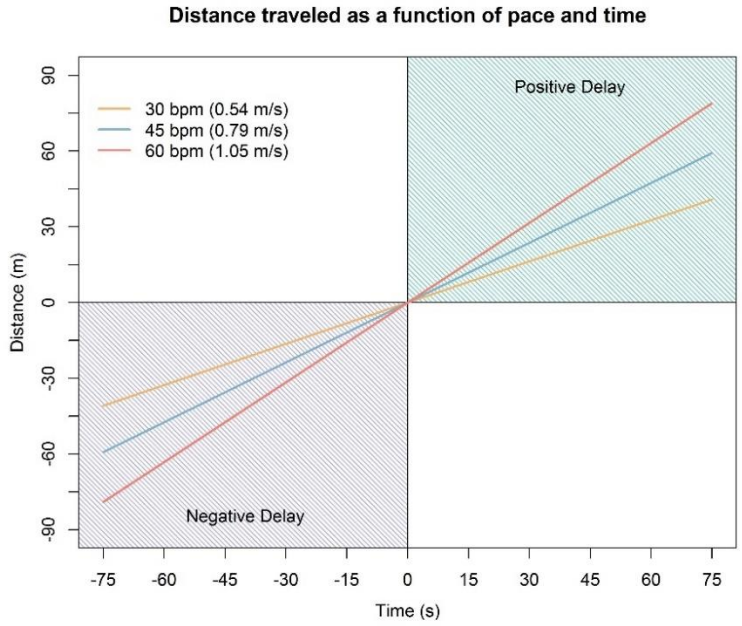

Figure 2.4. Distance traveled over time as a function of walking pace. The slope of each line corresponds to the mean observed speed for each level of pace. Positive distances indicate how far the faller has walked into or past the geofence boundary when the alert is generated (i.e., a positive, late warning). Negative distances indicate how far ahead of the intersection point the faller is when the alert is generated (i.e., a negative, early warning).

2.4.2 Simulation Results

Simulation analysis supported field results, illustrating the effect of intersection angle on geofence alert delay. Figure 2.5 shows the geofence alert delay as a function of intersection angle grouped by radius and GNSS standard deviation. There is more error in the alert delay associated with higher standard deviations and there is a general trend toward more negative delays (earlier alerts) as standard deviation increases. This trend is most noticeable at the larger angles. Also, more negative delays (earlier alerts) occur as intersection angle increases. This pattern is clearest at the larger standard deviations. Finally, in terms of geofence radius, slightly more negative delays were associated with larger radii at the largest intersection angles.

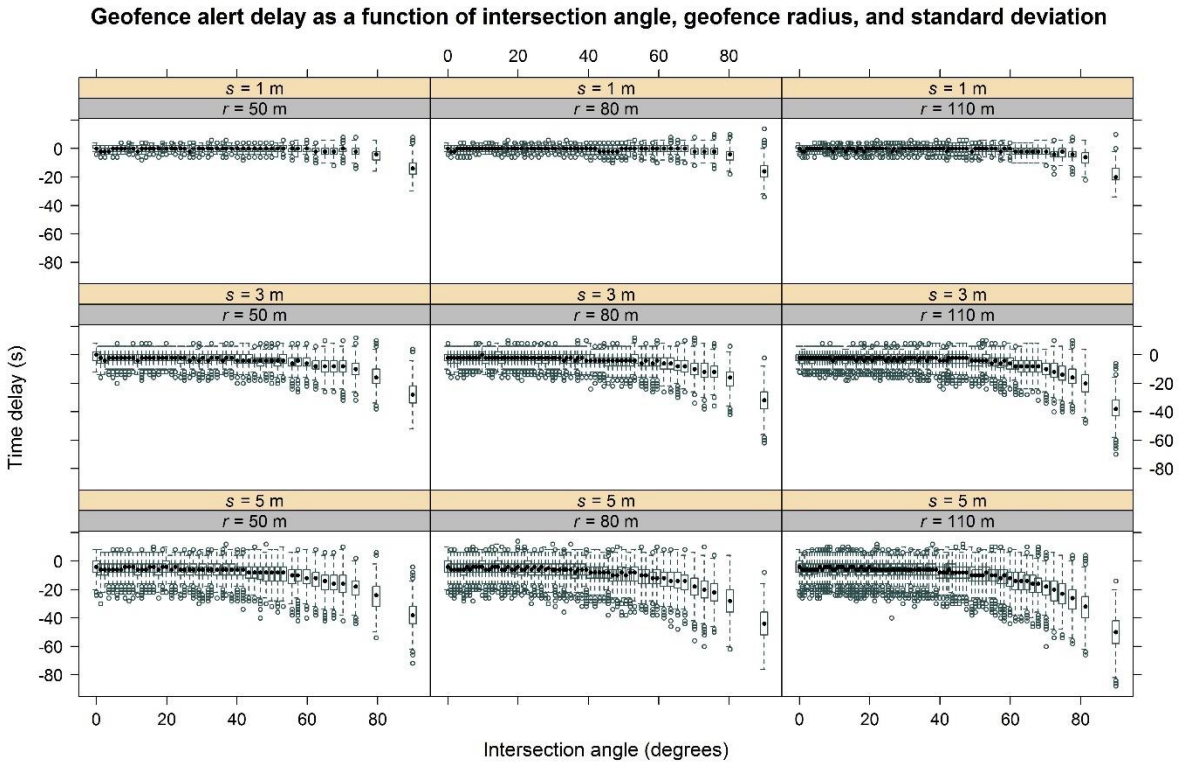

Figure 2.5. Box-and-whisker plot of simulation results showing geofence alert delay as a function of intersection angle grouped by radius and GNSS standard deviation. To improve clarity, the figure is a subset of factor-level combinations, representing three geofence radii (r = 50, 80, and 110 m) and three standard deviations (s = 1, 3, and 5 m). Upper panel numbers are GNSS standard deviation and lower panels represent geofence radii.

Table 2.4 shows the results from the exponential model fitted to the simulation data. All model coefficients had p-values less than 2×10^{-16}.

Table 2.4. Summary of the exponential model (Equation (2)) fitted to the simulation results showing the estimate of each model coefficient, standard errors and p-values.

Parameter	Estimate [1]	Std. Error [2]	t-statistic [3]	p-value [4]
b0	3.86×10^{0}	1.35×10^{-2}	286.41	$<2 \times 10^{-16}$
b1	-5.79×10^{-2}	3.64×10^{-4}	−159.06	$<2 \times 10^{-16}$
b2	6.92×10^{-2}	7.33×10^{-5}	944.50	$<2 \times 10^{-16}$
b3	-2.00×10^{0}	2.03×10^{-3}	−985.52	$<2 \times 10^{-16}$
b4	-4.29×10^{-3}	1.27×10^{-4}	−33.76	$<2 \times 10^{-16}$

[1] Estimated model coefficient; [2] Standard error of estimated model coefficient; [3] t-statistic for each model coefficient; [4] p-value associated with the t-statistic for model coefficients.

Figure 2.6 illustrates how the bearing angle at which error occurs triggers early alerts depending on the intersection angle of stationary and mobile geofences. It is evident in the figure that there is an interaction among circle geometry and the directionality of GNSS error that affects alert timing. There are more possible error bearing angles that result in early alerts as intersection angle increases from 0° to 90°.

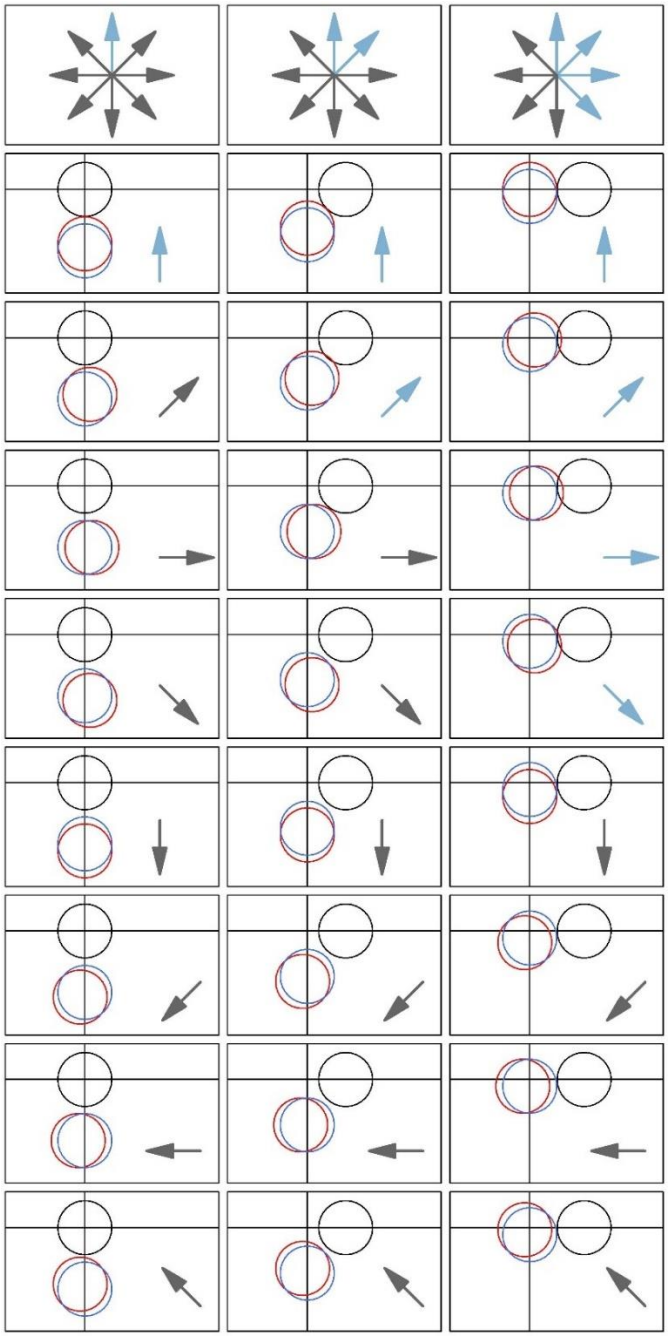

Figure 2.6. Visualization of GNSS error bearings resulting in early alerts. In each cell, the black circle is a stationary geofence and the blue circle represents a mobile geofence located 20 m from its initial intersection point with the stationary geofence. In the first column, the geofence intersection angle will be 0°. In the second and third columns, the intersections will occur at 45° and 90°, respectively. The red circle in each cell illustrates the location of the mobile geofence if it were moved 20 m from its true location, with each row representing one of eight possible directions in which that 20-m error might occur. Arrows in each cell indicate the directionality of error, with light blue arrows indicating movements that result in early intersection alerts. Black arrows indicate movements that do not result in early intersection alerts. The top row depicts all eight error directions in each column below and summarizes which of those directions result in early alerts.

To better demonstrate this effect, additional simulation results shown in Figure 2.7 illustrate the proportion of error bearing angles that result in early alert as a function of the intersection angle

grouped by four starting locations (1, 4, 7, and 10 m from the true intersection point) and three GNSS standard deviations (1, 3, and 5 m). In all cases, the 90° angle has the highest proportion of directional error movements that result in early warning. The difference in this proportion is greatest when the starting location is further from the intersection point. The difference in proportions also varies indirectly with the magnitude of GNSS standard deviation. This is most noticeable at the closest starting locations.

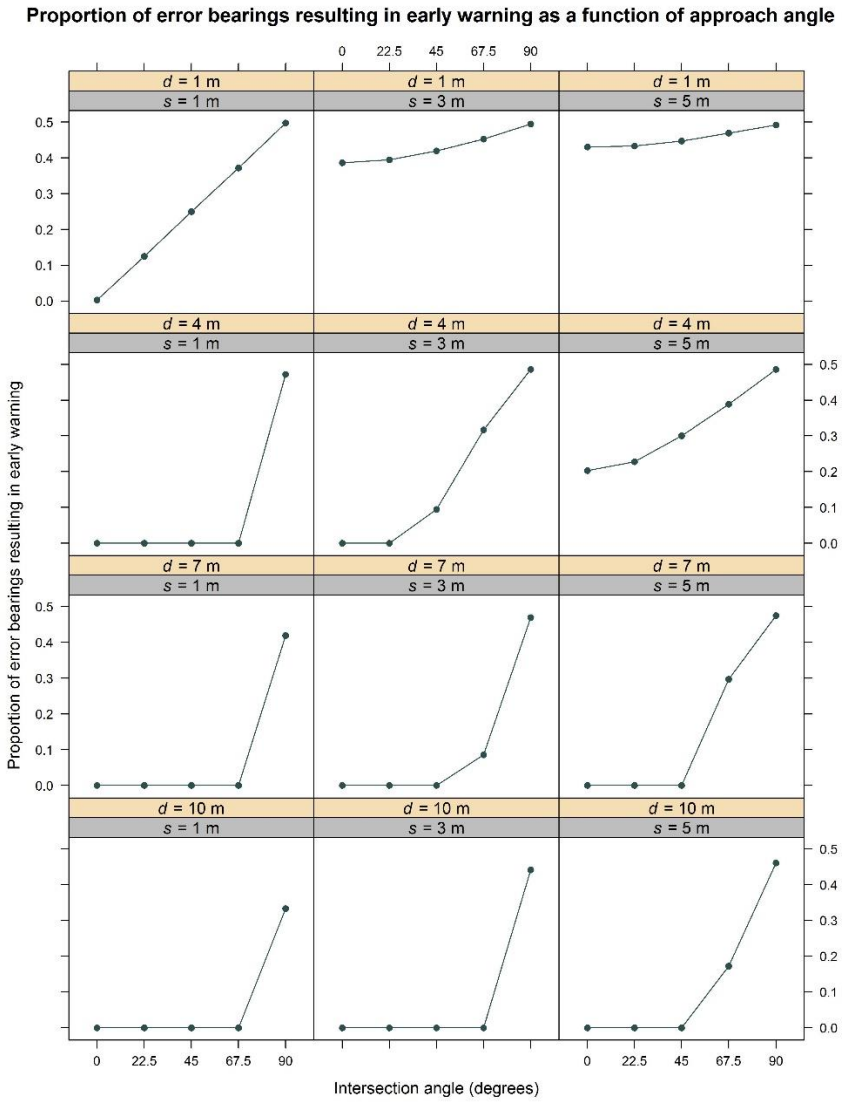

Figure 2.7. Proportion of error bearing angles that result in early alert plotted as a function of the intersection angle. Calculations were done for five intersection angles (0°, 22.5°, 45°, 67.5°, and 90°). The upper panel labels represent the four starting locations (d = 1, 4, 7, and 10 m from the true intersection point) and the lower panels are the three GNSS standard deviations (s = 1, 3, and 5 m).

2.5 Discussion

Results from the field experiment indicate that the realized geofence radius-intersection angle combinations had a significant effect on the alert delay. Similarly, simulation results illustrated the effect of intersection angle on alert delay. Because of the way in which intersection angles were calculated, a 0° angle means the mobile geofence approached the PLD or stationary geofence straight-on, while a 90° angle means the mobile geofence approached alongside the PLD or stationary geofence. In both the field experiment and the simulation, the delay was closest to 0 s at smaller angles. As the angle increased to 90°, delay decreased (became more negative), meaning that an earlier alert was signaled. This effect appears to result from a phenomenon that is evident in Figure 2.7, in which the proportion of directional GNSS error that triggers an early warning depends on angle of intersection approach. In other words, when a mobile geofence approaches a point of interest (PLD) straight-on (i.e., at a 0° angle), only a small proportion of all potential GNSS error results in an early warning. However, when a mobile geofence approaches alongside a PLD (i.e., at a 90° angle), a larger proportion of all potential GNSS error results in early warning. This result has important implications for use of mobile geofences in logging safety because approach angles are constantly changing on active timber sales. This means the accuracy of any alert will vary as worker or equipment positions move around one another at different angles. For instance, if a worker surrounded by a mobile geofence moves straight toward a piece of equipment, the intersection alert may occur with relatively high accuracy. However, if the same worker were to approach alongside the equipment, intersection alert generation may have lower accuracy.

Because of the geofence radii and PLD locations used in the field experiment, not all factor-level combinations of geofence radius and intersection angle were realized. However, simulation results indicate the effect intersection angle has on alert delay, independent of radius. On the other hand, the effect of radius is not as clear. It seems that larger geofence radii trigger slightly earlier alerts at the largest angles but future research is necessary in order to understand this relationship more clearly.

In the field experiment, the delay was more negative at the slowest pace (30 bpm) and became closer to 0 s at the fastest pace (60 bpm). This was primarily noticeable at the largest intersection angles. While this effect was not statistically significant in the mixed-effects model, a moderate influence of pace seems evident graphically in Figure 2.3. A clearer effect of pace on geofence alert timing was observed previously in Grayson et al. [38]. Transmission interval also did not affect delay in the mixed-effects model used to analyze field results, and there were no noticeable

trends in delay at the three transmission intervals evaluated. This result is counterintuitive and may be a consequence of the range of intervals considered.

To continue to advance the use of mobile geofences for delineation of safe work zones in logging and other hazardous occupations with many moving parts, correction methods that account for the effect of intersection angle, and possibly other factors, may be needed. In our study, the absolute point at which GNSS-RF transponders crossed geofence boundaries was assumed to be the appropriate time for a hazard alert to be triggered. However, in practice, alerts would be triggered at earlier warning thresholds in order to provide information about approaching hazards with sufficient time for equipment operators or ground workers to slow down or change course. In further developing the use of mobile geofences to define hazard boundaries and associated safe work areas around workers and equipment, the effect of intersection angle identified in this study will need to be coupled with use of early warning thresholds based on the speed and distance relationships shown in Figure 2.4.

Although the focus of this study was on use of mobile geofences as tree falling hazard zones around manual fallers, there are many other potential safety applications on active logging operations for which mobile geofences could be deployed. For example, mobile geofences could be used to indicate the relative locations of ground workers working at the log landing adjacent to loading and processing equipment, or to indicate the relative proximity of rigging crew workers to the skyline carriage on cable logging operations. As with self-driving vehicle technology used in other fields, an eventual application of mobile geofences to indicate and reduce work-related hazards may be the use of technology not only to provide warnings to ground workers or equipment operators, but to slow or stop equipment function when occupational hazards are imminent.

2.6 Conclusions

Logging continues to be one of the most dangerous occupations in the United States. Real-time positioning has the potential to improve communication and situational awareness on active timber sales. Geofences are an important component of real-time positioning systems. While mobile geofences may be useful in alerting workers when they get too close to jobsite hazards, the accuracy of these alerts may vary depending on angle of approach and GNSS accuracy. Because accuracy and intersection angle change frequently on active logging operations, relying on mobile geofences without application of correction methods is not advised for fine resolution delineation of safe work areas. However, uncorrected mobile geofences may still be appropriate for increasing general

situational awareness among workers at coarser spatial scales. A better understanding of the effects of these factors could inform the development of correction methods to improve alert accuracy and recommendations for use of real-time positioning technology in occupational safety.

2.7 References

1. Sygnatur, E.F. Logging is perilous work. *Compens. Work. Cond.* **1998**, *3*, 3–9.
2. Fosbroke, D.E.; Kisner, S.M.; Myers, J.R. Working lifetime risk of occupational fatal injury. *Am. J. Ind. Med.* **1997**, *31*, 459–467.
3. Sullman, M.J.M.; Kirk, P.M.; Parker, R.J.; Gaskin, J.E. New Zealand logging industry accident reporting scheme: Focus for a human factors research programme. *J. Saf. Res.* **1999**, *30*, 123–131.
4. Wang, J.; Bell, J.L.; Grushecky, S.T. Logging injuries for a 10-year period in Jilin Province of the People's Republic of China. *J. Saf. Res.* **2003**, *34*, 273–279.
5. Axelsson, S.A. The mechanization of logging operations in Sweden and its effect on occupational safety and health. *J. For. Eng.* **1998**, *9*, 25–31.
6. Bell, J.L. Changes in logging injury rates associated with use of feller-bunchers in West Virginia. *J. Saf. Res.* **2002**, *33*, 463–471.
7. Egan, A.F. The introduction of a comprehensive logging safety standard in the USA—The first eighteen months. *J. For. Eng.* **1998**, *9*, 17–23.
8. Bordas, R.M.; Davis, G.A.; Hopkins, B.L.; Thomas, R.E.; Rummer, R.B. Documentation of hazards and safety perceptions for mechanized logging operations in East Central Alabama. *J. Agric. Saf. Health* **2001**, *7*, 113–123.
9. U.S. Bureau of Labor Statistics. Current Population Survey, Census of Fatal Occupational Injuries. 2016. Available online: http://www.bls.gov/iif/oshcfoi1.htm (accessed on 15 January 2017).
10. Keefe, R.F.; Eitel, J.U.H. Applications of carriage-mounted agricultural cameras to improve safety in cable logging operations. In Proceedings of the 2013 Annual Meeting of the Council on Forest Engineering, Missoula, MT, USA, 7–10 July 2013.
11. Wing, M.G.; Eklund, A.; Kellogg, L.D. Consumer-grade global positioning system (GPS) accuracy and reliability. *J. For.* **2005**, *103*, 169–173.
12. Johnson, C.E.; Barton, C.C. Where in the world are my field plots? Using GPS effectively in environmental field studies. *Front. Ecol. Environ.* **2004**, *2*, 475–482.

13. Bettinger, P.; Fei, S. One year's experience with a recreation-grade GPS receiver. *Math. Comput. For. Nat. Resour. Sci.* **2010**, *2*, 153–160.
14. Wing, M.G. Consumer-grade global positioning systems (GPS) receiver performance. *J. For.* **2008**, *106*, 185–190.
15. Wing, M.G. Consumer-grade GPS receiver measurement accuracy in varying forest conditions. *Res. J. For.* **2011**, *5*, 78–88.
16. Andersen, H.E.; Clarkin, T.; Winterberger, K.; Strunk, J. An accuracy assessment of positions obtained using survey- and recreational-grade global positioning system receivers across a range of forest conditions within the Tanana Valley of interior Alaska. *West. J. Appl. For.* **2009**, *24*, 128–136.
17. Reclus, F. Geofencing. In *Geopositioning and Mobility*; Nait-Sidi-Moh, A., Bakhouya, M., Gaber, J., Wack, M., Eds.; Johny Wiley & Sons, Inc.: Hoboken, NJ, USA, 2013; pp. 127–154.
18. Namiot, D. GeoFence services. *Int. J. Open Inf. Technol.* **2013**, *1*, 30–33.
19. Reclus, F.; Drouard, K. Geofencing for fleet & freight management. In Proceedings of the 9th International Conference on Intelligent Transport Systems Telecommunications (ITST), Lille, France, 20–22 October 2009; pp. 353–356.
20. Oliveira, R.R.; Noguez, F.C.; Costa, C.A.; Barbosa, J.L.; Prado, M.P. SWTRACK: An intelligent model for cargo tracking based on off-the-shelf mobile devices. *Expert Syst. Appl.* **2013**, *40*, 2023–2031.
21. Greenwald, A.; Hampel, G.; Phadke, C.; Poosala, V. An economically viable solution to geofencing for mass-market applications. *Bell Labs Tech. J.* **2011**, *16*, 21–38.
22. Martin, D.; Alzua, A.; Lamsfus, C. 2011. A contextual geofencing mobile tourism service. In *Information and Communication Technologies in Tourism 2011, Proceedings of the International Conference in Innsbruck, Austria, 26–28 January 2011*; Law, R., Fuchs, M., Ricci, F., Eds.; Springer: Vienna, Austria, 2011; pp. 191–202.
23. Song, L.; Eldin, N.N. Adaptive real-time tracking and simulation of heavy construction operations for look-ahead scheduling. *Autom. Constr.* **2012**, *27*, 32–39.
24. Pestana, G.; Rebelo, I.; Duarte, N.; Cuoronné, S. Addressing stakeholders coordination for airport efficiency and decision-support requirements. *J. Aerosp. Oper.* **2012**, *1*, 267–280.
25. Wawrzyniak, N.; Hyla, T. Application of geofencing technology for the purpose of spatial analyses in inland mobile navigation. In Proceedings of the 2016 Baltic Geodetic Congress (BGC Geomatics), Gdańsk, Poland, 2–4 June 2016; pp. 34–39.
26. Gill, E.; Fox, B.M.; Kreisel, J. Emerging commercial opportunities based on combined communication-navigation services. *Acta Astronaut.* **2006**, *59*, 100–106.

27. Monteiro, S.; Vázquez, X.; Long, R. Improving fishery law enforcement in marine protected areas. *Aegean Rev. Law Sea Marit. Law* **2010**, *1*, 95–109.
28. Licht, D.S.; Millspaugh, J.J.; Kunkel, K.E.; Kochanny, C.O.; Peterson, R.O. Using small populations of wolves for ecosystem restoration and stewardship. *Bioscience* **2010**, *60*, 147–153.
29. Sheppard, J.K.; McGann, A.; Lanzone, M.; Swaisgood, R.R. An autonomous GPS geofence alert system to curtail avian fatalities at wind farms. *Anim. Biotelemetry* **2015**, *3*, 1–8.
30. Wall, J.; Wittemyer, G.; Klinkenberg, B.; Douglas-Hamilton, I. Novel opportunities for wildlife conservation and research with real-time monitoring. *Ecol. Appl.* **2014**, *24*, 593–601.
31. Butler, Z.; Corke, P.; Peterson, R.; Rus, D. From robots to animals: Virtual fences for controlling cattle. *Int. J. Robot. Res.* **2006**, *25*, 485–508.
32. Anderson, D.M.; Nolen, B.; Fredrickson, E.; Havstad, K.; Hale, C.; Nayak, P. Representing spatially explicit Directional Virtual Fencing (DVF™) data. In Proceedings of the 24th Annual ESRI International User Conference, San Diego, CA, USA, 9–13 August 2004.
33. Luxhøj, J.T. A socio-technical model for analyzing safety risk of unmanned aircraft systems (UAS): An application to precision agriculture. *Proced. Manuf.* **2015**, *3*, 928–935.
34. Carbonari, A.; Giretti, A.; Naticchia, B. A proactive system for real-time safety management in construction sites. *Autom. Constr.* **2011**, *20*, 686–698.
35. Gallo, R.; Grigolato, S.; Cavalli, R.; Mazzetto, F. GNSS-based operational monitoring devices for forest logging operation chains. *J. Agric. Eng.* **2013**, *44*, 140–144.
36. McDonald, T.P.; Fulton, J.P. Automated time study of skidders using global positioning system data. *Comput. Electron. Agric.* **2005**, *48*, 19–37.
37. Keefe, R.F.; Eitel, J.U.H.; Smith, A.M.S.; Tinkham, W.T. Applications of multi transmitter GPS-VHF in forest operations. In Proceedings of the 47th International Symposium on Forestry Mechanization and 5th International Forest Engineering Conference, Gerardmer, France, 23–26 September 2014.
38. Grayson, L.M.; Keefe, R.F.; Tinkham, W.T.; Eitel, J.U.H.; Saralecos, J.D.; Smith, A.M.S.; Zimbelman, E.G. Accuracy of WAAS-enabled GPS-RF warning signals when crossing a terrestrial geofence. *Sensors* **2016**, *16*, 1–8.
39. Becker, R.M.; Keefe, R.F.; Anderson, N.M. Use of real-time GNSS-RF data to characterize the swing movements of forestry equipment. *Forests* **2017**, *8*, 1–15.
40. Guo, C.; Guo, W.; Cao, G.; Dong, H. A lane-level LBS system for vehicle network with high-precision BDS/GPS positioning. *Comput. Intell. Neurosci.* **2015**, *2015*, 1–13.

41. Veal, M.W.; Taylor, S.E.; McDonald, T.P.; McLemore, D.K.; Dunn, M.R. Accuracy of tracking forest machines with GPS. *Trans. ASAE* **2001**, *44*, 1903–1911.
42. Piedallu, C.; Gégout, J.-C. Effects of forest environment and survey protocol on GPS accuracy. *Photogramm. Eng. Remote Sens.* **2005**, *71*, 1071–1078.
43. Jiang, Z.; Sugita, M.; Kitahara, M.; Takatsuki, S.; Goto, T.; Yoshida, Y. Effects of habitat feature, antenna position, movement, and fix interval on GPS radio collar performance in Mount Fuji, central Japan. *Ecol. Res.* **2008**, *23*, 581–588.
44. Turner, L.W.; Udal, M.C.; Larson, B.T.; Shearer, S.A. Monitoring cattle behavior and pasture use with GPS and GIS. *Can. J. Anim. Sci.* **2000**, *80*, 405–413.
45. Cain, J.W., III; Krausman, P.R.; Jansen, B.D.; Morgart, J.R. Influence of topography and GPS fix interval on GPS collar performance. *Wildl. Soc. Bull.* **2005**, *33*, 926–934.
46. R Core Team. *R: A Language and Environment for Statistical Computing*; R Foundation for Statistical Computing: Vienna, Austria, 2016; Available online: https://www.R-project.org/ (accessed on 10 February 2017).
47. Hijmans, R.J. Geosphere: Spherical Trigonometry. R Package version 1.5-5. 2016. Available online: https://CRAN.R-project.org/package=geosphere (accessed on 10 February 2017).
48. Pinheiro, J.; Bates, D.; DebRoy, S.; Sarkar, D.; R Core Team. Nlme: Linear and Nonlinear Mixed Effects Models. R Package version 3.1-130. 2016. Available online: http://CRAN.R-project.org/package=nlme (accessed on 10 February 2017).

Chapter 3: Real-time Positioning in Logging: Effects of Forest Stand Characteristics, Topography, and Line-of-sight Obstructions on GNSS-RF Transponder Accuracy and Radio Signal Propagation

Published In:

Zimbelman EG, Keefe RF. Real-time positioning in logging: Effects of forest stand characteristics, topography, and line-of-sight obstructions on GNSS-RF transponder accuracy and radio signal propagation. PLOS ONE. 2018 Jan;13(1):e0191017. doi:10.1371/journal.pone.0191017.

3.1 Abstract

Real-time positioning on mobile devices using global navigation satellite system (GNSS) technology paired with radio frequency (RF) transmission (GNSS-RF) may help to improve safety on logging operations by increasing situational awareness. However, GNSS positional accuracy for ground workers in motion may be reduced by multipath error, satellite signal obstruction, or other factors. Radio propagation of GNSS locations may also be impacted due to line-of-sight (LOS) obstruction in remote, forested areas. The objective of this study was to characterize the effects of forest stand characteristics, topography, and other LOS obstructions on the GNSS accuracy and radio signal propagation quality of multiple Raveon Atlas PT GNSS-RF transponders functioning as a network in a range of forest conditions. Because most previous research with GNSS in forestry has focused on stationary units, we chose to analyze units in motion by evaluating the time-to-signal accuracy of geofence crossings in 21 randomly-selected stands on the University of Idaho Experimental Forest. Specifically, we studied the effects of forest stand characteristics, topography, and LOS obstructions on (1) the odds of missed GNSS-RF signals, (2) the root mean squared error (RMSE) of Atlas PTs, and (3) the time-to-signal accuracy of safety geofence crossings in forested environments. Mixed-effects models used to analyze the data showed that stand characteristics, topography, and obstructions in the LOS affected the odds of missed radio signals while stand variables alone affected RMSE. Both stand characteristics and topography affected the accuracy of geofence alerts.

3.2 Introduction

Since the Department of Defense launched its first Navigation System with Timing and Ranging (NAVSTAR) satellite in 1978, global positioning system (GPS) technology has become an integral component of national defense, homeland security, civilian life, and scientific research [1]. Global navigation satellite system (GNSS) positioning is a more general term that encompasses all

global satellite-based positioning systems such as GPS, GLONASS, Galileo, and BeiDou. Initial research evaluating the practicality of GNSS technology in forested landscapes indicated the potential use of GNSS for a range of operational and research uses in natural resources [2]. Early assessments of GNSS for forestry found it could be used to locate forest inventory plots [3,4], quickly determine timber harvest unit boundaries [4], locate forest roads [4], and track wheeled skidders [5]. Various other studies tracked harvest equipment with GNSS and used this information to assess site disturbance and to calculate productivity from time-study data [6,7]. More recent studies related to forest operations have analyzed the potential for GNSS data to quantify production efficiency [8], track log trucks [9], improve operational monitoring [10], and increase efficiency and calibrate remotely-sensed inventory data using GNSS-derived harvester head positions [11].

The accuracy of GNSS coordinate readings is dependent upon the number and geometry of satellites visible to a GNSS unit at any point in time. Positional dilution of precision (PDOP) is an index of the influence of satellite geometry on GNSS measurements [12]. In general, a lower PDOP value indicates an arrangement of satellites providing higher measurement reliability and values less than 2 are desirable [12]. PDOP values can be calculated for user-defined locations using GNSS mission planning software [13]. Another factor that could potentially affect GNSS accuracy in forested conditions is aspect. The Wide Area Augmentation System (WAAS) provides real-time GNSS data correction [14]. GNSS receivers need a clear view of a geostationary communications satellite (GEO) in order to receive WAAS correction signals [14]. GNSS receivers in the northern United States usually need an unobstructed view to the south of less than 20 degrees to receive WAAS signals because GEO satellites are low on the horizon [14]. This leads to a potential for increased error on slopes without a clear view to the south [14]. Few studies have evaluated the effect of aspect on GNSS performance, and while two studies found higher GNSS fix rates and lower location error on south aspects, these differences were not statistically significant [15,16].

GNSS use in forestry is often affected by error associated with satellite signal obstruction by the canopy or other solid objects and the reflection or diffraction of satellite signals from nearby objects or surfaces, an error known as multipathing [13,17]. Previous studies have shown that forest stand structural characteristics and terrain affect GNSS accuracy [5,18–23]. Holden et al. developed a method to model GNSS precision using three canopy descriptor variables (percentage of sky obstruction, maximum canopy hole radius, and fragmentation of sky view) [21]. Lewis et al. modeled the proportion of 3D GNSS fixes, PDOP, and location error using the percent canopy cover and satellite view (to represent terrain obstruction) [22]. Newer studies have taken advantage of the correlation between GNSS signal strength and forest stand characteristics by evaluating the potential

to predict and map forest parameters using GNSS signals [24,25]. GNSS receiver type (survey-, mapping-, or recreation-grade) also affects the accuracy of position measurements [5,26–30]. Survey-grade receivers are capable of sub-centimeter accuracy in the open and sub-meter accuracy under mature forest conditions [30,31]. At the other end of the spectrum, recreation-grade units are the least expensive and have accuracies ranging from 2 – 5 m in the open [13,32–34] to 3.8 – 12 m in mature forests [13,30,32–34].

Advances in positioning technology for remote environments have emerged simultaneously for several uses, ranging from recreation to public safety and defense. These devices link GNSS positional information with radio frequency (RF) transmission of location coordinates (GNSS-RF) to form ad-hoc networks in which the locations of all units can be monitored on mobile phones or tablets. Like traditional GNSS devices, each GNSS-RF transponder determines its coordinates using one or more satellite-based positioning systems. However, the RF transmission is a second component that allows those coordinates to be sent to other, nearby GNSS-RF units at user-defined intervals. GNSS-RF transponders include consumer-grade units for recreational use like the Garmin Rino and Garmin Alpha 100, devices such as the Raveon Atlas PT marketed for public safety, a variety of military-grade GNSS radios designed for defense applications, and consumer-grade mobile-based solutions from goTenna and Beartooth that turn smartphones into two-way radios for voice or text communication in areas without cellular service. While traditional GNSS devices allow users to see their own positions, GNSS-RF devices enable real-time positioning through location sharing among individuals and equipment in remote locations [8,23,35–37]. Thus, either the device's native screen or an attached tablet can display the location of other devices in the network moving in real-time.

Many GNSS-RF transponders support geofencing, in which a virtual boundary is defined around a user-defined geographic zone. Geofences are either circular or polygonal in shape, can vary widely in size depending on intended application, and can be stationary or mobile. Alert notifications are triggered as tracked mobile objects cross into or out of the geofence, and this functionality may be useful for a range of operational forestry applications such as detecting the amount of time workers spend near cable logging hazards [23], signaling when log skidders or log trucks cross harvest unit boundaries [36], and delineating tree falling hazard zones around manual fallers [37]. GNSS-RF real-time positioning and geofences have the potential to improve communication and situational awareness on logging operations, in wildland firefighting, transportation, and recreation. In this study, our focus was on logging safety, as logging is consistently ranked as one of the most hazardous occupations in the United States [38], with the highest fatal work injury rate of civilian occupations in

2015 [39]. By increasing situational awareness, the active display of real-time positioning logistics may be able to reduce hazards posed by the frequent interactions among ground workers, heavy equipment, and irregular terrain that are common on active logging operations.

GNSS-RF and related technologies pose new challenges for quantifying positional accuracy because positional error is associated with both the accuracy of GNSS locations and successful propagation of radio signals between devices. In other words, the accuracy of GNSS-RF position sharing depends not only on factors that influence GNSS accuracy as described above, but also on factors that affect radio signal propagation and attenuation. Radio signals experience diffraction, scattering and reflection as they travel through vegetation [40–42]. Leaf state and vegetation depth and density influence radio signal attenuation [42–45]. Attenuation can also be affected by wind [42,43,46], humidity [47,48], rain [46], and terrain [49,50]. It is unclear whether the same factors affect both the GNSS and RF components of emerging technologies, or if different forest stand characteristics and topographic factors affect one or the other.

The purpose of this study was to characterize the factors affecting real-time positioning on irregular, forested terrain through analysis of the effects of forest stand characteristics, topography and other line-of-sight (LOS) obstructions on the GNSS accuracy and radio signal propagation quality of multiple Raveon Atlas PT GNSS-RF transponders (Raveon Technologies, Vista, California, USA) functioning as a network. Until recently, most previous research evaluating GNSS for forestry applications has focused on stationary units. Recent studies characterizing GNSS units in motion include work by Kaartinen et al. and Liu et al. [11,24], while others have quantified mobile GNSS units paired with RF-based transmission [8,23,36,37]. To further our understanding of location sharing among mobile GNSS units, we evaluated the time-to-signal accuracy of geofence crossing alerts in 21 randomly-selected stands on the University of Idaho Experimental Forest, under a wide spectrum of stand and topographic conditions. Time-to-signal accuracy refers to the difference between when a person or object crosses a geofence and when the alert is generated and shared with other, nearby GNSS-RF devices. Specifically, we tested three hypotheses. Our first null hypothesis was that neither forest stand characteristics, topography, nor the presence of obstructions in the line-of-sight affected the probability of successful radio signal propagation between GNSS-RF units. We tested this by analyzing the odds of missed radio signals within each stand using mixed-effects logistic regression. Our second null hypothesis was that neither stand characteristics, topography, nor physical obstructions affected the stationary positional accuracy of GNSS-RF units. To test this, we used linear mixed-effects models to determine which factors most affected root mean squared error (RMSE) of the PT. Our third null hypothesis was that neither stand characteristics, topography, nor

physical obstructions affected the time-to-signal accuracy of geofence crossings. We tested this by using linear mixed-effects models to determine which factors most affected geofence intersection alert delay.

3.3 Materials and methods

3.3.1 Field experiment

Five Raveon Atlas PT GNSS-RF transponders collected positional data during the field experiment. As GNSS-RF units, the PTs receive their coordinates and then transmit that information to other PTs using radio frequency. The units can be attached to tablets or computers, which allows ground workers and equipment operators on logging operations to see all other positioning devices in real-time. PTs receive their coordinates from NAVSTAR GPS satellites only and have a specified 24-hour static accuracy of < 2.5 m for 50% of measurements and of < 5 m for 90% of measurements [51]. Depending on terrain, the devices can communicate up to 48 km away and position updates can be transmitted as frequently as one signal per second [51]. PTs can be used with Raveon RavTrack software, which has several options for geofencing, including different notification options.

In this study, real-time geofence alert signals were evaluated in a random sample of 21 stands on the University of Idaho Experimental Forest (UIEF) (Figure 3.1A). Only stands ≥ 2.02 hectares (5 acres) in size were selected. Within each stand, the timing of geofence alerts was characterized for a manual faller entering a 100 m × 300 m rectangular geofence (Figure 3.1B). In addition to placing one stationary PT at the geofence intersection point (Atlas PT X in Figure 3.1B) to record data, a compass and 100-m fiberglass tape were used to place three other PTs 100 m from the virtual boundary intersection point at angles forming the vertices of an equilateral triangle (Atlas PTs A, B, and C at triangle points A, B, and C, respectively, in Figure 3.1B). The first of these stationary PTs (PT A) was placed at a randomly selected bearing from the intersection point (triangle point A). The bearing was sampled from the set of whole numbers between 1 and 360, with replacement. The remaining two stationary PTs (PTs B and C) were placed 120° and 240° clockwise, respectively, from this first PT (triangle points B and C, respectively). All stationary PTs were zip-tied to wooden stakes such that the bottoms of their antennas were 1 m above the ground surface. Each stationary PT was attached to a Windows 10 Dell Venue 8 Pro tablet running Raveon RavTrack software. Finally, maps for each stand were loaded onto the tablets using 1-m resolution National Agriculture Imagery Program (NAIP) images downloaded from The National Map website [52] and all tablets were synced with the National Institute of Standards and Technology (NIST) time server [53] each day.

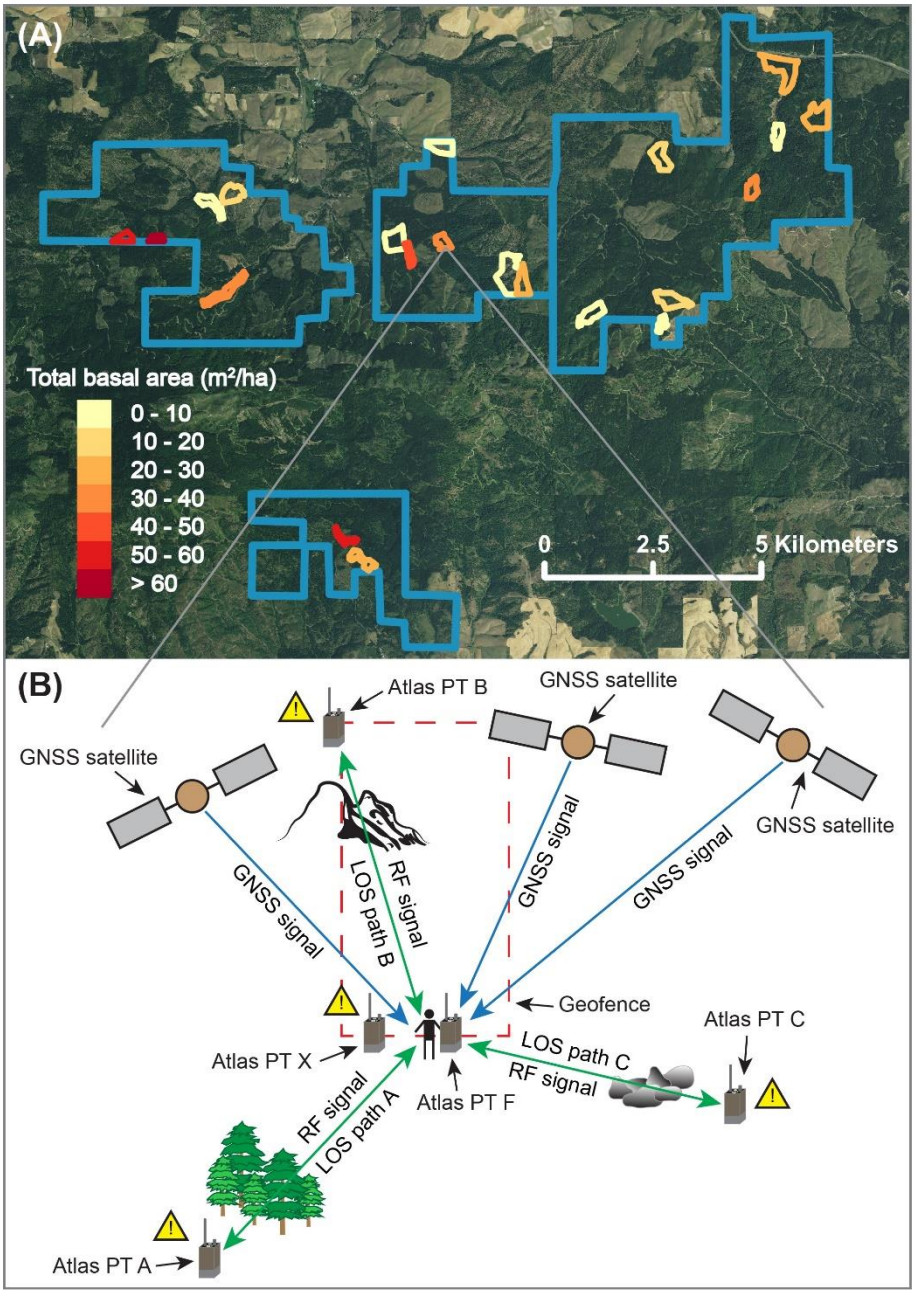

Figure 3.1. Map of the stand locations on the UIEF and illustration of the experimental setup. (A) The 21 stands are delineated according to total basal area (m^2/ha) and the UIEF unit boundaries are shown in blue. Background map is 1-m NAIP imagery. (B) Illustration of global navigation satellite system (GNSS) technology paired with radio frequency (RF) transmission (GNSS-RF). GNSS-RF transponders (Atlas PTs) receive positional information from GNSS satellites and relay this information to one another using radio frequency transmission. Atlas PT X is located at the geofence intersection point, while Atlas PTs A, B, and C are located at the triangle points A, B, and C, respectively. The manual faller carried a PT attached at the hip (Atlas PT F).

The orientation of geofence crossing in each stand was also randomly selected from the sample of whole numbers between 1 and 360, with replacement. A rectangular geofence was established in each stand using a Suunto sight-through azimuth compass, fiberglass tape, and an Eos

Arrow 100 GNSS unit (Eos Positioning Systems, Terrebonne, Quebec, Canada) with a specified accuracy of < 0.6 m [54]. One side of the geofence was centered at the geofence intersection point and was oriented perpendicular to the crossing direction. The geofence was 100 m wide at the crossing point and 300 m long.

In each stand, a manual faller carrying a PT attached at the belt crossed the geofence once by walking a 90-m route oriented perpendicular to the geofence (i.e., in the chosen geofence crossing direction), starting and ending 45 m from the intersection point. For consistency, the manual faller walked at a pace of 45 bpm, as dictated by a digital metronome. The route was established using a compass and 50-m fiberglass tape and was marked with pin flags. The observed time at which the faller crossed the geofence was recorded in the field using a custom script in R [55] running on a Windows 10 Dell Venue 8 Pro tablet synced with the NIST time server. The predicted intersection times were recorded by the tablets attached to each stationary PT (PTs A, B, C, and X). All PTs were set to collect and transmit their coordinates at a rate of once per second.

Within each stand, topographic, physical, and vegetative obstructions present along each LOS path between the geofence intersection point and the PTs located at triangle points A, B, and C were quantified during setup using a modification of the FIREMON line intercept method [56]. To mark the LOS path, a 100-m fiberglass tape was attached to two metal stakes. One stake was located at the intersection point and the second was located where the stationary PT would be placed during the experiment. The tape was secured to these two stakes and stretched taught 1 m above the ground to match the location of the stationary PT antenna height. This height was approximately equal to that of a PT when worn by a ground worker on a belt clip. The start of the tape was attached to the stake at the intersection point while the end was attached to the stake at the triangle point. For each LOS path, three 5-m sections were randomly selected from the segments shown in Figure 3.2 and all vegetative obstructions in these sections were classified using the key in Table 3.1. Only obstacles physically touching the fiberglass tape were quantified. To measure each obstacle, two meter sticks were used to hold the tape 1 m above the ground. The first meter stick was located 1 m before the start of the obstacle and the second meter stick was located 1 m past the end of the obstacle. Once the fiberglass tape was in position, the two locations at which the obstacle first and last contacted the tape were recorded to the nearest centimeter. Obstacles less than 5 cm in size (as measured along the LOS path) were not quantified. When gaps were present between nearby obstacles, the obstacles were treated as two separate obstacles only when the gap was greater than 25 cm. Obstructions less than 1 m tall were not quantified and trees that were less than 12.5-cm diameter at breast height (DBH) were classified

as coniferous vegetation. To simplify analysis, vegetative obstructions within the three measured 5-m sections were summarized using Eq (1):

$$V_i = S_i + C_i + T_i + W_i + SC_i + SW_i + CW_i \quad (1)$$

Where V_i is the measured distance of all vegetative obstructions recorded for the three 5-m sections along the *i*th LOS path. S_i, C_i, T_i, W_i, SC_i, SW_i, and CW_i represent the distance of vegetative obstructions defined in Table 3.1 as measured in the three 5-m sections along the *i*th LOS path. Then, to account for the fact that only 15 m of each 100-m LOS path was measured, the total distance of vegetation along each path was calculated using Eq (2):

$$TV_i = \frac{V_i}{0.15} \quad (2)$$

Where TV_i represents the total distance of vegetation along the entire *i*th LOS path and V_i is the measured distance of all vegetative obstructions recorded in the three 5-m sections along the *i*th LOS path (Eq (1)). Lastly, all boulders, streams, and forest roads were recorded as present or absent along each LOS path, regardless of their location on the path. These were recorded because of the effects they may have as terrain changes. However, because only one boulder was measured in the LOS paths, we removed it from analysis.

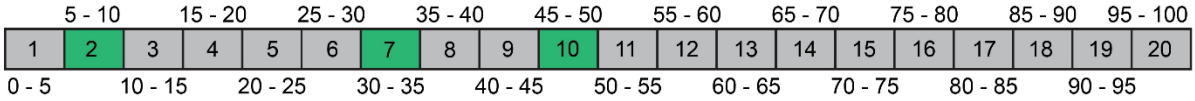

Figure 3.2. LOS path sections. Each LOS path was divided into 20 5-m sections and three sections were randomly selected for each LOS path. This figure shows the 20 sections and their locations along the LOS path. Sections highlighted in green represent the three randomly selected sections for which all vegetative obstructions were measured using the key in Table 3.1.

Table 3.1. Obstacle list and key.

Obstacle ID	**Vegetative Obstruction**
S	Deciduous shrub
C	Coniferous vegetation
T	Tree (stem)
W	Coarse woody debris (CWD)
SC	Deciduous shrub/coniferous vegetation
SW	Deciduous shrub/CWD
CW	Coniferous vegetation/CWD

Once all obstructions were quantified and recorded, each LOS path was walked carrying a Garmin Alpha 100 GNSS-RF unit (Garmin, Olathe, Kansas, USA) to record the vertical elevation

profile. Using the Garmin data, each LOS path was classified in terms of the presence or absence of concavity and convexity. A LOS path was concave if the minimum elevation along the path was at least 3 m below the lower of the two path endpoints. A LOS path was convex if the maximum elevation along the path was at least 3 m above the higher of the two path endpoints. The classification criteria for concavity and convexity is illustrated in Figure 3.3. The percent slope and aspect were also measured at the geofence intersection point. Aspect was measured as a continuous circular variable, but was reclassified as either N (316° – 45°), E (46° – 135°), S (136° – 225°), or W (226° – 315°). Trimble's GNSS mission planning website [57] was used to determine the predicted PDOP values for each day during the experiment. Sampling was only conducted during times with predicted PDOP values less than 4.5 to ensure consistency.

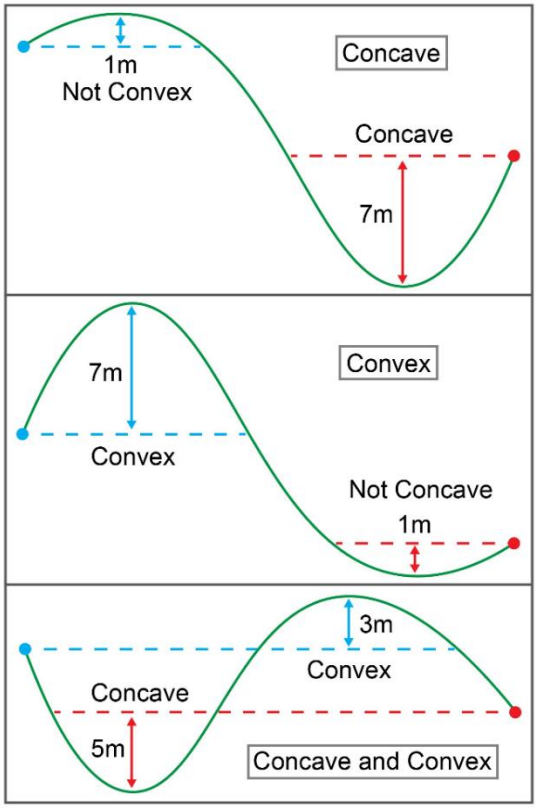

Figure 3.3. Illustration of slope classification as concave, convex, or both. Blue dots represent the higher of the two LOS endpoints while red dots represent the lower of the two LOS endpoints. Green lines represent the ground surface along the LOS path.

To quantify forest stand characteristics, a 0.03-hectare fixed-area plot was established in each stand, centered at the intersection point. The DBH, total height, and height to the base of the live crown were quantified for all trees ≥ 12.5-cm DBH within the plot. Using these measurements, total basal area (TBA), trees per hectare (TPH), mean height (Ht), and quadratic mean diameter (QMD) were calculated for each stand and used as variables representing forest stand characteristics during

analysis. Quadratic mean diameter is a commonly used metric in forestry that refers to the diameter of the tree of mean basal area (stem cross-sectional surface area), as measured at breast height (1.37 m). QMD is calculated as the square root of the squared stem diameters divided by the number of stems sampled, as defined in Eq (3):

$$QMD = \sqrt{\sum_{i=1}^{n} \frac{{D_i}^2}{n}} \tag{3}$$

Where D_i is the DBH of the *i*th tree and *n* is the number of trees sampled.

To quantify missed radio signals in each stand, the number of missed position updates transmitted from the faller's PT (PT F) to the three PTs at the triangle points (PTs A, B, and C) was calculated for the 90-s interval centered on the observed geofence intersection time. Because all units were set to transmit their coordinates at 1-s intervals, 90 position updates would have been received in this time period in the absence of missed signals.

Stationary GNSS accuracy was summarized using RMSE, which is a common measure of GNSS positional error and represents the difference between the predicted and observed coordinates of a GNSS unit. In each stand, the predicted coordinates were obtained using the stationary PT located at the geofence crossing point (denoted as Atlas PT X in Figure 3.1B). These coordinates were collected once per second for 5 min prior to the time of geofence crossing. The observed (true) coordinates for each of these PTs were obtained using the Eos Arrow 100 GNSS unit described above. All coordinates were converted to the Universal Transverse Mercator (UTM) projection and then the RMSE for each stationary PT was calculated using Eq (4):

$$RMSE_i = \sqrt{\sum_{i=1}^{n} ((x_i - \hat{x}_{ij})^2 + \left(y_i - \hat{y}_{ij}\right)^2)/n} \tag{4}$$

Where $RMSE_i$ is the RMSE value in the *i*th stand, x_i is the observed easting value in the *i*th stand (i.e., the Arrow 100 easting coordinates), $\hat{x}_{ij}$ is the *j*th predicted easting value in the *i*th stand (i.e., the PT easting coordinates), y_i is the observed northing value in the *i*th stand (i.e., the Arrow 100 northing coordinates), $\hat{y}_{ij}$ is the *j*th predicted northing value in the *i*th stand (i.e., the PT northing coordinates), and *n* is the total number of PT signals received in the *i*th stand.

The overall geofence intersection alert delay for each stand was derived by averaging the time-to-signal delay calculated at each of the three triangle points (A, B, and C) (Eq (5)):

$$D_i = \frac{(P_{ij} - O_i) + (P_{ik} - O_i) + (P_{il} - O_i)}{3} \quad (5)$$

Where D_i is the overall delay for the geofence intersection in the *i*th stand and O_i is the observed time at which the faller crossed the geofence in the *i*th stand, as recorded in the field. P_{ij} is the predicted intersection time in the *i*th stand at the *j*th triangle point, represented by the recorded alert at triangle point A. P_{ik} is the predicted intersection time in the *i*th stand at the *k*th triangle point, represented by the recorded alert at triangle point B. P_{il} is the predicted intersection time in the *i*th stand at the *l*th triangle point, represented by the recorded alert at triangle point C. Using this formula, positive delays indicate geofence crossing alerts that were triggered after the faller crossed the geofence and negative delays indicate geofence crossing alerts that occurred before the faller intersected the geofence. We used time-to-signal delay as an integrated measure of the accuracy of mobile GNSS units sharing their locations, which differs from RMSE calculated by Kaartinen et al. using known reference points along a path [11].

3.3.2 Analysis of missed radio signals

To test the null hypothesis that the probability of successful GNSS-RF signal propagation was not related to forest stand characteristics, topography, or obstructions in the line-of-sight, a binomial generalized linear mixed-effects model was used to evaluate relationships between the odds of missed signals as a function of vegetative LOS obstructions, topography, and forest stand characteristics. The model was fitted using the glmer function in the R lme4 package [58]. Variables included as fixed effects were the total distance of vegetation along each LOS path (TV_i), TBA, TPH, Ht, QMD, slope, aspect, and the presence or absence of forest roads, streams, convex slopes, and concave slopes (Table 3.2). These variables were included because of their potential effect on the successful propagation of radio signals. To avoid errors with model convergence, the TPH variable was multiplied by a scalar of 0.01. The stand was used as a random effect to account for unobserved variation between stands. The response was the log odds of missed position updates along each LOS path during the 90-s interval centered around the observed geofence intersection time.

Table 3.2. Model parameters.

Variable	**Category**
TV_i[a]	LOS obstruction
TV_{mean}[b]	LOS obstruction
TBA	Forest stand characteristic
TPH	Forest stand characteristic
Ht	Forest stand characteristic
QMD	Forest stand characteristic
Slope	Topography
Aspect	Topography
Presence/absence of forest roads	Topography

Presence/absence of streams	Topography
Presence/absence of convex slopes	Topography
Presence/absence of concave slopes	Topography

[a] TV_i was used only in the analysis of missed radio signals.

[b] TV_{mean} was used only in the analysis of RMSE and geofence intersection alert delay.

3.3.3 Analysis of RMSE

A linear mixed-effects model was also used to test the null hypothesis that neither forest stand characteristics, topography, nor physical obstructions affected GNSS accuracy. The model was fitted using the lmer function in the R lme4 package [58] using the day on which sampling occurred as a random effect to account for variation between days, as might occur due to changing satellite availability and geometry. Variables included as fixed effects in this model were total vegetation (TV_{mean}), TBA, TPH, Ht, QMD, slope, aspect, and the presence or absence of forest roads, streams, convex slopes, and concave slopes (Table 3.2). TV_{mean} for each stand was calculated by averaging the total distance of vegetation (TV_i) from the three LOS paths within each stand. Also, because variables recorded as either present or absent (forest roads, streams, convex slopes, and concave slopes) were quantified along each LOS path, these variables were also considered to be present in this stand-level analysis if they were present along any of the LOS paths. The response variable was the PT RMSE in each stand ($RMSE_i$) calculated using Eq (4).

3.3.4 Analysis of geofence intersection alert delay

To test the null hypothesis that neither forest stand characteristics, topography, nor physical obstructions affected the time-to-signal accuracy of geofence crossings, a linear mixed-effects model was used to quantify relationships between the magnitude of geofence intersection alert delay as a function of forest stand characteristics, topographic structure, and vegetative LOS obstructions. The model was fitted using the lmer function in the R lme4 package [58] using the day on which sampling occurred as a random effect to account for variation between days, as might occur due to changing satellite availability and geometry. Variables included as fixed effects were total vegetation (TV_{mean}), TBA, TPH, Ht, QMD, slope, aspect, and the presence or absence of forest roads, streams, convex slopes, and concave slopes (Table 3.2). TV_{mean} for each stand was calculated by averaging the total distance of vegetation (TV_i) from the three LOS paths within each stand. Also, because variables recorded as either present or absent (forest roads, streams, convex slopes, and concave slopes) were quantified along each LOS path, these variables were also considered to be present in this stand-level analysis if they were present along any of the LOS paths. The response variable was the overall intersection alert delay in each stand (D_i) calculated using Eq (5).

3.3.5 Model selection

For each of the three analyses, a full model was first fitted to the data using all fixed effect terms. These fixed effects were removed one at a time in order of highest *p*-values. The aictab function in the R AICcmodavg package [59] was used to compare all resulting models and the model with the lowest corrected Akaike Information Criterion (AICc) was selected. In terms of the geofence alert delay model, the first two models with the lowest AICc had fixed effect terms that were not significant (*p*-values > 0.05), in which case the model with the third lowest AICc was selected as the final model because all fixed effects had *p*-values ≤ 0.05. Inferences about all three final models were made using the lincon function in the R trtools package [60], which provides point estimates, standard errors, 95% confidence intervals, and *p*-values for each model term. In the case of the logistic regression model, the point estimates, standard errors, and confidence intervals were exponentiated to represent the effect of each variable on the odds of getting a missed signal.

3.4 Results

3.4.1 Analysis of missed radio signals

The proportion of missed radio signals ranged from 0/90 to 20/90, with a mean of 3.30/90. The mixed-effects logistic regression model with the lowest AICc had total distance of vegetation along the LOS path (*TVi*), TPH*0.01, convex, stream, road, and aspect as fixed effects (Table 3.3). All fixed effects affected the odds of missed signals ($p \leq 0.05$). The odds of a missed signal decreased by a factor of 0.93 per unit increase in *TVi* ($p = 5.65 \times 10^{-7}$), while the odds of a missed signal increased by a factor of 1.10 per unit increase in TPH*0.01 ($p = 1.45 \times 10^{-3}$). The odds of a missed signal were 1.61 times higher when a slope was convex vs. not convex ($p = 3.58 \times 10^{-2}$) and 2.00 times higher in the presence of roads ($p = 2.34 \times 10^{-5}$). In the presence of streams, the odds of a missed signal decreased by a factor of 0.66 ($p = 3.16 \times 10^{-2}$). The odds of a missed signal were 1.05 times higher on east, 2.17 times higher on north, and 2.92 times higher on west aspects (as compared to south aspects), although this effect was only significant on north ($p = 9.99 \times 10^{-3}$) and west ($p = 1.65 \times 10^{-4}$) aspects.

Table 3.3. Summary of mixed-effects logistic regression model using stand as a random effect and the odds of missed position updates as the response.

Model term	Estimate	SE	Lower CI	Upper CI	*t*-value	DF	*p*-value
(Intercept)	0.0187	0.2759	0.0109	0.0321	−14.4247	Inf	3.6198×10^{-47}
TV_i	0.9331	0.0138	0.9082	0.9588	−5.0028	Inf	5.6502×10^{-07}
TPH*0.01	1.1048	0.0313	1.0391	1.1747	3.1837	Inf	1.4539×10^{-03}
Convex[a]	1.6084	0.2264	1.0320	2.5067	2.0989	Inf	3.5823×10^{-02}
Stream[a]	0.6552	0.1967	0.4455	0.9634	−2.1495	Inf	3.1597×10^{-02}
Forest road[a]	2.0042	0.1644	1.4522	2.7659	4.2298	Inf	2.3395×10^{-05}

Aspect (E)	1.0531	0.3147	0.5683	1.9515	0.1644	Inf	8.6941×10^{-01}
Aspect (N)	2.1718	0.3011	1.2038	3.9182	2.5761	Inf	9.9911×10^{-03}
Aspect (W)	2.9186	0.2843	1.6719	5.0950	3.7679	Inf	1.6464×10^{-04}

Coefficient estimates, standard errors, and lower and upper bounds have been exponentiated to be on the odds scale.

[a] Indicator variables represent the presence of each respective feature.

3.4.2 Analysis of RMSE

RMSE ranged from 1.81 m to 16.69 m, with a mean of 6.61 m. For the RMSE analysis, the mixed-effects model with the lowest AICc had Ht and QMD as fixed effects, both of which affected RMSE ($p \leq 0.05$) (Table 3.4). The RMSE increased as Ht increased ($p = 9.15 \times 10^{-6}$) but varied indirectly with QMD ($p = 3.02 \times 10^{-3}$). Figure 3.4 illustrates the relationships between predicted RMSE as a function of the two explanatory variables included in the final mixed-effects model.

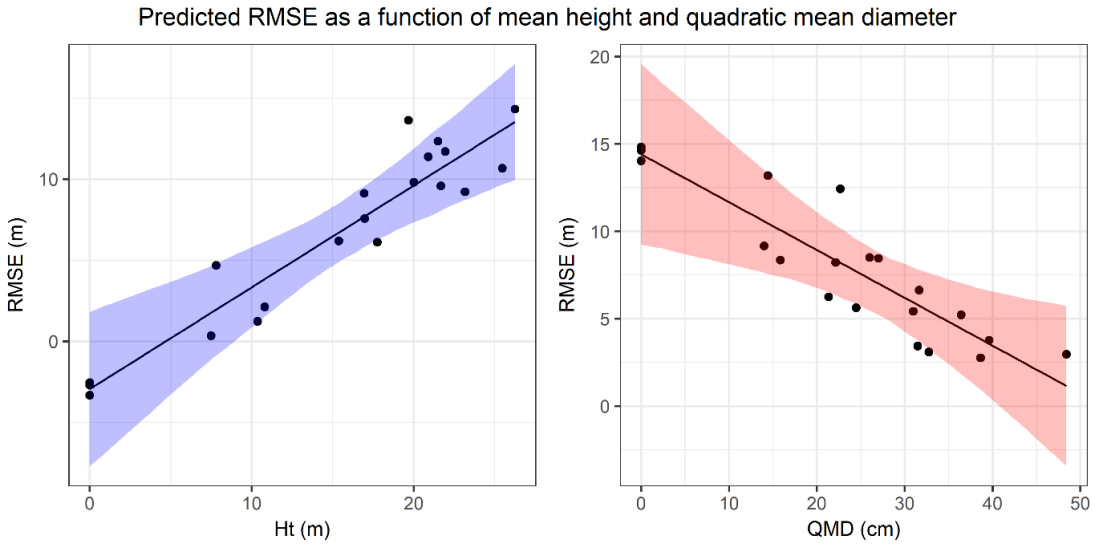

Figure 3.4. Mixed-effects model predictions for PT RMSE. Predicted RMSE as a function of the two model variables (Ht and QMD). Predictions for each variable were made using the mean of the other predictor. 95% confidence intervals computed using the bootstrap are shown as colored bands. Points on each plot represent partial residuals.

Table 3.4. Summary of mixed-effects linear regression model using day as a random effect and RMSE as the response.

Model term	**Estimate**	**SE**	**Lower CI**	**Upper CI**	***t*-value**	**DF**	***p*-value**
(Intercept)	3.7528	1.2790	1.2461	6.2595	2.9343	Inf	3.3435×10^{-03}
Ht	0.6276	0.1415	0.3503	0.9048	4.4363	Inf	9.1526×10^{-06}
QMD	−0.2737	0.0923	−0.4547	−0.0928	−2.9653	Inf	3.0243×10^{-03}

3.4.3 Analysis of geofence intersection alert delay

Geofence intersection alert delay ranged from −5.33 s to 66 s, with a mean of 18.62 s. The final mixed-effects model used to analyze the delay had TBA, concave, and aspect as fixed effects (Table 3.5). This model had the third lowest AICc, but was chosen because the two models with lower AICc values each had model terms that were not significant ($p > 0.05$). The geofence intersection alert delay increased as TBA increased ($p = 6.49 \times 10^{-4}$) and was also higher in the presence of concave slopes when compared to slopes that were not concave ($p = 2.46 \times 10^{-2}$). Finally, the delay was smaller on east, north, and south aspects (as compared to west aspects), although this effect was only significant on east aspects ($p = 1.83 \times 10^{-2}$). Figure 3.5 illustrates the relationships between the predicted alert delay as a function of the three explanatory variables included in the final mixed-effects model.

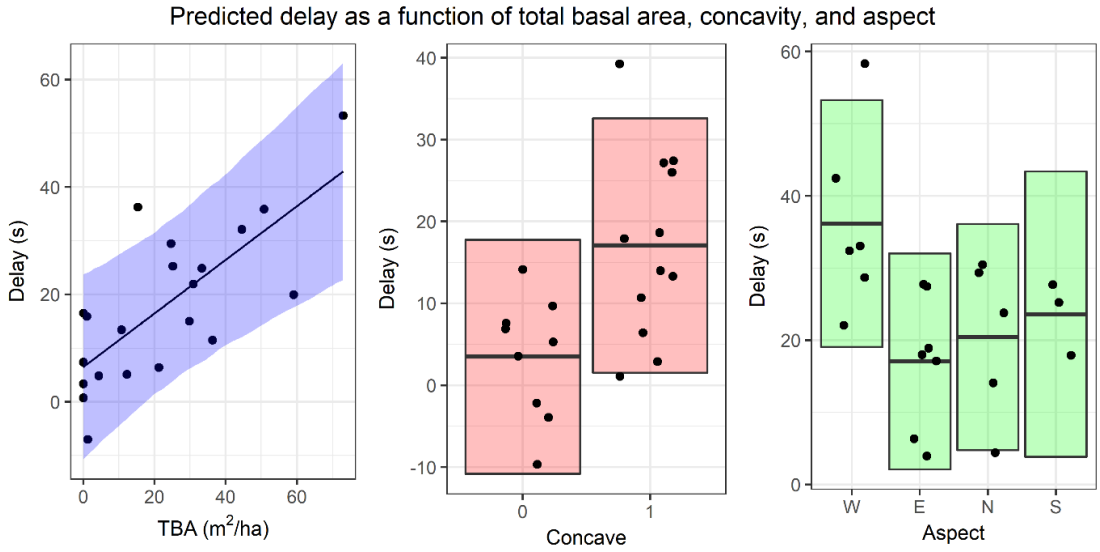

Figure 3.5. Mixed-effects model predictions for geofence intersection alert delay. Predicted delay as a function of the three model variables (TBA, concave, and aspect). Predictions for each variable were made using the mean of the other predictors. 95% confidence intervals computed using the bootstrap are shown as colored bands. Points on each plot represent partial residuals.

Table 3.5. Summary of mixed-effects linear regression model using day as a random effect and geofence intersection alert delay as the response.

Model term	**Estimate**	**SE**	**Lower CI**	**Upper CI**	***t*-value**	**DF**	***p*-value**
(Intercept)	11.9425	8.5931	−4.8998	28.7847	1.3898	Inf	1.6460×10^{-01}
TBA	0.4988	0.1463	0.2121	0.7855	3.4104	Inf	6.4876×10^{-04}
Concave[a]	13.5946	6.0494	1.7381	25.4512	2.2473	Inf	2.4622×10^{-02}
Aspect (E)	−19.0832	8.0855	−34.9306	−3.2359	−2.3602	Inf	1.8267×10^{-02}
Aspect (N)	−15.7249	9.4249	−34.1974	2.7475	−1.6684	Inf	9.5227×10^{-02}
Aspect (S)	−12.5487	9.5119	−31.1916	6.0942	−1.3193	Inf	1.8708×10^{-01}

[a] Variable indicating the presence of concave slopes.

3.5 Discussion

Analysis of missed radio signals indicated that forest stand characteristics, topography, and LOS obstructions affected the odds of missed signals. The odds of missed radio signals varied directly with stand density (TPH) and varied indirectly with LOS obstructions (*TVi*). Because previous work has shown that radio signal attenuation increases with greater vegetation depth and density, this result is somewhat counterintuitive [42–45]. However, the magnitude of these effects on the odds ratio was relatively small and may be a result of an interaction between stand density and vegetation in the LOS and/or external influences from wind or humidity [42,43,46–48]. Furthermore, topography influenced radio signal propagation, as convex slopes, aspect, and the presence of forest roads and streams affected the odds of missed signals. The mean number of missed signals during the observed 90-s interval was small, suggesting that relatively few position updates are missed at short distances (100 m).

Analysis of the PT RMSE indicated that only stand variables affected stationary GNSS accuracy. RMSE varied directly with Ht, but decreased with increasing QMD. Because characteristics associated with increasing forest stand density, such as canopy cover, are known to reduce GNSS accuracy, we expected that both predictors would have positive relationships with RMSE. Thus, this result is counterintuitive and may be an artefact of the data. A few sampled stands had relatively open canopies with large, mature trees at low density that may have affected the relationship between RMSE and QMD.

Both stand and topographic variables affected geofence intersection alert delay. Because of the way time delays were calculated, positive delays represent late alerts while negative delays represent early alerts. The alert delay varied directly with TBA and was higher in the presence of concave slopes. Aspect also affected alert delay, with delay being smaller on east slopes compared to west slopes. Taken together these results show that the time-to-signal accuracy of GNSS-RF geofence crossings is affected by both GNSS accuracy and radio signal propagation.

The relationships among the response and predictor variables were not strong for any of the three models. In the case of the missed radio signals, this could be due to the fact that the proportion of missed signals was generally low and the distance between radios fairly small (100 m). In terms of alert delay and RMSE, it is important to note that PTs receive coordinates from NAVSTAR GPS satellites only. Newer GNSS devices receive coordinates from multiple satellite constellations (i.e., from GPS, GLONASS, and BeiDou), which may improve accuracy and reliability in forested

environments [61,62]. We collected data for a single geofence crossing in each stand, and RMSE measurements were collected for 5 min at each location. It is possible that clearer relationships would be evident if RMSE was determined using data collected over a longer period of time. Furthermore, future work should perform similar experiments using GNSS-RF transponders capable of processing multiple satellite constellations, as this may yield stronger patterns.

Our results suggest that GNSS-RF radio signal propagation is related to stand density, topography, and obstructions in the line-of-sight and that geofence alert timing is related to stand characteristics and topography. This indicates that the accuracy and successful sharing of GNSS coordinates may change depending on stand conditions and topography, both of which vary on active timber sales. Thus, real-time positioning based on consumer-grade GNSS-RF units may improve general communication and situational awareness on logging operations by allowing ground workers and equipment operators to view the relative positions of nearby workers and machines in real-time on mobile devices. However, high-resolution, mission-critical safety applications of this technology (e.g., geofencing) are not yet advisable under mature forest conditions. Future work should focus on the development of correction methods that account for the effects of forest stand characteristics on GNSS accuracy and geofence alert delay. Previous work has shown that adjustments should also be made for the angle and speed at which a tracked object approaches a geofence [36,37]. Such correction methods may improve reliability and enable a broader range of uses of GNSS-RF technology for safety applications in natural resources, especially if combined with GNSS-RF transponders that communicate with multiple satellite systems. Moreover, phone-based GNSS positioning that incorporates inertial navigation system (INS) capabilities has the potential for improving positioning accuracy. When paired with emerging Bluetooth-based augmentation technologies to create ad-hoc networks, these mobile-based solutions may be promising alternatives to dedicated GNSS-RF units for real-time positioning in remote environments.

3.6 References

1. nasa.gov [Internet]. NASA; c2012–2015 [cited 2017 Jul 3]. Global positioning system history; [about 1 screen]. Available from: http://www.nasa.gov/directorates/heo/scan/communications/policy/GPS_History.html.
2. Wilkie DS. Performance of a backpack GPS in a tropical rain forest. Photogramm Eng Remote Sensing. 1989;55(12): 1747–1749.
3. Evans DL, Carraway RW, Simmons GT. Use of global positioning system (GPS) for forest plot location. South J Appl For. 1992;16(2): 67–70.

4. Bilodeau J, Gosselin S, Lowell K, Edwards G, Gold C. Operational integration of GPS into forest management activities which use a GIS to monitor forest operations. Proceedings of the GIS'93 Symposium; 1993 Feb 15–18; Vancouver, BC. p. 196–200.
5. Veal MW, Taylor SE, McDonald TP, McLemore DK, Dunn MR. Accuracy of tracking forest machines with GPS. Trans ASAE. 2001;44(6): 1903–1911. doi: 10.13031/2013.6978.
6. McDonald TP, Carter EA, Taylor SE. Using the global positioning system to map disturbance patterns of forest harvesting machinery. Can J For Res. 2002;32(2): 310–319. doi: 10.1139/X01-189.
7. McDonald TP, Fulton JP. Automated time study of skidders using global positioning system data. Comput Electron Agric. 2005;48(1): 19–37. doi: 10.1016/j.compag.2005.01.004.
8. Becker RM, Keefe RF, Anderson NM. Use of real-time GNSS-RF data to characterize the swing movements of forestry equipment. Forests. 2017;8(2): 44. doi: 10.3390/f8020044.
9. Devlin GJ, McDonnell K. Performance accuracy of real-time GPS asset tracking systems for timber haulage trucks travelling on both internal forest road and public road networks. Int J For Eng. 2009;20(1): 45–49. doi: 10.1080/14942119.2009.10702575.
10. Gallo R, Grigolato S, Cavalli R, Mazzetto F. GNSS-based operational monitoring devices for forest logging operation chains. J Agric Eng. 2013;44(2s): 140–144. doi: 10.4081/jae.2013.269.
11. Kaartinen H, Hyyppä J, Vastaranta M, Kukku A, Jaakkola A, Yu X, et al. Accuracy of kinematic positioning using global satellite navigation systems under forest canopies. Forests. 2015;6(9): 3218–3236. doi: 10.3390/f6093218.
12. Johnson CE, Barton CC. Where in the world are my field plots? Using GPS effectively in environmental field studies. Front Ecol Environ. 2004;2(9): 475–482. doi: 10.1890/1540-9295(2004)002[0475:WITWAM]2.0.CO;2.
13. Wing MG, Eklund A, Kellogg LD. Consumer-grade global positioning system (GPS) accuracy and reliability. J For. 2005;103(4): 169–173.
14. Karsky D. Comparing four methods of correcting GPS data: DGPS, WAAS, L-band, and postprocessing. Missoula (MT): U.S. Department of Agriculture, Forest Service, Missoula Technology and Development Center; 2004 Jul. Report No.: 0471-3-2307-MTDC.
15. D'Eon RG, Serrouya R, Smith G, Kochanny CO. GPS radiotelemetry error and bias in mountainous terrain. Wildl Soc Bull. 2002;30(2): 430–439.
16. D'Eon RG, Delparte D. Effects of radio-collar position and orientation on GPS radio-collar performance, and the implications of PDOP in data screening. J Appl Ecol. 2005;42(2): 383–388. doi: 10.1111/j.1365-2664.2005.01010.x.

17. Kos T, Markezic I, Pokrajcic J. Effects of multipath reception on GPS positioning performance. Proceedings of the ELMAR-2010 Symposium; 2010 Sep 15–17; Zadar, Croatia. IEEE; 2010.
18. Liu CJ, Brantigan R. Using differential GPS for forest traverse surveys. Can J For Res. 1995;25(11): 1795–1805. doi: 10.1139/x95-194.
19. Deckert C, Bolstad PV. Forest canopy, terrain, and distance effects on global positioning system point accuracy. Photogramm Eng Remote Sensing. 1996;62(3): 317–321.
20. Sigrist P, Coppin P, Hermy M. Impact of forest canopy on quality and accuracy of GPS measurements. Int J Remote Sens. 1999;20(18): 3595–3610. doi: 10.1080/014311699211228.
21. Holden NM, Martin AA, Owende PMO, Ward SM. A method for relating GPS performance to forest canopy. Int J For Eng. 2001;12(2): 51–56. doi: 10.1080/14942119.2001.10702446.
22. Lewis JS, Rachlow JL, Garton EO, Vierling LA. Effects of habitat on GPS collar performance: Using data screening to reduce location error. J Appl Ecol. 2007;44(3): 663–671. doi: 10.1111/j.1365-2664.2007.01286.x.
23. Wempe AM, Keefe RF. Characterizing rigging crew proximity to hazards on cable logging operations using GNSS-RF: Effect of GNSS positioning error on worker safety status. Forests. 2017;8(10): 357. doi: 10.3390/f8100357.
24. Liu J, Hyyppä J, Yu X, Jaakkola A, Liang X, Kaartinen H, et al. Can global navigation satellite system signals reveal the ecological attributes of forests? Int J Appl Earth Obs Geoinf. 2016;50: 74–79. doi: 10.1016/j.jag.2016.03.007.
25. Liu J, Hyyppä J, Yu X, Jaakkola A, Kukko A, Kaartinen H, et al. A novel GNSS technique for predicting boreal forest attributes at low cost. IEEE Trans Geosci Remote Sens. 2017;55(9): 4855–4867. doi: 10.1109/TGRS.2017.2650944.
26. Bolstad P, Jenks A, Berkin J, Horne K, Reading WH. A comparison of autonomous, WAAS, real-time, and post-processed global positioning systems (GPS) accuracies in northern forests. North J Appl For. 2005;22(1): 5–11.
27. Piedallu C, Gégout J-C. Effects of forest environment and survey protocol on GPS accuracy. Photogramm Eng Remote Sensing. 2005;71(9): 1071–1078. doi: 10.14358/PERS.71.9.1071.
28. Wing MG, Eklund A. Performance comparison of a low-cost mapping grade global positioning systems (GPS) receiver and consumer grade GPS receiver under dense forest canopy. J For. 2007;105(1): 9–14.
29. Danskin SD, Bettinger P, Jordan TR, Cieszewski C. A comparison of GPS performance in a southern hardwood forest: Exploring low-cost solutions for forestry applications. South J Appl For. 2009;33(1): 9–16.

30. Bettinger P, Fei S. One year's experience with a recreation-grade GPS receiver. Math Comput For Nat Resource Sci. 2010;2(2): 153–160.
31. Danskin S, Bettinger P, Jordan T. Multipath mitigation under forest canopies: A choke ring antenna solution. For Sci. 2009;55(2): 109–116.
32. Wing MG. Consumer-grade global positioning systems (GPS) receiver performance. J For. 2008;106(4): 185–190.
33. Andersen HE, Clarkin T, Winterberger K, Strunk J. An accuracy assessment of positions obtained using survey- and recreational-grade global positioning system receivers across a range of forest conditions within the Tanana Valley of interior Alaska. West J Appl For. 2009; 24(3): 128–136.
34. Wing MG. Consumer-grade GPS receiver measurement accuracy in varying forest conditions. Res J For. 2011;5(2): 78–88. doi: 10.3923/rjf.2011.78.88.
35. Keefe RF, Eitel JUH, Smith AMS, Tinkham WT. Applications of multi transmitter GPS-VHF in forest operations. Proceedings of the 47th International Symposium on Forestry Mechanization and 5th International Forest Engineering Conference; 2014 Sep 23–26; Gerardmer, France.
36. Grayson LM, Keefe RF, Tinkham WT, Eitel JUH, Saralecos JD, Smith AMS, et al. Accuracy of WAAS-enabled GPS-RF warning signals when crossing a terrestrial geofence. Sensors. 2016;16(6): 912. doi: 10.3390/s16060912.
37. Zimbelman EG, Keefe RF, Strand EK, Kolden CA, Wempe AM. Hazards in motion: Development of mobile geofences for use in logging safety. Sensors. 2017;17(4): 822. doi: 10.3390/s17040822.
38. Sygnatur EF. Logging is perilous work. Compens Work Cond. 1998;3: 3–9.
39. U.S. Bureau of Labor Statistics, Current Population Survey, Census of Fatal Occupational Injuries, 2016. Available from: http://www.bls.gov/iif/oshcfoi1.htm.
40. Tamir T. Radio wave propagation along mixed paths in forest environments. IEEE Trans Antennas Propag. 1977;25(4): 471–477. doi: 10.1109/TAP.1977.1141620.
41. Seker SS. Radio pulse transmission along mixed paths in a stratified forest. IEE Proceedings H (Microwaves, Antennas and Propagation). 1989;136(1): 13–18. doi: 10.1049/ip-h-2.1989.0002.
42. Savage N, Ndzi D, Seville A, Vilar E, Austin J. Radio wave propagation through vegetation: Factors influencing signal attenuation. Radio Sci. 2003;38(5): 1088. doi: 10.1029/2002RS002758.
43. Tewari RK, Swarup S, Roy MN. Radio wave propagation through rain forests of India. IEEE Trans Antennas Propag. 1990;38(4): 433–449. doi: 10.1109/8.52261.

44. Al-Nuaimi MO, Stephens RBL. Measurements and prediction model optimisation for signal attenuation in vegetation media at centimetre wave frequencies. IEE Proceedings – Microwaves, Antennas and Propagation. 1998;145(3): 201–206. doi: 10.1049/ip-map:19981883.
45. Azevedo JAR, Santos FES. An empirical propagation model for forest environments at tree trunk level. IEEE Trans Antennas Propag. 2011;59(6): 2357–2367. doi: 10.1109/TAP.2011.2143664.
46. Meng YS, Lee YH, Ng BC. The effects of tropical weather on radio-wave propagation over foliage channel. IEEE Transactions on Vehicular Technology. 2009;58(8): 4023–4030. doi: 10.1109/TVT.2009.2021480.
47. Löw K. UHF measurements of seasonal field-strength variations in forests. IEEE Transactions on Vehicular Technology. 1988;37(3): 121–124. doi: 10.1109/25.16537.
48. Meng YS, Lee YH, Ng BC. Study of propagation loss prediction in forest environment. Prog Electromagn Res B Pier B. 2009;17: 117–133. doi: 10.2528/PIERB09071901.
49. Kürner T, Cichon DJ, Wiesbeck W. Concepts and results for 3D digital terrain-based wave propagation models: An overview. IEEE Journal on Selected Areas in Communications. 1993;11(7): 1002–1012. doi: 10.1109/49.233213.
50. Freeland RS, Buschermohle MJ, Nichols WM. Precision agriculture: RTK base-to-tractor range limitations using RF communication. Appl Eng Agric. 2014;30(1): 97–104. doi: 10.13031/aea.30.10072.
51. Raveon Support [Internet]. Raveon Technologies; [cited 2017 Jul 14]. Available from: http://www.raveon.com/support/.
52. The National Map Download [Internet]. United States Geological Survey (USGS); [cited 2017 Jul 14]. Available from: https://viewer.nationalmap.gov/basic/.
53. NIST Internet Time Servers [Internet]. National Institute of Standards and Technology; [cited 2017 Jul 14]. Available from: http://tf.nist.gov/tf-cgi/servers.cgi.
54. Arrow 100 Subfoot GNSS [Internet]. Eos Positioning Systems; c2014–2017 [cited 2017 Jul 14]. Available from: http://www.eos-gnss.com/arrow-100/.
55. R Core Team. R: A language and environment for statistical computing. R Foundation for Statistical Computing, Vienna, Austria, 2016. Available from: https://www.R-project.org/.
56. Lutes DC, Keane RE, Caratti JF, Key CH, Benson NC, Sutherland S, et al. FIREMON: Fire effects monitoring and inventory system. Fort Collins (CO): U.S. Department of Agriculture, Forest Service, Rocky Mountain Research Station; 2006 Jun. Report No.: RMRS-GTR-164-CD.

57. GNSS Planning Online [Internet]. Trimble; [cited 2017 Jul 5]. Available from: http://www.trimble.com/GNSSPlanningOnline/#/Settings.
58. Bates D, Maechler M, Bolker B, Walker S. Fitting linear mixed-effects models using lme4. J Stat Softw. 2015;67(1): 1–48. doi: 10.18637/jss.v067.i01.
59. Mazerolle MJ. AICcmodavg: Model selection and multimodel inference based on (Q)AIC(c). 2016. R package version 2.1-0. Available from: https://cran.r-project.org/package=AICcmodavg.
60. Johnson T. trtools: Miscellaneous tools for teaching statistics. 2017. R package version 0.1.0. Available from: http://github.com/trobinj/trtools.
61. Næsset E, Bjerke T, Øvstedal O, Ryan LH. Contributions of differential GPS and GLONASS observations to point accuracy under forest canopies. Photogramm Eng Remote Sensing. 2000;66(4): 403–407.
62. Li X, Zhang X, Ren X, Fritsche M, Wickert J, Schuh H. Precise positioning with current multi-constellation global navigation satellite systems: GPS, GLONASS, Galileo and BeiDou. Sci Rep. 2015;5: 1–14. doi: 10.1038/srep08328.

Chapter 4: Lost in the Woods: Forest Vegetation, and not Topography, Most Affects the Connectivity of Mesh Radio Networks for Public Safety

Submitted To:

Zimbelman EG, Keefe RF. Lost in the woods: Forest vegetation, and not topography, most affects the connectivity of mesh radio networks for public safety. Saf Sci. 2022 (Submitted).

4.1 Abstract

Real-time data- and location-sharing using mesh networking radios paired with smartphones may improve situational awareness and safety in remote environments lacking communications infrastructure. Despite being increasingly used for wildland fire and public safety applications, there has been little formal evaluation of the network connectivity of these devices. The objectives of this study were to 1) characterize the connectivity of mesh networks in variable forest and topographic conditions; 2) evaluate the abilities of lidar and satellite remote sensing data to predict connectivity; and 3) assess the relative importance of the predictive metrics. A large field experiment was conducted to test the connectivity of a network of one mobile and five stationary goTenna Pro mesh radios on 24 Public Land Survey System sections in northern Idaho. Dirichlet regression was used to predict connectivity using 1) both lidar- and satellite-derived metrics (LIDSAT); 2) lidar-derived metrics only (LID); and 3) satellite-derived metrics only (SAT). On average the full network was connected only 32.6% of the time and the mobile goTenna was disconnected from all other devices 18.2% of the time. RMSE for the six connectivity levels ranged from 0.101 to 0.314 for the LIDSAT model, from 0.103 to 0.310 for the LID model, and from 0.121 to 0.313 for the SAT model. Vegetation-related metrics affected connectivity more than topography. Developed models may be used to predict the expected performance of real-time mesh networks to support wildland firefighting, forestry, and public safety. However, safety professionals should be aware of the impacts of vegetation on connectivity.

4.2 Introduction

Use of new mesh radio devices that pair with smartphones using Bluetooth can facilitate global navigation satellite system - radio frequency (GNSS-RF) sharing of locations among people and equipment in remote environments. This type of technology has potential applications in public safety when communications infrastructure is absent by enabling communication of location-aware geospatial information among wildland firefighters, search and rescue (SAR), and other emergency

personnel to improve situational awareness (SA) (CoE 2018a, 2018b, 2019; Keefe et al. 2019a). This technology may be useful for disaster communications in healthcare (Goldberg et al. 2021) and for digital safety applications in forestry (Wempe et al. 2019). Wildland firefighting is a particularly strenuous and hazardous occupation, with 480 fatalities between 1990 and 2016 (Risk Management Committee 2017). Vehicle- and aviation-related incidents, medical events, such as strokes and heart attacks, and fire entrapments were among the leading causes of wildland firefighter fatalities from 2001 to 2012 (Butler et al. 2017) as well as between 2007 and 2016 (Risk Management Committee 2017). To address this, efforts have been made to increase safety and reduce injuries and fatalities among wildland firefighters (Risk Management Committee 2017). Section 1114 of the John D. Dingell, Jr. Conservation, Management, and Recreation Act signed into law in 2019 required implementation of a system to monitor the locations of all active wildland fire resources used by Federal Type 1 incident management teams in the United States (Murkowski 2019). As part of the enacted legislation, interagency Dingell Act Resource Tracking (DART) teams were required to conduct pilot projects to evaluate available resource tracking technologies that could be used on type I incidents (U.S. Department of Agriculture 2020; DART Team 2021). One tracking system evaluated by the DART Team was the Team Awareness Kit (TAK) smartphone app paired with goTenna Pro X mesh networking radios (goTenna Inc, Brooklyn, NY, USA), which allow communication in areas lacking cellular service (DART Team 2021). goTenna Pro mesh radios pair with smartphones using Bluetooth and enable automatic sharing of GNSS coordinates, text messages, points, and shapes within the TAK app via radio frequency (DART Team 2021). Previous evaluations of these devices have reported on their general performance and potential for increasing SA (CoE 2018a, 2018b, 2019; Keefe et al. 2019a; Wempe et al. 2019) and their ability to transmit to a stationary repeater (DART Team 2021). However, there has not been a comprehensive, replicated study evaluating the connectivity of networks of goTenna Pro mesh radio devices operating in a range of forest vegetation and terrain types in the Northern Rocky Mountain region.

In addition to improved SA in wildland firefighting, GNSS-RF positioning, geofencing, mesh networking, and human activity recognition have a range of other possible applications in natural resource safety and management (Keefe et al. 2019a). For example, by monitoring the current safety status and location of individuals relative to workplace hazards, real-time positioning has been evaluated as a tool for improving SA and safety on logging operations (Wempe and Keefe 2017; Zimbelman et al. 2017; Newman et al. 2018; Zimbelman and Keefe 2018; Wempe et al. 2019). Additionally, human activity recognition using wearable and mobile device sensors can be used to quantify occupational tasks in forestry (Keefe et al. 2019b; Zimbelman and Keefe 2021), which could

ultimately improve health and safety as well as precision forestry and fire management. The use of these technologies, together with the increasing availability of remote sensing and big data in forestry, represent aspects of smart forestry and Forestry 4.0 (Gingras and Charette 2017; Müller et al. 2019; Zou et al. 2019; Feng and Audy 2020; Keefe et al. 2022). Forestry 4.0 is based on the adoption of Industry 4.0 concepts in forestry, such as the digitalization, automation, and increase in precision in the forestry supply chain (Gingras and Charette 2017; Müller et al. 2019; Feng and Audy 2020). Recent advances in GNSS-RF mesh and mobile ad hoc networks (MANETs) have made it possible to share the locations obtained from the GNSS chip in phones with other paired phones and devices. Depending on the particular technology, users may share locations, send texts, and even make voice calls in the absence of cellular networks or base stations (Wu et al. 2000; Marina and Das 2001; Tseng et al. 2002). Furthermore, many of these technologies also form mesh, or multi-hop, networks, in which each node in the network can relay data to other nodes (Marina and Das 2001; Tseng et al. 2002). Unlike traditional radios, mesh networking allows information to be routed through other nodes to enable communication between users who may not have a direct line-of-sight (LOS) connection (Tseng et al. 2002).

A mesh network is considered connected if a path exists between each pair of nodes (Wang et al. 2010). One way to evaluate mesh networks is to calculate the connectivity probability, which is the proportion of time the network is connected over a specified observation period (Wang et al. 2010). Traditional approaches to studying landscape-scale connectivity of radio networks have relied heavily on computer-intensive methods that simulate routing protocols (Hong et al. 1999; Royer and Toh 1999; Marina and Das 2001; Pathak and Dutta 2011), mobility models (Hong et al. 1999; Jardosh et al. 2003; Aschenbruck et al. 2009; Wang et al. 2010, 2019; Papageorgiou et al. 2012; Schwamborn and Aschenbruck 2013), and radio signal propagation models (Stepanov and Rothermel 2008; Kamarudin et al. 2010; Galvan-Tejada and Duarte-Reynoso 2012). Radio propagation models can be either theoretical or empirical, and many are derived using both analytical and empirical methods (Rappaport 2002; Alsayyari et al. 2014). Because they are based on actual measurements, empirical models can account for all the known or unknown environment-related factors that affect radio wave propagation, but they may not be valid in different environments or at different transmission frequencies (Rappaport 2002). There is also a tradeoff in computational complexity between empirical models and more realistic models that account for geography, terrain, or vegetation (Stepanov and Rothermel 2008).

Early research on near-ground communication and radio transmission in forested environments demonstrated the ability of empirical radio propagation models that account for foliage to predict measured VHF and UHF path loss in vegetation (Joshi et al. 2005; Meng et al. 2010). More recently, wireless sensor networks (WSNs), which rely on near-ground peer-to-peer propagation and share similar features with MANETs used for public safety, have been evaluated for environmental monitoring and communication in remote vegetated environments (Gay-Fernández et al. 2010; Kamarudin et al. 2010; Gay-Fernández and Cuiñas 2013; Anastassiu et al. 2014; Smith et al. 2016). Olasupo and Otero proposed a variety of path loss models based on WSN nodes deployed in jungle environments and compared these to theoretical models, most of which were found to under-predict path loss (Olasupo and Otero 2020). To move beyond empirical predictions that used only distance and frequency to estimate path loss, Azevedo and Santos developed empirical models that accounted for forest stand parameters including tree density, tree diameter, canopy diameter, and foliage density (Azevedo and Santos 2011, 2017). Anastassiu et al. developed computational models based on tree geometry and the electrical characteristics of air, soil, and vegetation (Anastassiu et al. 2014).

Kotz et al. noted that most simulations evaluating wireless networks assume propagation along a flat plane and use outdoor experiments to show that future research should account for radio propagation in 3D terrain (Kotz et al. 2004). To incorporate the effects of terrain when simulating static ad hoc networks, Durkin's propagation model (Edwards and Durkin 1969) has been used with digital elevation models (DEMs) or triangulated irregular networks (TINs) to show that terrain can decrease the number of links between nodes (Filiposka et al. 2013) and change network connectivity (Nguyen et al. 2016). Simulations using mobile nodes together with Durkin's model and DEMs have shown that incorporating terrain results in more realistic estimates of network performance, demonstrating that terrain can both degrade and improve performance (Filiposka and Trajanov 2011) and that some performance metrics may decrease with increasing moving speed (Lin et al. 2013). Loo et al. used a 3D terrain model based on DEMs to estimate path loss and found that the terrain profile between nodes was an important predictor (Loo et al. 2017). DEMs have also been used to develop methods that optimize the placement of WSNs for wildfire monitoring (Teguh et al. 2014).

As is evident in prior literature, the majority of past research has emphasized use of simulation modeling methods that require assumptions about network propagation and routing protocols. An alternative approach to studying the connectivity of mesh networks in complex, forested landscapes that has received comparatively little attention is the use of remote sensing to characterize and map connectivity. Al-Turjman et al. mention using lidar to characterize trees and

forests in order to determine potential node positions for optimal network deployment (Al-Turjman et al. 2009). To link remote sensing data to measured radio frequency path loss, Jiang et al. used the Normalized Difference Vegetation Index (NDVI) derived from Landsat 8 satellite imagery to predict the path loss exponent (Jiang et al. 2014). Demetri et al. expanded on the model presented by Azevedo and Santos (Azevedo and Santos 2011) to propose a method for predicting signal attenuation using lidar, and validated predictions using WSN deployments in forests (Demetri et al. 2015). This model was subsequently used to develop an automated approach to identifying optimal node placement in forested environments (Demetri et al. 2019). Oroza et al. developed a machine learning program that uses lidar data to identify potential locations for snow sensors (Oroza et al. 2016). Additionally, RSSI measurements from the American River Hydrologic Observatory were used to train a path loss model using machine learning (Oroza et al. 2017). A variety of independent variables were used in the model, including path ground distance, canopy coverage, terrain complexity, and path angle, many of which were extracted from DEMs or the National Land Cover Database (Oroza et al. 2017). Prediction error was lower using machine learning when compared to traditional empirical path loss model approaches (Oroza et al. 2017).

The effects of terrain and vegetation on mesh network connectivity have been evaluated independently, but the potential interactions and relative importance of the two have not been quantified. In this study, we developed a method to predict mesh network connectivity using remote sensing data without relying on traditional network simulators. We performed a large field experiment to test the connectivity of a network of goTenna Pro devices paired with Google Pixel smartphones. Dirichlet regression was used to predict connectivity using terrain and vegetation metrics as predictors. The metrics were derived from lidar data, satellite imagery, and a combination of the two. Our first research objective was to characterize the connectivity of mesh networks in variable forest and topographic conditions in the northern Rocky Mountain region of the United States. Our second objective was to evaluate the abilities of lidar and satellite remote sensing data to predict connectivity, as evident in useful predictive regression relationships. We hypothesized that using both lidar- and satellite-derived metrics would improve model predictions. Our third objective was to assess the relative importance of the different predictive metrics. In doing so, we hypothesized that terrain-related metrics would be more important than the vegetation metrics for predicting connectivity, as indicated by how frequently these two types of variables were selected for inclusion in final models. This work will inform use of goTenna Pro and other ad hoc mesh radio networks for resource monitoring in wildland firefighting, forestry and public safety and allow others to predict the connectivity of these networks using publicly available remote sensing data.

4.3 Materials and Methods

4.3.1 Field study

In order to evaluate the terrain and vegetation factors affecting the connectivity of VHF-based mesh networks, a designed field experiment was conducted on 24 sections delineated by the Public Land Survey System (PLSS). Sections are approximately one square mile in size and were selected from within the boundary of the Clearwater–Nez Perce 3DEP 2016 lidar acquisition covering 2,662 square miles in northwestern Idaho and southeastern Washington (Idaho Lidar Consortium). In an effort to categorize airborne lidar datasets, the National Enhanced Elevation Assessment (NEEA) defined five elevation data Quality Levels (QLs) characterized by horizontal resolution and vertical accuracy (Dewberry 2012). The United States Geological Survey (USGS) National Geospatial Program (NGP) established the 3D Elevation Program (3DEP) based on the NEEA recommendations (Heidemann 2018). Of the five quality levels, Quality Level 1 (QL1) and Quality Level 2 (QL2) are considered acceptable for 3DEP and the standard national DEM available through The National Map (Heidemann 2018). QL1 data has an aggregate nominal pulse spacing of ≤ 0.35 m and aggregate nominal pulse density of ≥ 8.0 pls/m^2 (Heidemann 2018). QL2 data has an aggregate nominal pulse spacing of ≤ 0.71 m and aggregate nominal pulse density of ≥ 2.0 pls/m^2 (Heidemann 2018). Both QL1 and QL2 have vertical accuracies ($RMSE_z$) of ≤ 10 cm (Heidemann 2018). Both QL1 and QL2 lidar was flown for the Clearwater–Nez Perce acquisition between October 29, 2016, and November 13, 2016, with the QL1 data covering 847 square miles and the QL2 data covering 1,815 square miles. This study was confined to the area covered only by QL1 data (Figure 4.1). The QL1 data was flown at an altitude of 1,900 m with a 60° field of view. The resulting area had an average point density of 9.5 pts/m^2 and average point spacing of 0.35 m. Quantum Spatial (St. Petersburg, FL, USA) processed the QL1 data into a 0.5-m hydro-flattened bare earth raster DEM. All lidar data was downloaded using the Globus Web App (University of Chicago 2022).

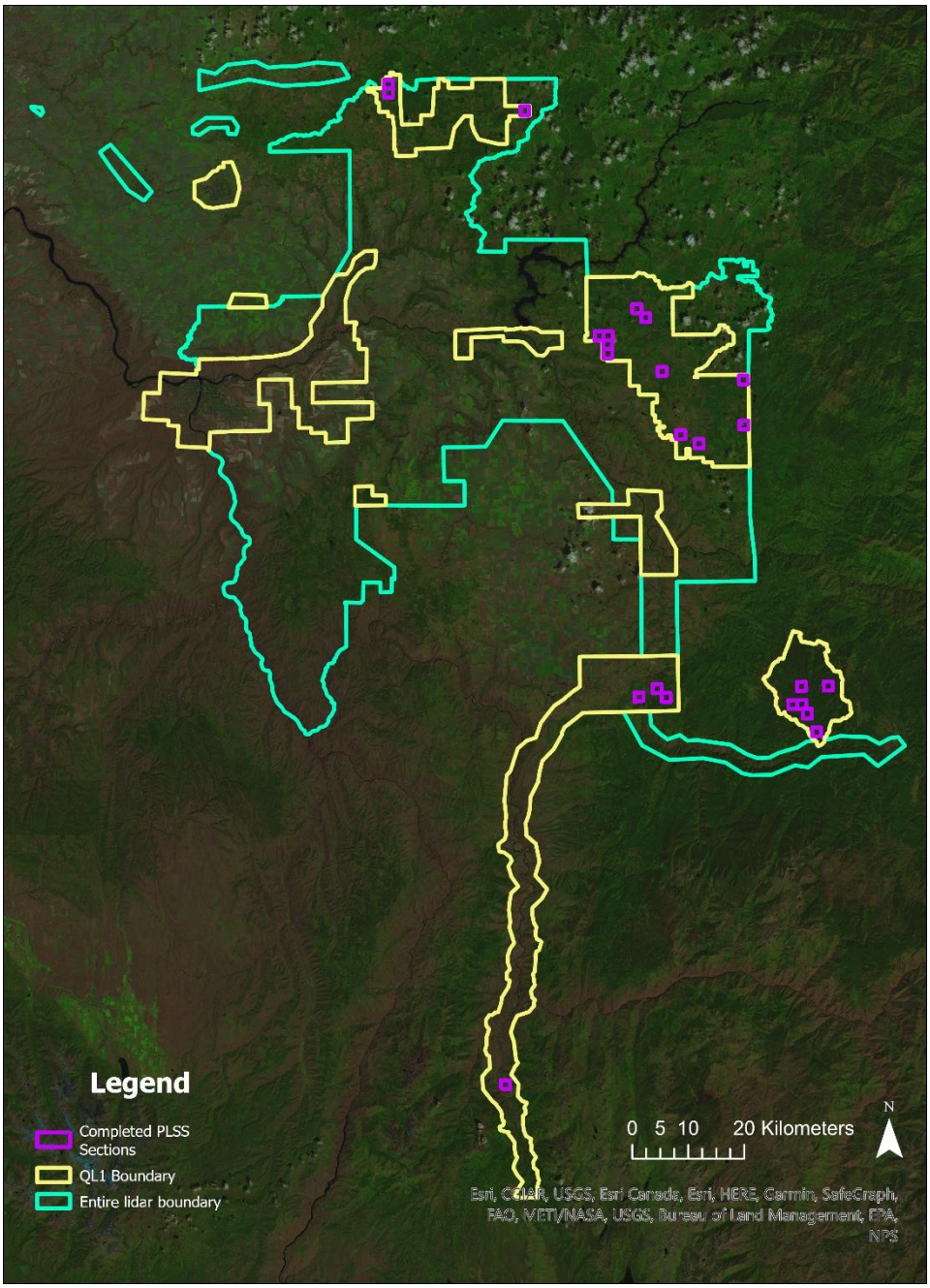

Figure 4.1. Map of the area covered by the entire Clearwater–Nez Perce 3DEP 2016 lidar acquisition, highlighting the QL1 data boundaries and the 24 randomly-selected PLSS sections.

In order to capture variability in terrain, sections were selected based on the rumple index, which can be used to characterize ground roughness (Blanchette et al. 2015). The 0.5-m DEMs were used to calculate the rumple index using the rumple_index function from the lidR package (Roussel

and Auty 2021) in the R statistical programming environment (R Core Team 2021). This function calculates the ratio between a surface's area and its projected area on the ground. A rumple index was calculated for each section covered completely by the QL1-derived 0.5-m DEMs. Rumple indices for sections covered by the entire QL1 dataset ranged from 1.005996 – 1.291691, although sections with rumple indices > 1.19 were excluded due to limited accessibility. Sections were visually inspected in Google Earth, and sections that 1) appeared to be less than 25% forested; 2) had major river crossings; or 3) included any urban areas were removed from consideration. While PLSS sections are supposed to be one square mile (260 hectares [ha]) in area, the actual areas vary and only sections that were within 10% (26 ha) of this were included. After filtering sections by these criteria, the number of eligible sections was reduced from 626 to 286, with rumple indices ranging from 1.005997 – 1.188209. This reduced range was divided into five categories (1.005997 – 1.042439; 1.042439 – 1.078882; 1.078882 – 1.115324; 1.115324 – 1.151767; 1.151767 – 1.188209) and five sections from each category were randomly selected (Figure 4.1). Sections were located on a mix of public and private land, and only sections where landowner permission was granted were utilized. Only seven of the 286 eligible sections fell into the highest rumple category (1.151767 – 1.188209). Two of these were located on private land, and landowner permission was not granted. A third section was inaccessible due to hunting restrictions, weather, and its remote location. This resulted in only four eligible sections in the highest rumple category and meant a total of 24 sections were used in the study.

Field data was collected between June 14, 2019, and November 1, 2019. Within each section, five goTenna Pro units paired with Google Pixel smartphones were placed in randomly-selected locations. In order to ensure goTennas were not too close together, the distance between all goTenna locations within each section was calculated prior to sampling and new locations were randomly selected whenever the distance between devices was less than 75 m. goTenna Pros operate on tunable VHF frequencies between 142 – 175 MHz, with options to configure both control and data channels. For this study, the Pros were set up with two control channels (151.7000 MHz and 151.7600 MHZ) and one data channel (151.5125 MHZ) licensed to our lab group. Power output was set to 5 W and the bandwidth was 11.8 kHz. When paired with a smartphone, users can send text messages and share locations (acquired from the smartphone's GNSS chip) through the goTenna. All Pro/Pixel pairs were mounted 1 m above the ground on wooden stakes and were set to transmit their coordinates to each other every 30 seconds. Data was recorded using the Android Team Awareness Kit – Civil Use (ATAK-CIV) app, version 3.8.1 (TAK Product Center 2018) and the goTenna ATAK-CIV Plugin. Because of the way in which ATAK-CIV records location data, it is impossible to detect missed

locations unless you know the tracked unit is moving and expect a change in coordinates every 30 s. Thus, a sixth goTenna Pro paired with a Pixel was carried on a belt by a volunteer who traversed each section once diagonally. The path began at a randomly-selected corner of the section and the volunteer walked for at least one hour. Due to the variable nature of the terrain and vegetation, the time it took to traverse each section varied. As a result, the number of total transmissions in each section ranged from 129 to 327. The true coordinates of this mobile unit were considered to be the coordinates recorded locally and were used to determine whether each new location was successfully transmitted to the five stationary Pros. Thus, for each section we calculated the proportion of the total transmitted locations that were received by each of the stationary Pros. Additionally, there were occasional instances when the mobile goTenna did not record a change of coordinates for 30 s or longer, such as when GNSS signal quality was poor or when the volunteer stopped moving for a brief period. This would then be detected as an incorrect missed signal when looking at the data recorded by the stationary units. To avoid this, the dataset was visually inspected to ensure that all missed signals were due to missed transmissions, and not due to a lack of change of coordinates from the mobile unit. Finally, one of the stationary goTenna Pros turned off for an unknown reason during data collection in one PLSS section. This occurred when the volunteer carrying the mobile goTenna was more than halfway through traversing the section and as a result, connectivity data was calculated only up until the point at which the stationary goTenna turned off.

4.3.2 Remote sensing data processing

4.3.2.1 Lidar metrics

In order to predict connectivity, a variety of metrics were derived from the QL1 lidar data as well as from Landsat 8 satellite imagery in order to represent the potential effects of terrain, vegetation, and canopy cover. All lidar data was processed in R, version 4.1.2 (R Core Team 2021) and a variety of metrics based on the DEMs, canopy height models (CHMs), point cloud, and voxels were calculated. To characterize terrain roughness, the 0.5-m DEMs were used to calculate the rumple index for each section as described above, the surface relief ratio (SRR), as well as the mean and standard deviation of slope, topographic position index (TPI), roughness, flow direction, hierarchical slope position (HSP), McNab's curvature, terrain ruggedness index (TRI), heat load index (HLI), and dissection (Table A.1 in Appendix A). Vegetation height was calculated by normalizing the z-values of the lidar point cloud using the normalize_height function in the R lidR package (Roussel and Auty 2021) together with the 0.5-m DEMs. The normalized point cloud was cropped for each section and used to calculate a variety of metrics to characterize vegetation and canopy cover. First, the point cloud was visualized for each section, and any remaining obvious

outliers were removed manually. The normalized point cloud was then used to create a 0.5 m pit-free CHM using the lidR grid_canopy function, using only first vegetation returns ≥ 0.27 m in height. The lidR rumple_index function was then used with the resulting CHM to calculate a rumple index for the canopy, in order to characterize the irregularity and topography of the canopy surface (Parker et al. 2004; Blanchette et al. 2015). The percentage of returns classified as "ground" was also calculated using the lidR cloud_metrics function using all vegetation returns ≥ 0.27 m and the lidR LAD function was used to calculate leaf area density using 1 m height bins up to 30.5 m using all, first, and last vegetation returns ≥ 0.27 m (Table A.1 in Appendix A). Finally, custom functions (Blackburn 2021) developed by Blackburn et al. (Blackburn et al. 2021) were used to calculate a variety of cloud- and voxel-based metrics (Table A.1 in Appendix A). Both the point cloud, or area-based, and voxel-based variables summarized aspects of point density, height, and intensity across each section. Voxels, or volumetric pixels, are created by dividing the lidar point cloud along the horizontal and vertical axes, and voxel-based metrics are then calculated by summarizing the points encompassed by each voxel (Pearse et al. 2019). The Blackburn std_cloud function (Blackburn 2021) was used within the lidR cloud_metrics function to calculate a variety of cloud-based metrics using all, first, and last vegetation returns ≥ 0.27 m (Table A.1 in Appendix A). The Blackburn std_voxel and vox_mt functions (Blackburn 2021) were modified slightly and used within the lidR cloud_metrics function to calculate a variety of voxel-based metrics at 3 m, 4 m, and 5 m resolutions using all vegetation returns ≥ 0.27 m (Table A.1 in Appendix A). Specifically, the original skewness and kurtosis calculations within both the std_voxel and vox_mt functions were replaced with the skewness and kurtosis functions in the R moments package (Komsta and Novomestky 2015) and the height thresholds and height bins used to calculate canopy closure (cc_abovez_res) and mean percentage canopy closure (p_cc_res) were modified for each resolution (Table A.1 in Appendix A). In total, 919 lidar metrics were calculated. These lidar DEM-, point cloud-, and voxel-derived metrics were included because they have been shown to be correlated with forest structural parameters (Gobakken and Næsset 2008; Popescu and Zhao 2008; Woods et al. 2008; Falkowski et al. 2010; Latifi et al. 2010; van Ewijk et al. 2011; González-Ferreiro et al. 2012; Hudak et al. 2012, 2016; Hyyppä et al. 2012; Lu et al. 2012; Pope and Treitz 2013; Blanchette et al. 2015; Ehbrecht et al. 2016; Kim et al. 2016; Pearse et al. 2017, 2019; Phua et al. 2017; Tenneson et al. 2018; Blackburn et al. 2021).

4.3.2.2 Landsat 8 satellite metrics

Landsat 8 Operational Land Imager (OLI) Collection 2 Tier 1 Level-2 Science Product (L2SP) scenes covering the 24 sections were downloaded from USGS EarthExplorer (U.S. Geological Survey 2022) using an acquisition date range from June 1, 2019 to November 1, 2019 and

cloud cover for the entire scene from 0% to 20%. Landsat data was processed in R. Eligible scenes for each section were cropped using the section boundary, and these resulting images were then used to ensure that less than 5% of the imagery for each section was "not clear" (using the Pixel QA bands) and that less than 5% of the section was classified as high or medium aerosols (using the Aerosol QA bands). After selecting for these criteria, the scene acquired closest in time to the sampling date for each section was ultimately chosen to be used to calculate a variety of metrics for each section. L2SP surface reflectance scenes for bands 1–7 were rescaled using multiplicative and additive band-specific scale factors (U.S. Geological Survey 2020) in order to calculate percentage reflectance values. These scenes were then masked using the Pixel QA and Aerosol QA bands to remove pixels that were not clear or were classified as high or medium aerosols. Basic surface reflectance metrics (mean and standard deviation) for each section were calculated for bands 1–7 of the resulting masked scenes (Table 4.1). Mean and standard deviation of NDVI were also calculated for each section using the masked scenes (Table 4.1). NDVI was calculated using Eq (1):

$$NDVI = \frac{(NIR - Red)}{(NIR + Red)} \quad (1)$$

Where *Red* is the red band (Landsat 8 OLI band 4) reflectance and *NIR* is the near-infrared band (Landsat 8 OLI band 5) reflectance.

Finally, grey-level co-occurrence matrix (GLCM) texture metrics were calculated for each section using the glcm function in the R glcm package (Zvoleff 2020) and the masked Landsat scenes. Specifically, the mean and standard deviation of eight texture measures (mean, variance, homogeneity, contrast, dissimilarity, entropy, second moment, and correlation) were calculated for bands 1–7 using four window sizes (3, 5, 7, and 9) and 64 grey levels (Table 4.1). A total of 464 satellite metrics were calculated. These satellite-derived metrics were included because they have been shown to be correlated with forest structural parameters (Pocewicz et al. 2004; Hudak et al. 2006; Kayitakire et al. 2006; Gasparri et al. 2010; Gonzalez et al. 2010; Latifi et al. 2010; Gómez et al. 2012; Lu et al. 2012; Kelsey and Neff 2014; Dube and Mutanga 2015; Phua et al. 2017).

Table 4.1. Satellite-derived metrics.

Variable	**Description**
SR_stat_B	Surface reflectance statistics (stat = mean and standard deviation) for each band (B = 1–7), calculated for each section
NDVI_stat	NDVI statistics (stat = mean and standard deviation) calculated for each section
GLCM_stat_B_win	Eight GLCM texture metrics (GLCM = mean, variance, homogeneity, contrast, dissimilarity, entropy, second moment, and correlation) were calculated for each section using four window sizes (win = 3, 5, 7, 9) for each band (B = 1–7), then two statistics (stat = mean and standard deviation) were calculated for each metric

4.3.3 Model development

4.3.3.1 Connectivity

Connectivity was calculated as the proportion of the total number of transmitted signals sent from the mobile goTenna that were received by five, four, three, two, one, or zero stationary goTennas (Table 4.2, Figure 4.2). Specifically, the proportion of total signals received by all five stationary goTennas (Con_6) represented the proportion of time the full network of six devices (i.e., the five stationary goTennas and one mobile goTenna) was connected. The proportion of total signals received by zero stationary goTennas (Con_1) represented the proportion of time none of the stationary goTennas were connected to the mobile goTenna. This resulted in a compositional dataset, where the dependent variables for each section were the proportions of the six connectivity levels, which summed to one. A common problem in compositional data analysis occurs when the dataset contains zero values, since both traditional log-ratio analysis and Dirichlet regression cannot handle zero values in any of the compositional responses. Zeros can be considered to be rounded, essential, or count zeros (Martín-Fernández et al. 2003, 2015). Rounded zeros can occur when a component is present but below a detection limit, and it is often suitable to replace rounded zeros by a small value (Martín-Fernández et al. 2003). Essential zeros represent the true absence of that portion of the composition, and it is generally not appropriate to replace these zeros (Martín-Fernández et al. 2003). Instead, various approaches such as combining categories, have been suggested (Martín-Fernández et al. 2003). Count zeros are considered to represent values that may have been observed if a different sampling design or larger number of trials had been utilized (Martín-Fernández et al. 2015). Zero values in our dataset were considered to be count zeros and were replaced using the cmultRepl function in the R zCompositions package (Palarea-Albaladejo and Martín-Fernández 2015), which imputes zeros in compositional count datasets based on Bayesian-multiplicative replacement (Martín-Fernández et al. 2015; Palarea-Albaladejo and Martín-Fernández 2015). Specifically, this method imputes zero counts and then multiplicatively adjusts the remaining non-zero components to produce a set of proportions that still sum to one (Martín-Fernández et al. 2015; Palarea-Albaladejo and Martín-Fernández 2015).

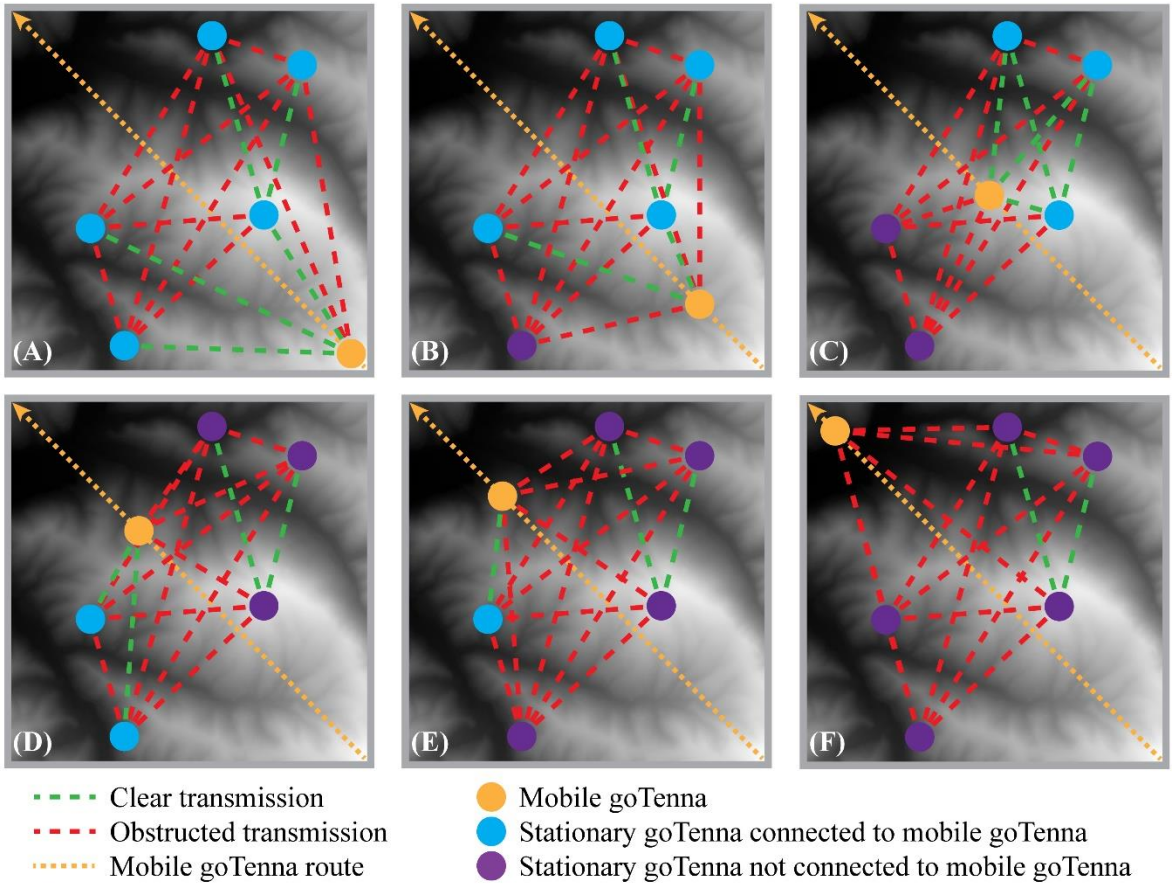

Figure 4.2. Example locations of the one mobile and five stationary goTenna Pros that may result in each of the six connectivity levels. The mobile goTenna is shown at various locations along the diagonal walking path within a PLSS section. Panels A–F represent connectivity levels Con_6–Con_1, respectively. These connectivity levels correspond to instances in which five, four, three, two, one, or zero stationary devices are connected to the mobile goTenna Pro, respectively.

Table 4.2. The six compositional response variables representing the six connectivity levels and calculation methods.

Variable	**Description**	**Calculation**
Con_6	Proportion of time the full network of six devices (i.e., all five stationary goTennas and one mobile goTenna) were connected	# of signals received by all five stationary goTennas / # of total transmitted signals sent from mobile goTenna
Con_5	Proportion of time five devices (i.e., four stationary goTennas and one mobile goTenna) were connected	# of signals received by four stationary goTennas / # of total transmitted signals sent from mobile goTenna
Con_4	Proportion of time four devices (i.e., three stationary goTennas and one mobile goTenna) were connected	# of signals received by three stationary goTennas / # of total transmitted signals sent from mobile goTenna
Con_3	Proportion of time three devices (i.e., two stationary goTennas and one mobile goTenna) were connected	# of signals received by two stationary goTennas / # of total transmitted signals sent from mobile goTenna

Con_2	Proportion of time two devices (i.e., one stationary goTenna and one mobile goTenna) were connected	# of signals received by one stationary goTenna / # of total transmitted signals sent from mobile goTenna
Con_1	Proportion of time zero stationary goTennas were connected to the mobile goTenna	# of signals received by zero stationary goTennas / # of total transmitted signals sent from mobile goTenna

4.3.3.2 Dirichlet regression

Dirichlet regression is a multivariate generalization of beta regression and can be used to analyze compositional data (Gueorguieva et al. 2008). It has been used in forestry to model compositional data, specifically to predict forestry planned end products (Hickey et al. 2015), species proportions for forest inventories (Puliti et al. 2017), and biomass component proportions (Poudel and Temesgen 2016; Zhao et al. 2016; Eker et al. 2017; Poudel et al. 2019). In the common parameterization of the Dirichlet distribution, there is a shape parameter α_c for each of the c components. The expected value of any given component y_c is $E[y_c] = \alpha_c/\alpha_0$, where α_0 is the sum of all α_c's. The α_c's are modeled using explanatory variables with a log link using Eq (2):

$$\log(\alpha_{ij}) = a_i + \beta_i z_j \quad (2)$$

Where z_j are the explanatory variables for the jth observation ($j = 1, \ldots, n$), a_i are the intercepts for the ith component ($i = 1, \ldots c$), and β_i are the regression coefficients for the ith component ($i = 1, \ldots c$). The expected values of α_c are then derived as $\hat{\alpha}_{ij} = \exp(\hat{a}_i + \hat{\beta}_i z_j)$. The DirichReg function in the R DirichletReg package (Maier 2014, 2021) was used to fit Dirichlet regression models with the common parameterization to the lidar- and satellite-derived terrain and vegetation metrics in order to predict connectivity. Models were created using 1) both lidar- and satellite-derived metrics (LIDSAT); 2) lidar-derived metrics only (LID); and 3) satellite-derived metrics only (SAT). All lidar- and satellite-derived predictor variables were normalized using the maximum and minimum values of each variable. Because so many predictor variables were calculated using the remote sensing data, the Boruta algorithm implemented in the R Boruta package was used to select candidate predictors for each normalized variable set (LIDSAT, LID, SAT) (Kursa and Rudnicki 2010). The Boruta algorithm is a feature selection method based on the random forest algorithm (Kursa and Rudnicki 2010) and has been used effectively with high dimensional remote sensing data (Leutner et al. 2012; Blackburn et al. 2021). The Boruta algorithm was run 100 times for each of the six proportion responses (i.e., connectivity levels) and for each of the three variable sets using a maximum number of 1000 runs each time. The number of times each variable was selected by the algorithm was summed across the 100 iterations. After Boruta feature selection, the number of predictor variables for the six

connectivity levels ranged from 17 to 75 for the LIDSAT dataset, 2 to 69 for the LID dataset, and 5 to 27 for the SAT dataset. Because many of these Boruta-selected variables were highly correlated, variables that had correlations > |0.7| were removed and all remaining variables were used to build the initial models. Because each component is allowed to have different explanatory variables when fitting Dirichlet regression models under the common parameterization, all initial models were built using the uncorrelated Boruta-selected variables specific to each connectivity level. As a result, the initial model built with the LIDSAT dataset had between 3 to 12 predictors for each proportion response, the initial model built with the LID dataset had between 1 to 10 predictors for each proportion response, and the initial model built with the SAT dataset had between 2 to 5 predictors for each proportion response. For each of the three initial models, variables were removed one at a time in order of highest *p*-values until arriving at the null model with only intercepts for each proportion level. All models created for each dataset were arranged in order of increasing number of parameters and were compared using analysis of variance (ANOVA), which when used in the DirichletReg package uses a likelihood ratio test to perform pairwise tests of Dirichlet regression models. Models were iteratively removed through ANOVA until a final model for each dataset was selected. These three final models were evaluated by four statistics using leave-one-out cross validation (LOOCV): mean absolute error (MAE), root mean squared error (RMSE), mean bias, and mean relative bias (bias%) using Eqs (3–6).

$$MAE = \frac{\sum_{i=1}^{n}\left|Y_i - \hat{Y}_i\right|}{n} \tag{3}$$

$$RMSE = \sqrt{\frac{\sum_{i=1}^{n}\left(Y_i - \hat{Y}_i\right)^2}{n}} \tag{4}$$

$$bias = \frac{\sum_{i=1}^{n}\left(Y_i - \hat{Y}_i\right)}{n} \tag{5}$$

$$bias\% = \frac{bias}{\bar{Y}} \tag{6}$$

Where n is the number of observations, Y_i is the ith observed proportion, $\hat{Y}_i$ is the ith predicted proportion from the model fitted using the (n–1) data, and $\bar{Y}$ is the mean of the observed proportions.

4.4 Results

Summary statistics of the six connectivity levels showed that the mean proportion of time all five stationary devices were connected to the mobile goTenna (Con_6) was 0.326 (s = 0.332), the mean proportion of time four of the stationary devices were connected to the mobile goTenna (Con_5) was 0.141 (s = 0.157), the mean proportion of time three of the stationary devices were connected to the mobile goTenna (Con_4) was 0.106 (s = 0.133), the mean proportion of time two of the stationary devices were connected to the mobile goTenna (Con_3) was 0.110 (s = 0.121), the mean proportion of time one of the stationary devices was connected to the mobile goTenna (Con_2) was 0.136 (s = 0.168), and the mean proportion of time zero stationary devices were connected to the mobile goTenna (Con_1) was 0.182 (s = 0.125) (Table 4.3).

Table 4.3. Summary statistics of the six connectivity levels of the dependent variable (proportion of time connected).

Connectivity level	Mean	SD	Range
Con_6	0.326	0.332	0.000-0.905
Con_5	0.141	0.157	0.000-0.506
Con_4	0.106	0.133	0.008-0.500
Con_3	0.110	0.121	0.004-0.406
Con_2	0.136	0.168	0.000-0.559
Con_1	0.182	0.125	0.000-0.445

There was high variability in the number of times variables in each category were selected by the Boruta algorithm for each connectivity level over the 100 iterations (Figure 4.3). For Con_1, lidar voxel height-related metrics were selected most frequently for both the LIDSAT and LID datasets and satellite GLCM texture metrics were selected most frequently for the SAT dataset. For Con_2, only satellite-based GLCM texture and surface reflectance metrics were selected for the LIDSAT and SAT datasets, and only lidar voxel height metrics were selected for the LID dataset. For both Con_3 and Con_4, lidar voxel point density-related metrics were selected most frequently for the LIDSAT and LID datasets. For the SAT dataset, both GLCM texture and surface reflectance metrics were selected relatively frequently for Con_3 and GLCM texture metrics were selected most frequently for Con_4. For Con_5, lidar-derived voxel intensity and cloud intensity metrics were selected most frequently for the LIDSAT dataset, while lidar-derived voxel intensity, cloud intensity, and cloud height metrics were all selected relatively frequently for the LID dataset. Only satellite GLCM texture metrics were selected for the SAT dataset for Con_5, and relatively infrequently. For Con_6, lidar voxel point density and voxel height metrics as well as satellite GLCM texture metrics were selected most frequently for the LIDSAT dataset, while voxel point density and voxel height metrics were selected

most frequently for the LID dataset. For the SAT dataset, GLCM texture metrics were selected most frequently for Con_6. Additionally, among the categories, lidar voxel point density metrics were selected much more frequently than variables in other categories. These metrics were selected most frequently for Con_3 and Con_4. Satellite GLCM texture metrics were also selected very frequently and for all six connectivity levels, but most often for Con_3.

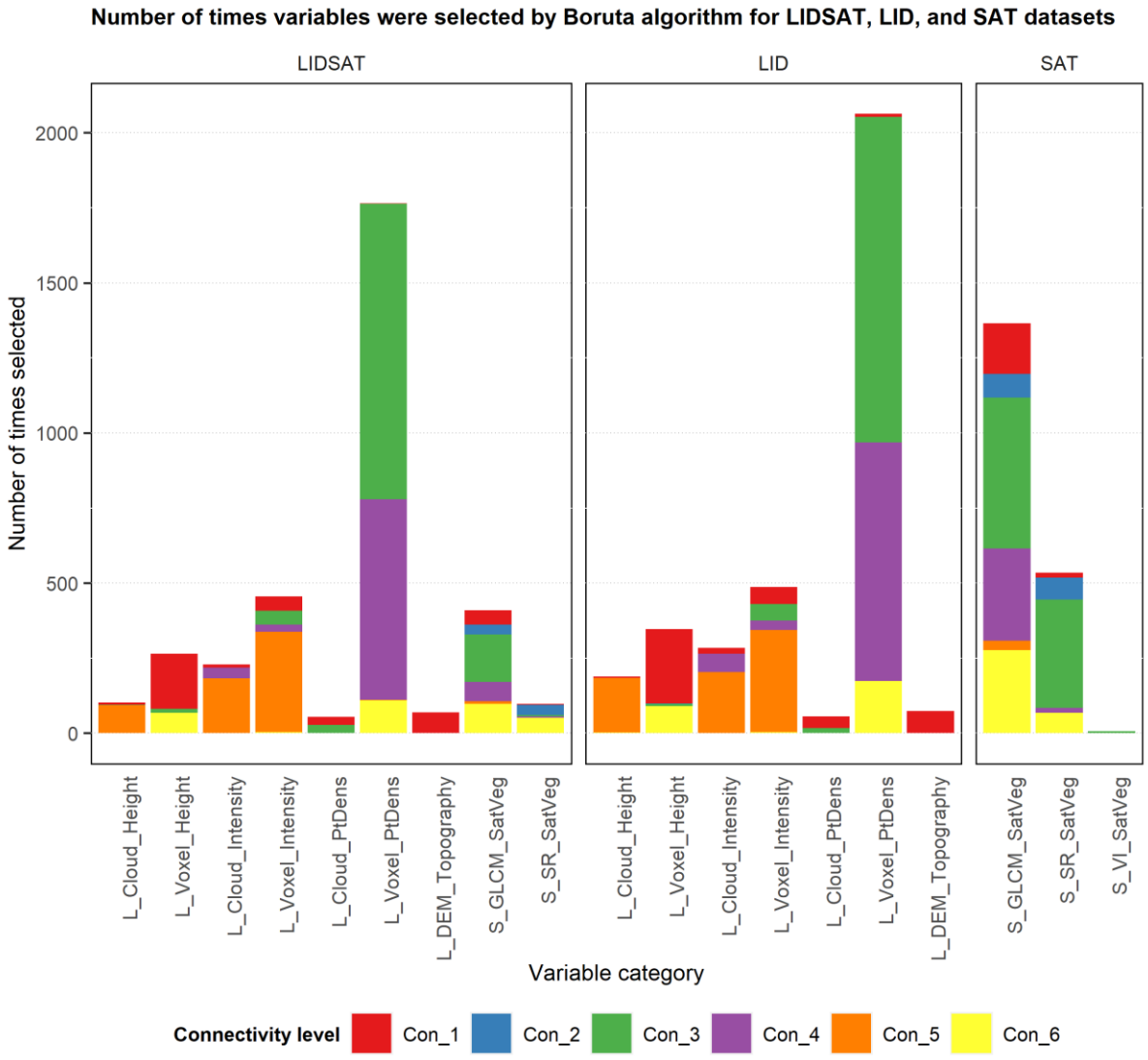

Figure 4.3. Bar chart of the number of times variables in each category were selected by the 100 iterations of the Boruta algorithm for the LIDSAT, LID, and SAT datasets.

There was also variability in the number of unique variables from each category that were selected by the Boruta algorithm for each connectivity level over the 100 iterations (Figure 4.4). For

Con_1, a large number of lidar voxel height and lidar cloud point density metrics were selected for the LIDSAT and LID datasets. There were also many satellite GLCM texture metrics selected for Con_1 for the LIDSAT and SAT datasets. For Con_2, there were more satellite GLCM texture metrics selected than surface reflectance metrics for both the LIDSAT and SAT datasets, while only a few lidar voxel height metrics were selected for the LID dataset. For Con_3, there were many lidar voxel point density-related metrics selected for both the LIDSAT and LID datasets, and many GLCM texture metrics selected for the SAT dataset. For Con_4, a large number of voxel point density metrics and satellite GLCM texture metrics were selected for the LIDSAT dataset and many voxel point density metrics were selected for the LID dataset. For the SAT dataset, a large number of GLCM texture metrics were selected for Con_4. For Con_5, there were many lidar voxel intensity metrics selected for both the LIDSAT and LID datasets and a relatively smaller number of GLCM texture metrics selected for the SAT dataset. For Con_6, there were a large number of lidar voxel point density metrics selected for both the LIDSAT and LID datasets, and quite a few GLCM texture metrics selected for both the LIDSAT and SAT datasets.

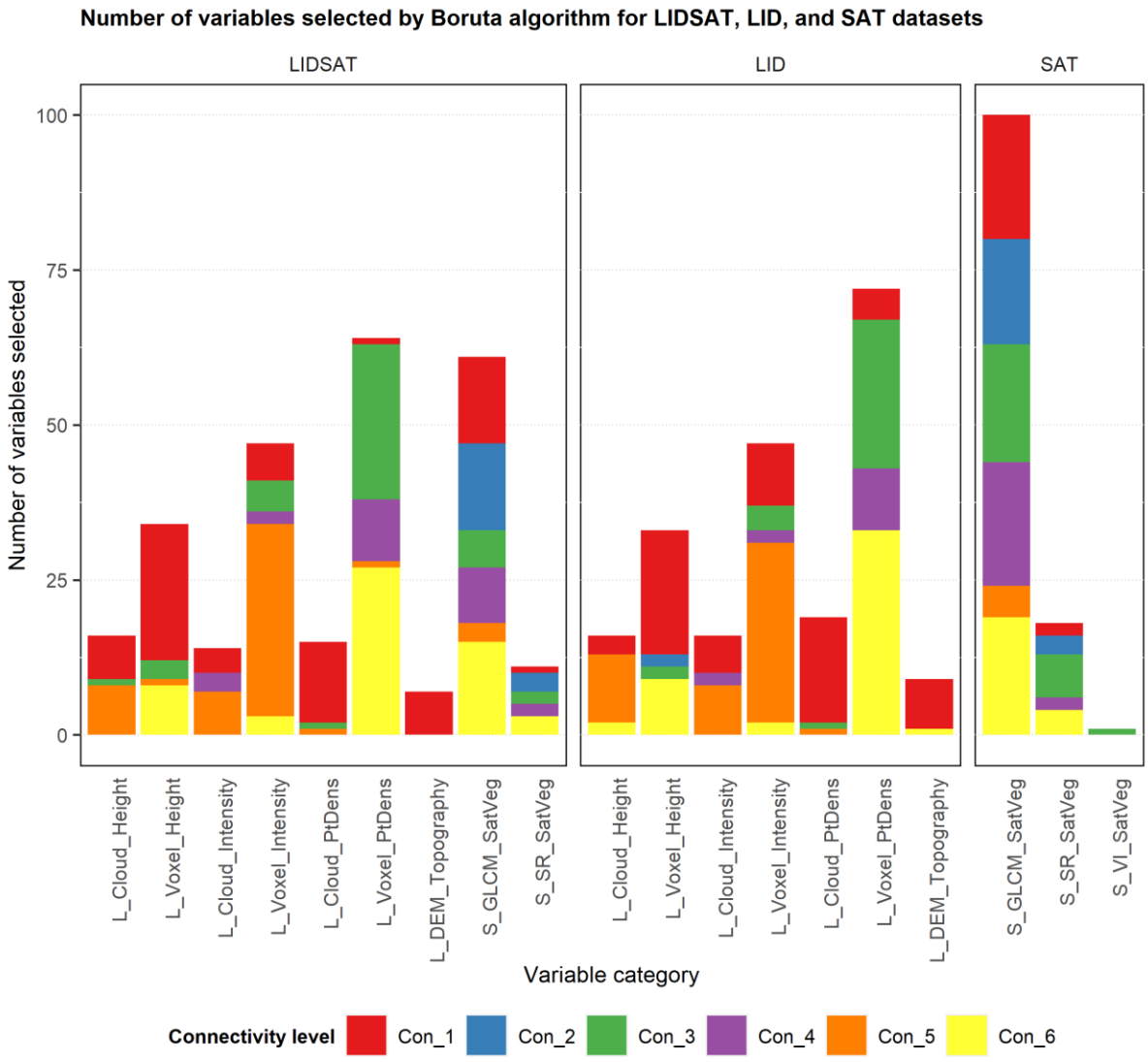

Figure 4.4. Bar chart of the number of variables from each category that were selected by the 100 iterations of the Boruta algorithm for the LIDSAT, LID, and SAT datasets.

The final LIDSAT model fitted to the entire dataset had between one and four predictor variables for each proportion (Table 4.4). Parameters for all predictor variables were significant ($p \leq 0.05$). Four of these variables were satellite GLCM texture metrics, two were lidar voxel height metrics, four were lidar voxel intensity metrics, three were lidar voxel point density metrics, and one was a lidar point cloud intensity metric. All predictors are related to vegetation, rather than topography.

Table 4.4. Summary of LIDSAT Dirichlet model regression coefficients for each of the six connectivity levels. Coefficients in bold are significant ($p \leq 0.05$).

Variable	Model term	Estimate	SE	*z*-value	*p*-value
Con_6	(Intercept)	-2.118	0.473	-4.481	**7.446E-06**
	variance_Mean_B6_5	1.278	0.431	2.961	**3.062E-03**
	variance_SD_B5_3	2.817	0.534	5.276	**1.320E-07**
	z_IQR_kurt_4m	1.540	0.552	2.788	**5.297E-03**
Con_5	(Intercept)	-0.471	0.402	-1.172	2.412E-01
	i_cv_var_3m	3.431	0.609	5.635	**1.753E-08**
	contrast_SD_B5_9	-1.474	0.739	-1.994	**4.617E-02**
Con_4	(Intercept)	-2.905	0.858	-3.386	**7.090E-04**
	i_skew_kurt_4m	2.264	0.689	3.287	**1.013E-03**
	npoints_above_mean_4m	2.400	0.959	2.503	**1.232E-02**
	icum_qHt_15_last	2.260	0.902	2.507	**1.218E-02**
Con_3	(Intercept)	-0.363	0.239	-1.518	1.291E-01
	npoints_above_IQR_3m	1.325	0.520	2.550	**1.077E-02**
Con_2	(Intercept)	-1.474	0.388	-3.801	**1.440E-04**
	dissimilarity_Mean_B1_9	3.466	0.714	4.850	**1.232E-06**
Con_1	(Intercept)	1.859	0.554	3.359	**7.821E-04**
	z_skew_mean_3m	-4.285	1.371	-3.126	**1.769E-03**
	i_var_kurt_3m	-2.389	0.965	-2.475	**1.331E-02**
	i_skew_IQR_4m	2.059	0.868	2.371	**1.775E-02**
	P_Di_sd_4m	-1.620	0.717	-2.260	**2.383E-02**

The final LID model fitted to the entire dataset had three predictor variables for Con_6, one predictor each for Con_5, Con_4, Con_3, and Con_1, and only an intercept for Con_2 (Table 4.5). The parameters for six of the seven predictor variables were significant ($p \leq 0.05$), while the parameter for one predictor for Con_6 (SRR) was not ($p = 0.08$). Three of these variables were lidar voxel intensity metrics, two were lidar voxel point density metrics, and two were lidar DEM-based metrics. The five voxel-based metrics are related to vegetation while the two DEM-based metrics (SRR and HLI_Mean) are related to topography.

Table 4.5. Summary of LID Dirichlet model regression coefficients for each of the six connectivity levels. Coefficients in bold are significant ($p \leq 0.05$).

Variable	Model term	Estimate	SE	*z*-value	*p*-value
Con_6	(Intercept)	1.126	0.724	1.556	1.197E-01
	i_sd_kurt_3m	2.848	0.823	3.462	**5.371E-04**
	npoints_above_var_5m	-1.637	0.818	-2.001	**4.544E-02**
	SRR	-1.574	0.904	-1.740	8.179E-02

Con_5	(Intercept)	-0.794	0.316	-2.514	**1.194E-02**
	i_skew_var_3m	2.021	0.667	3.030	**2.444E-03**
Con_4	(Intercept)	-0.791	0.313	-2.527	**1.150E-02**
	i_skew_kurt_4m	1.330	0.652	2.040	**4.139E-02**
Con_3	(Intercept)	-0.527	0.244	-2.161	**3.073E-02**
	npoints_above_IQR_3m	1.219	0.545	2.237	**2.529E-02**
Con_2	(Intercept)	-0.272	0.189	-1.438	1.504E-01
Con_1	(Intercept)	1.013	0.394	2.568	**1.023E-02**
	HLI_Mean	-2.143	0.935	-2.292	**2.188E-02**

The final SAT model fitted to the entire dataset had one predictor variable each for Con_6, Con_5, Con_2, and Con_1 and only an intercept for Con_4 and Con_3 (Table 4.6). Parameters for all four predictors were significant ($p \leq 0.05$), and all were GLCM texture metrics related to vegetation.

Table 4.6. Summary of SAT Dirichlet model regression coefficients for each of the six connectivity levels. Coefficients in bold are significant ($p \leq 0.05$).

Variable	**Model term**	**Estimate**	**SE**	***z*-value**	***p*-value**
Con_6	(Intercept)	-1.308	0.339	-3.862	**1.125E-04**
	variance_SD_B5_3	3.201	0.592	5.409	**6.323E-08**
Con_5	(Intercept)	0.325	0.301	1.081	2.797E-01
	contrast_SD_B5_3	-1.398	0.656	-2.131	**3.306E-02**
Con_4	(Intercept)	-0.442	0.192	-2.304	**2.123E-02**
Con_3	(Intercept)	-0.352	0.191	-1.848	6.457E-02
Con_2	(Intercept)	-0.977	0.335	-2.919	**3.514E-03**
	contrast_Mean_B1_3	1.857	0.739	2.512	**1.200E-02**
Con_1	(Intercept)	0.741	0.347	2.131	**3.305E-02**
	mean_Mean_B5_3	-1.573	0.696	-2.258	**2.396E-02**

LOOCV showed that MAE ranged from 0.082 to 0.249 for the LIDSAT model, from 0.081 to 0.258 for the LID model, and from 0.102 to 0.256 for the SAT model (Table 4.7). RMSE ranged from 0.101 to 0.314 for the LIDSAT model, from 0.103 to 0.310 for the LID model, and from 0.121 to 0.313 for the SAT model (Table 4.7). Bias ranged from -0.048 to 0.073 for the LIDSAT model, from -0.030 to 0.083 for the LID model, and from -0.029 to 0.092 for the SAT model (Table 4.7). Bias% ranged from -26.2% to 22.5% for the LIDSAT model, from -27.1% to 25.5% for the LID model, and from -19.6% to 28.2% for the SAT model (Table 4.7). Bias was negative for Con_5, Con_4, Con_3, and Con_1 in all three final models and for Con_2 in the SAT model (Table 4.7), meaning these models tended to overpredict the proportion. Bias was positive for Con_6 in all three final models and

for Con_2 in the LIDSAT and LID models (Table 4.7), meaning these models tended to underpredict the proportion.

Table 4.7. Accuracy metrics calculated for each connectivity level using LOOCV.

		Connectivity level					
Metric	**Model**	**Con_6**	**Con_5**	**Con_4**	**Con_3**	**Con_2**	**Con_1**
MAE	**LIDSAT**	0.249	0.083	0.084	0.082	0.119	0.123
	LID	0.258	0.106	0.093	0.081	0.137	0.091
	SAT	0.256	0.116	0.107	0.102	0.130	0.104
RMSE	**LIDSAT**	0.314	0.117	0.110	0.101	0.157	0.159
	LID	0.310	0.133	0.111	0.103	0.173	0.110
	SAT	0.313	0.145	0.129	0.122	0.162	0.121
bias	**LIDSAT**	0.073	-0.005	-0.019	-0.019	0.017	-0.048
	LID	0.083	-0.019	-0.021	-0.030	0.013	-0.026
	SAT	0.092	-0.019	-0.015	-0.022	-0.007	-0.029
bias%	**LIDSAT**	22.5	-3.7	-17.8	-16.8	12.5	-26.2
	LID	25.5	-13.2	-20.3	-27.1	9.5	-14.3
	SAT	28.2	-13.7	-14.0	-19.6	-4.8	-16.2

Boxplots of the observed and predicted proportions calculated using the final LIDSAT, LID, and SAT models fitted to the entire dataset illustrate the wide variability in the data, especially for the Con_6 connectivity level (Figure 4.5). The boxplots further illustrate how the three final models tended to overpredict the Con_5, Con_4, Con_3, and Con_1 connectivity levels (Figure 4.5). The boxplots also show how all three final models tended to underpredict the Con_6 connectivity level (Figure 4.5).

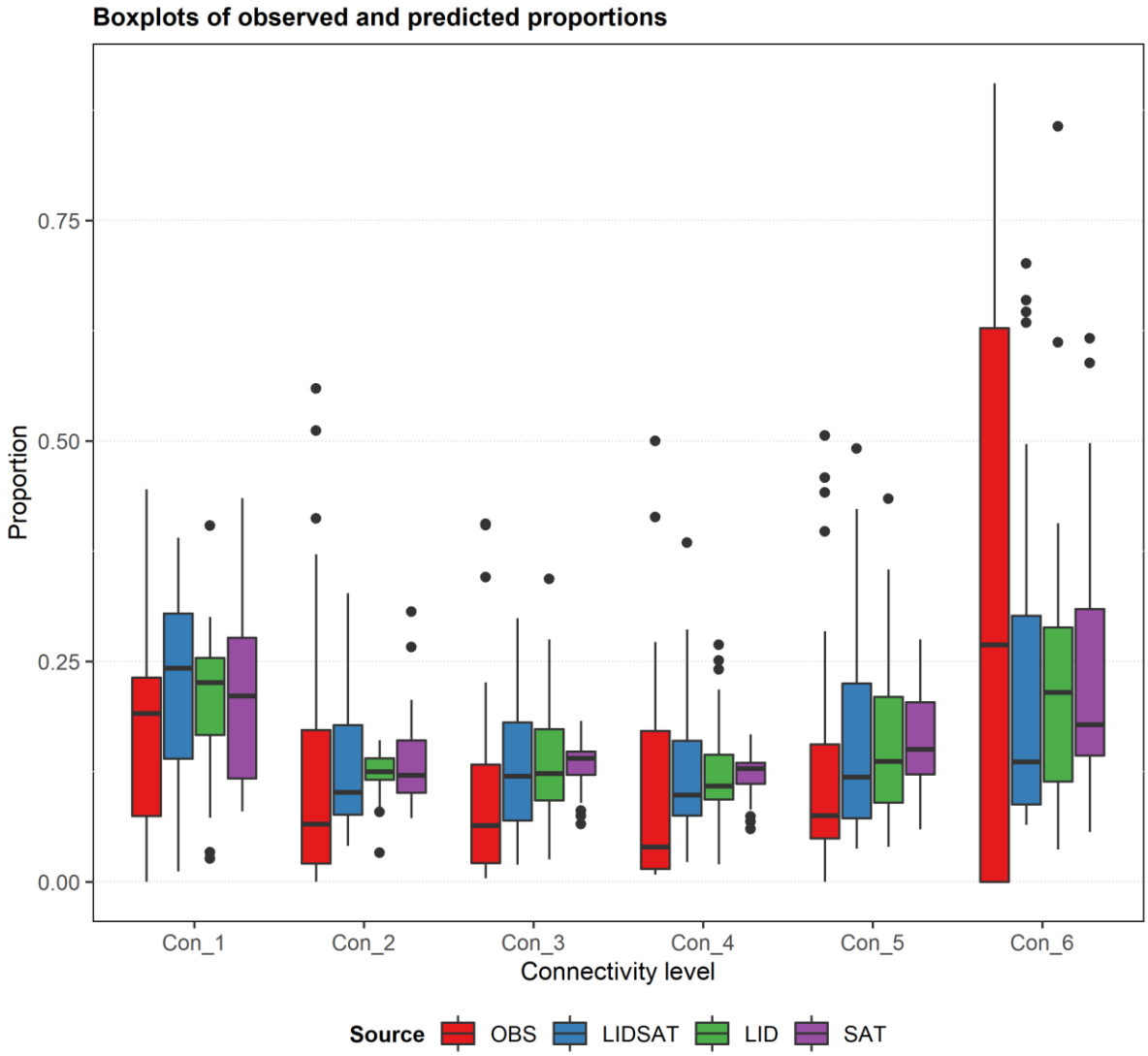

Figure 4.5. Boxplots of observed and predicted proportions of the six connectivity levels. Predictions were obtained using the final LIDSAT, LID, and SAT models fitted to the entire dataset.

4.5 Discussion

In this study, we characterized the connectivity of smartphone-based goTenna mesh radio networks for location sharing in forests using lidar and satellite remote sensing data and developed Dirichlet regression models to predict the connectivity of these networks over a range of vegetation and topographic conditions. Our results showed that for a network of six devices with one mobile device and five deployed at randomized, stationary locations over PLSS sections approximately 260 ha in area, the full network was connected, on average, only 32.6% of the time and the mobile

goTenna Pro was disconnected from all other devices 18.2% of the time. There was also a wide range in the proportion of time all six devices were connected (0.000–0.905). The network was never fully connected in some sections, while in others, the full network was connected 90.5% of the time. Similarly, the mobile goTenna was not connected to any other device between 0% and 44.5% of the time, depending on the section. This high variability in network connectivity has important implications for wildland fire incident command and other public health and safety applications of mesh networks in forests. Wildland fire managers, search and rescue personnel, forestry and logging workers, and others relying on these networks for improved situational awareness and safety should anticipate gaps in connectivity during which one or more individuals may not be able to communicate or share locations on the network.

The variables most commonly chosen by the Boruta variable selection algorithm were lidar voxel point density metrics as well as voxel intensity metrics for the two datasets with lidar data (LIDSAT and LID). The lidar DEM-based topography variables were selected much less frequently than the lidar point cloud and voxel predictors more related to vegetation. Satellite GLCM metrics were selected more frequently by the Boruta algorithm compared to the surface reflectance and NDVI metrics for the two datasets with satellite data (LIDSAT and SAT). The majority of predictors in the final LIDSAT model were lidar voxel metrics, which represented aspects of lidar intensity, point density, and canopy height. However, a variety of satellite GLCM texture variables were also present in the final LIDSAT model, suggesting that both lidar and satellite data were important or complementary predictors of connectivity. Most of the predictors in the final LID model were lidar voxel metrics representing aspects of intensity and point density. However, this model also had two lidar DEM variables related to topography, which is in contrast to the LIDSAT model that depended primarily on vegetation. The final SAT model only had GLCM texture variables, suggesting that these were better predictors of connectivity than surface reflectance or NDVI. While we had anticipated that topography would be an important predictor of connectivity, the relatively minor presence of DEM predictors in both the Boruta variable selection and final models shows that vegetation more directly affected network connectivity. This could in part be due to the relationship between the size of each PLSS section and the number of devices deployed. For example, it is possible that using a network of six devices in an approximately 260-ha area was enough to overcome some of the effects of topography on radio signal attenuation, and that vegetation, which is known to affect near-ground peer-to-peer radio signal propagation (Meng et al. 2010; Galvan-Tejada and Duarte-Reynoso 2012; Gay-Fernández and Cuiñas 2013; Anastassiu et al. 2014; Smith et al. 2016),

most impacts connectivity. Future work should evaluate the relationship between connectivity, number of devices, and study area.

Both the final LID and SAT models had connectivity levels without a predictor variable, which suggests that some connectivity levels may have been related only to the lidar or satellite data. In particular, Con_2 was modeled with only an intercept in the final LID model, but had a significant satellite predictor in both the LIDSAT and SAT models. This suggests that this level of connectivity (i.e., the proportion of time that the mobile goTenna was connected to just one stationary device) could be modeled with satellite data better than lidar data. Both Con_3 and Con_4 only had intercepts in the SAT model but had significant lidar-based predictors in both the LIDSAT and LID models, indicating that these two levels of connectivity (i.e., the proportion of time the mobile goTenna was connected to either two or three stationary devices) could be modeled with lidar data better than satellite data. This is somewhat surprising based on the Boruta results, in which satellite GLCM and surface reflectance metrics were selected commonly for Con_3 and satellite GLCM metrics were selected commonly for Con_4, both in terms of the number and frequency of variable selection. In contrast to the LID and SAT models, the LIDSAT model had significant predictors for each connectivity level, suggesting that using both data sources may be more useful than using just lidar or satellite data for prediction.

MAE, RMSE, and bias were all worse for the Con_6 connectivity level compared to the other connectivity levels for all three final models. Bias% was worse for the Con_1, Con_3, and Con_6 connectivity levels for the LIDSAT, LID, and SAT models, respectively, compared to the other connectivity levels. These accuracy metrics were slightly better for the LIDSAT model compared to the other two for most proportion levels, but worse than the other two models for the Con_1 connectivity level. This suggests that both the LID and SAT models predicted the proportion of time that the mobile goTenna Pro was not connected to any other device somewhat better than the model using both data sources, but that the LIDSAT model predicted the proportion of time that the mobile device was connected to one or more stationary devices slightly better than either the LID or SAT model in most cases. Finally, all three models tended to underpredict the proportion of time that the mobile goTenna Pro was connected to all five stationary devices (Con_6) and to overpredict the proportion of time the mobile goTenna Pro was not connected to any other device (Con_1).

In practice, wildland fire incident command teams may place a device on a high point such as an overhead aircraft to serve as a relay node and potentially improve connectivity. The effect of utilizing dedicated overhead relay nodes was not evaluated in our study. Future work should

investigate the potential for improved transmission by using relay nodes as well as a higher density of devices. In particular, using a relay node may affect whether devices primarily transmit to one another either horizontally with cumulative vegetation effects on path loss, or vertically through forest canopy vegetation. It is important to note, however, that mesh radios used during Initial Attack on small fires may not have aircraft present to support a dedicated relay node.

The connectivity data used in this study were compositional data that were nonnegative proportions of time that different numbers of devices were connected. The unit-sum constraint of compositional data restricts the types of analytical approaches that are appropriate. By using Dirichlet regression, our approach guaranteed that the predictions of all proportional components summed to one. One limitation to our study was the sample size (n = 24) in relation to the number of components, or connectivity levels, which was determined by the number of devices in the mesh network (six). Considerations for future work should include further evaluation of the relationship between sample size and the number of network components. In particular, a larger sample size may be necessary to investigate networks with more than six devices, as those would result in more components and thus a larger number of estimated model parameters.

4.6 Conclusions

This is the first study reporting the connectivity of smartphone-based goTenna Pro mesh networks replicated across a wide range of terrain and vegetation conditions. The results show that remote sensing can successfully be used to characterize network connectivity. Vegetation affected connectivity more than topography, and the performance of these networks varied widely across sites. Initial Attack crews responding to wildland fires should anticipate gaps in real-time location tracking required on Type I fires in the United States under the Dingell Act. The Dirichlet regression models we have developed may be used to predict connectivity over large spatial extents outside of our study areas using available lidar and satellite data as predictors. One important consideration is that most of the lidar metrics used in our models were voxel-based rather than point cloud- or DEM-based. This means computation time should be considered, since voxel-based calculations tend to be more computationally complex than point cloud and DEM calculations. Ultimately, predicting connectivity in similar conditions outside the study area can be used to develop maps that forecast how well similar networks are expected to perform for wildland fire management, forestry, or other safety applications.

4.7 References

Alsayyari A, Kostanic I, Otero C, Almeer M, Rukieh K. An empirical path loss model for wireless sensor network deployment in a sand terrain environment. In: Proceedings of the 2014 IEEE World Forum on Internet of Things (WF-IoT). Seoul, South Korea: IEEE; 2014. p. 218–23. doi:10.1109/WF-IoT.2014.6803162.

Al-Turjman FM, Hassanein HS, Ibnkahla MA. Connectivity optimization for wireless sensor networks applied to forest monitoring. In: Proceedings of the 2009 IEEE International Conference on Communications. Dresden, Germany: IEEE; 2009. p. 1–6. doi:10.1109/ICC.2009.5198845.

Anastassiu HT, Vougioukas S, Fronimos T, Regen C, Petrou L, Zude M, et al. A computational model for path loss in wireless sensor networks in orchard environments. Sensors. 2014 Mar;14(3):5118–35. doi:10.3390/s140305118.

Aschenbruck N, Gerhards-Padilla E, Martini P. Modeling mobility in disaster area scenarios. Perform Eval. 2009 Dec;66(12):773–90. doi:10.1016/j.peva.2009.07.009.

Azevedo JA, Santos FE. A model to estimate the path loss in areas with foliage of trees. Int J Electron Commun AEU. 2017 Jan;71:157–61. doi:10.1016/j.aeue.2016.10.018.

Azevedo JAR, Santos FES. An empirical propagation model for forest environments at tree trunk level. IEEE Trans Antennas Propag. 2011 Jun;59(6):2357–67. doi:10.1109/TAP.2011.2143664.

Blackburn RC. lidRmts [Internet]. 2021 [cited 2022 Mar 2]. Available from: https://github.com/RCBlackburn/lidRmts

Blackburn RC, Buscaglia R, Sánchez Meador AJ. Mixtures of airborne lidar-based approaches improve predictions of forest structure. Can J For Res. 2021 Aug;51(8):1106–16. doi:10.1139/cjfr-2020-0506.

Blanchette D, Fournier RA, Luther JE, Côté J-F. Predicting wood fiber attributes using local-scale metrics from terrestrial LiDAR data: A case study of Newfoundland conifer species. For Ecol Manag. 2015 Jul;347:116–29. doi:10.1016/j.foreco.2015.03.013.

Butler C, Marsh S, Domitrovich JW, Helmkamp J. Wildland firefighter deaths in the United States: A comparison of existing surveillance systems. J Occup Environ Hyg. 2017 Apr;14(4):258–70. doi:10.1080/15459624.2016.1250004.

CoE. 2018 Montrose Helitack TAK deployment report [Internet]. Rifle, CO, USA: Colorado Center of Excellence for Advanced Technology Aerial Firefighting; 2018a. Report No.: CoE-18-003.1. Available from: http://cdpsdocs.state.co.us/coe/Website/TAK/MontroseHelitackATAKDeploymentReport.pdf

CoE. 2018 Overland Hand Crew TAK deployment report [Internet]. Rifle, CO, USA: Colorado Center of Excellence for Advanced Technology Aerial Firefighting; 2018b. Report No.: CoE-18-005.1. Available from: http://cdpsdocs.state.co.us/coe/Website/TAK/Overland_Crew_ATAK_Deployment_Report.pdf

CoE. Report on April 2019 TAK use for search and rescue [Internet]. Rifle, CO, USA: Colorado Center of Excellence for Advanced Technology Aerial Firefighting; 2019. Report No.: CoE-19-002.1. Available from: http://cdpsdocs.state.co.us/coe/Website/TAK/Report_on_April_2019_TAK_Use_for_Search_and_Rescue.pdf

DART Team. DART on the Caldor Fire [Internet]. 2021 [cited 2022 Apr 2]. Available from: https://arcg.is/1DqDfG1

Demetri S, Picco GP, Bruzzone L. Estimating low-power radio signal attenuation in forests: A LiDAR-based approach. In: 2015 International Conference on Distributed Computing in Sensor Systems. Fortaleza, Brazil: IEEE; 2015. p. 71–80. doi:10.1109/DCOSS.2015.17.

Demetri S, Picco GP, Bruzzone L. LaPS: LiDAR-assisted placement of wireless sensor networks in forests. ACM Trans Sens Netw. 2019 Feb;15(2):17. doi:10.1145/3293500.

Dewberry. National Enhanced Elevation Assessment final report [Internet]. Fairfax, VA, USA: Dewberry; 2012 Mar p. 816. Available from: http://www.dewberry.com/services/geospatial/national-enhanced-elevation-assessment

Dube T, Mutanga O. Investigating the robustness of the new Landsat-8 Operational Land Imager derived texture metrics in estimating plantation forest aboveground biomass in resource

constrained areas. ISPRS J Photogramm Remote Sens. 2015 Oct;108:12–32. doi:10.1016/j.isprsjprs.2015.06.002.

Edwards R, Durkin J. Computer prediction of service areas for v.h.f. mobile radio networks. Proc Inst Electr Eng. 1969 Sep 1;116(9):1493–500. doi:10.1049/piee.1969.0270.

Ehbrecht M, Schall P, Juchheim J, Ammer C, Seidel D. Effective number of layers: A new measure for quantifying three-dimensional stand structure based on sampling with terrestrial LiDAR. For Ecol Manag. 2016 Nov;380:212–23. doi:10.1016/j.foreco.2016.09.003.

Eker M, Poudel KP, Özçelik R. Aboveground biomass equations for small trees of brutian pine in Turkey to facilitate harvesting and management. Forests. 2017 Dec;8(12):477. doi:10.3390/f8120477.

Evans IS. General geomorphometry, derivatives of altitude, and descriptive statistics. In: Chorley RJ, editor. Spatial Analysis in Geomorphology. 1st ed. London: Routledge; 1972. p. 17–90.

Evans JS. spatialEco [Internet]. 2021. Available from: https://github.com/jeffreyevans/spatialEco

van Ewijk KY, Treitz PM, Scott NA. Characterizing forest succession in Central Ontario using lidar-derived indices. Photogramm Eng Remote Sens. 2011 Mar;77(3):261–9. doi:10.14358/PERS.77.3.261.

Falkowski MJ, Hudak AT, Crookston NL, Gessler PE, Uebler EH, Smith AMS. Landscape-scale parameterization of a tree-level forest growth model: A k-nearest neighbor imputation approach incorporating LiDAR data. Can J For Res. 2010 Feb;40(2):184–99. doi:10.1139/X09-183.

Feng Y, Audy J-F. Forestry 4.0: A framework for the forest supply chain toward Industry 4.0. Gest Produção. 2020 Dec;27(4):e5677. doi:10.1590/0104-530X5677-20.

Filiposka S, Mishkovski I, Trajkoska BT. Terrain details effect on connectivity in ad hoc wireless networks. Commun Netw. 2013 May 30;05(2B):30. doi:10.4236/cn.2013.52B006.

Filiposka S, Trajanov D. Terrain-aware three-dimensional radio-propagation model extension for NS-2. Simulation. 2011 Jan 1;87(1–2):7–23. doi:10.1177/0037549710374607.

Galvan-Tejada GM, Duarte-Reynoso EQ. A study based on the Lee propagation model for a wireless sensor network on a non-uniform vegetation environment. In: 2012 IEEE Latin-America

Conference on Communications. Cuenca, Ecuador: IEEE; 2012. p. 1–6. doi:10.1109/LATINCOM.2012.6506004.

Gasparri NI, Parmuchi MG, Bono J, Karszenbaum H, Montenegro CL. Assessing multi-temporal Landsat 7 ETM+ images for estimating above-ground biomass in subtropical dry forests of Argentina. J Arid Environ. 2010 Oct;74(10):1262–70. doi:10.1016/j.jaridenv.2010.04.007.

Gay-Fernández JA, Cuiñas I. Peer to peer wireless propagation measurements and path-loss modeling in vegetated environments. IEEE Trans Antennas Propag. 2013 Jun;61(6):3302–11. doi:10.1109/TAP.2013.2254452.

Gay-Fernández JA, Sánchez MG, Cuiñas I, Alejos AV, Sánchez JG, Miranda-Sierra JL. Propagation analysis and deployment of a wireless sensor network in a forest. Prog Electromagn Res. 2010;106:121–45. doi:10.2528/PIER10040806.

Gingras J-F, Charette F. FPInnovations' Forestry 4.0 initiative. In: Proceedings of the 2017 Council on Forest Engineering Annual Meeting [Internet]. Bangor, ME, USA; 2017 [cited 2021 Dec 5]. Available from: http://cofe.org/files/2017_Proceedings/FPInnovations%20Gingras%20Charette%20Forestry%204.0%20for%20COFE%202017.pdf

Gobakken T, Næsset E. Assessing effects of laser point density, ground sampling intensity, and field sample plot size on biophysical stand properties derived from airborne laser scanner data. Can J For Res. 2008 May;38(5):1095–109. doi:10.1139/X07-219.

Goldberg BS, Hall JE, Pham PK, Cho CS. Text messages by wireless mesh network vs voice by two-way radio in disaster simulations: A crossover randomized-controlled trial. Am J Emerg Med. 2021 Oct;48:148–55. doi:10.1016/j.ajem.2021.04.004.

Gómez C, Wulder MA, Montes F, Delgado JA. Modeling forest structural parameters in the Mediterranean pines of Central Spain using QuickBird-2 imagery and Classification and Regression Tree analysis (CART). Remote Sens. 2012 Jan;4(1):135–59. doi:10.3390/rs4010135.

Gonzalez P, Asner GP, Battles JJ, Lefsky MA, Waring KM, Palace M. Forest carbon densities and uncertainties from Lidar, QuickBird, and field measurements in California. Remote Sens Environ. 2010 Jul;114(7):1561–75. doi:10.1016/j.rse.2010.02.011.

González-Ferreiro E, Diéguez-Aranda U, Miranda D. Estimation of stand variables in Pinus radiata D. Don plantations using different LiDAR pulse densities. For Int J For Res. 2012 Apr;85(2):281–92. doi:10.1093/forestry/cps002.

Griffin AMR, Popescu SC, Zhao K. Using LIDAR and normalized difference vegetation index to remotely determine LAI and percent canopy cover. In: Proceedings of SilviLaser [Internet]. Edinburgh, UK; 2008. p. 446–55. Available from: https://citeseerx.ist.psu.edu/viewdoc/download?doi=10.1.1.569.9222&rep=rep1&type=pdf

Gueorguieva R, Rosenheck R, Zelterman D. Dirichlet component regression and its applications to psychiatric data. Comput Stat Data Anal. 2008 Aug;52(12):5344–55. doi:10.1016/j.csda.2008.05.030.

Heidemann HK. Lidar base specification [Internet]. Reston, VA: U.S. Geological Survey; 2018 p. 101. (Techniques and Methods). Report No.: 11-B4. Available from: http://pubs.er.usgs.gov/publication/tm11B4

Hickey C, Kelly S, Carroll P, O'Connor J. Prediction of forestry planned end products using Dirichlet regression and neural networks. For Sci. 2015 Apr;61(2):289–97. doi:10.5849/forsci.14-023.

Hijmans RJ. terra: Spatial data analysis [Internet]. 2021. Available from: https://CRAN.R-project.org/package=terra

Hong X, Gerla M, Pei G, Chiang C-C. A group mobility model for ad hoc wireless networks. In: Proceedings of the 2nd ACM International Workshop on Modeling, Analysis and Simulation of Wireless and Mobile Systems (MSWiM '99). Seattle, WA, USA: ACM; 1999. p. 53–60. doi:10.1145/313237.313248.

Hudak AT, Bright BC, Pokswinski SM, Loudermilk EL, O'Brien JJ, Hornsby BS, et al. Mapping forest structure and composition from low-density LiDAR for informed forest, fuel, and fire management at Eglin Air Force Base, Florida, USA. Can J Remote Sens. 2016 Sep;42(5):411–27. doi:10.1080/07038992.2016.1217482.

Hudak AT, Crookston NL, Evans JS, Falkowski MJ, Smith AMS, Gessler PE, et al. Regression modeling and mapping of coniferous forest basal area and tree density from discrete-return lidar and multispectral satellite data. Can J Remote Sens. 2006 Jan;32(2):126–38. doi:10.5589/m06-007.

Hudak AT, Strand EK, Vierling LA, Byrne JC, Eitel JUH, Martinuzzi S, et al. Quantifying aboveground forest carbon pools and fluxes from repeat LiDAR surveys. Remote Sens Environ. 2012 Aug;123:25–40. doi:10.1016/j.rse.2012.02.023.

Hyyppä J, Yu X, Hyyppä H, Vastaranta M, Holopainen M, Kukko A, et al. Advances in forest inventory using airborne laser scanning. Remote Sens. 2012 May;4(5):1190–207. doi:10.3390/rs4051190.

Idaho Lidar Consortium. Clearwater – Nez Perce 3DEP 2016 [Internet]. [cited 2022 Apr 8]. Available from: https://www.idaholidar.org/data/clearwater-nez-perce-3dep-2016/

Jardosh A, Belding-Royer EM, Almeroth KC, Suri S. Towards realistic mobility models for mobile ad hoc networks. In: Proceedings of the 9th Annual International Conference on Mobile Computing and Networking (MobiCom '03). San Diego, CA, USA: ACM; 2003. p. 217–29. doi:10.1145/938985.939008.

Jiang S, Portillo-Quintero C, Sanchez-Azofeifa A, MacGregor MH. Predicting RF path loss in forests using satellite measurements of vegetation indices. In: 39th Annual IEEE Conference on Local Computer Networks Workshops. Edmonton, AB, Canada: IEEE; 2014. p. 592–6. doi:10.1109/LCNW.2014.6927707.

Joshi GG, Dietrich CB, Anderson CR, Newhall WG, Davis WA, Isaacs J, et al. Near-ground channel measurements over line-of-sight and forested paths. IEE Proc - Microw Antennas Propag. 2005 Dec;152(6):589–96. doi:10.1049/ip-map:20050013.

Kamarudin LM, Ahmad RB, Ong BL, Malek F, Zakaria A, Arif MAM. Review and modeling of vegetation propagation model for wireless sensor networks using OMNeT++. In: 2010 Second International Conference on Network Applications, Protocols and Services. Kedah, Malaysia: IEEE; 2010. p. 78–83. doi:10.1109/NETAPPS.2010.21.

Kayitakire F, Hamel C, Defourny P. Retrieving forest structure variables based on image texture analysis and IKONOS-2 imagery. Remote Sens Environ. 2006 Jun;102(3–4):390–401. doi:10.1016/j.rse.2006.02.022.

Keefe RF, Wempe AM, Becker RM, Zimbelman EG, Nagler ES, Gilbert SL, et al. Positioning methods and the use of location and activity data in forests. Forests. 2019a May;10(5):458. doi:10.3390/f10050458.

Keefe RF, Zimbelman EG, Picchi G. Use of individual tree and product level data to improve operational forestry. Curr For Rep [Internet]. 2022 Apr [cited 2022 Apr 1]; doi:10.1007/s40725-022-00160-3.

Keefe RF, Zimbelman EG, Wempe AM. Use of smartphone sensors to quantify the productive cycle elements of hand fallers on industrial cable logging operations. Int J For Eng. 2019b May;30(2):132–43. doi:10.1080/14942119.2019.1572489.

Kelsey KC, Neff JC. Estimates of aboveground biomass from texture analysis of landsat imagery. Remote Sens. 2014 Jul;6(7):6407–22. doi:10.3390/rs6076407.

Kim E, Lee W-K, Yoon M, Lee J-Y, Son Y, Abu Salim K. Estimation of voxel-based above-ground biomass using airborne LiDAR data in an intact tropical rain forest, Brunei. Forests. 2016 Nov;7(11):259. doi:10.3390/f7110259.

Komsta L, Novomestky F. moments: Moments, cumulants, skewness, kurtosis and related tests [Internet]. 2015. Available from: https://CRAN.R-project.org/package=moments

Kotz D, Newport C, Gray RS, Liu J, Yuan Y, Elliott C. Experimental evaluation of wireless simulation assumptions. In: Proceedings of the 7th ACM International Symposium on Modeling, Analysis and Simulation of Wireless and Mobile Systems (MSWiM '04). Venice, Italy: ACM; 2004. p. 78–82. doi:10.1145/1023663.1023679.

Kursa MB, Rudnicki WR. Feature selection with the Boruta package. J Stat Softw [Internet]. 2010 Sep [cited 2021 Jun 4];36(11). doi:10.18637/jss.v036.i11.

Latifi H, Nothdurft A, Koch B. Non-parametric prediction and mapping of standing timber volume and biomass in a temperate forest: application of multiple optical/LiDAR-derived predictors. Forestry. 2010 Oct;83(4):395–407. doi:10.1093/forestry/cpq022.

Leutner BF, Reineking B, Müller J, Bachmann M, Beierkuhnlein C, Dech S, et al. Modelling forest α-diversity and floristic composition — On the added value of LiDAR plus hyperspectral remote sensing. Remote Sens. 2012 Sep;4(9):2818–45. doi:10.3390/rs4092818.

Lin M-S, Leu J-S, Li K-H, Wu J-LC. Zigbee-based Internet of Things in 3D terrains. Comput Electr Eng. 2013 Aug;39(6):1667–83. doi:10.1016/j.compeleceng.2012.09.018.

Loo ZB, Chong PK, Lee KY, Yap W-S. Improved path loss simulation incorporating three-dimensional terrain model using parallel coprocessors. Wirel Commun Mob Comput. 2017;2017:5492691. doi:10.1155/2017/5492691.

Lu D, Chen Q, Wang G, Moran E, Batistella M, Zhang M, et al. Aboveground forest biomass estimation with Landsat and LiDAR data and uncertainty analysis of the estimates. Int J For Res. 2012 Apr;2012:e436537. doi:10.1155/2012/436537.

Maier MJ. DirichletReg: Dirichlet regression for compositional data in R [Internet]. Vienna, Austria: WU Vienna University of Economics and Business; 2014 Jan. (Research Report Series / Department of Statistics and Mathematics). Report No.: 125. Available from: https://epub.wu.ac.at/4077/

Maier MJ. DirichletReg: Dirichlet regression [Internet]. 2021. Available from: https://github.com/maiermarco/DirichletReg

Marina MK, Das SR. On-demand multipath distance vector routing in ad hoc networks. In: Proceedings of the Ninth International Conference on Network Protocols (ICNP 2001). Riverside, CA, USA: IEEE; 2001. p. 14–23. doi:10.1109/ICNP.2001.992756.

Martín-Fernández JA, Barceló-Vidal C, Pawlowsky-Glahn V. Dealing with zeros and missing values in compositional data sets using nonparametric imputation. Math Geol. 2003 Apr;35(3):253–78. doi:10.1023/A:1023866030544.

Martín-Fernández J-A, Hron K, Templ M, Filzmoser P, Palarea-Albaladejo J. Bayesian-multiplicative treatment of count zeros in compositional data sets. Stat Model. 2015 Apr;15(2):134–58. doi:10.1177/1471082X14535524.

McCune B, Keon D. Equations for potential annual direct incident radiation and heat load. J Veg Sci. 2002 Aug;13(4):603–6. doi:10.1111/j.1654-1103.2002.tb02087.x.

McNab WH. Terrain shape index: Quantifying effect of minor landforms on tree height. For Sci. 1989 Mar;35(1):91–104. doi:10.1093/forestscience/35.1.91.

Meng YS, Lee YH, Ng BC. Path loss modeling for near-ground VHF radio-wave propagation through forests with tree-canopy reflection effect. Prog Electromagn Res M. 2010;12:131–41. doi:10.2528/PIERM10040905.

Müller F, Jaeger D, Hanewinkel M. Digitization in wood supply – A review on how Industry 4.0 will change the forest value chain. Comput Electron Agric. 2019 Jul;162:206–18. doi:10.1016/j.compag.2019.04.002.

Murkowski L. Text - S.47 - 116th Congress (2019-2020): John D. Dingell, Jr. Conservation, Management, and Recreation Act [Internet]. 2019 [cited 2022 Apr 1]. Available from: https://www.congress.gov/bill/116th-congress/senate-bill/47/text

Murphy MA, Evans JS, Storfer A. Quantifying Bufo boreas connectivity in Yellowstone National Park with landscape genetics. Ecology. 2010 Jan;91(1):252–61. doi:10.1890/08-0879.1.

Newman SM, Keefe RF, Brooks RH, Ahonen EQ, Wempe AM. Human factors affecting logging injury incidents in Idaho and the potential for real-time location-sharing technology to improve safety. Safety. 2018 Dec;4(4):43. doi:10.3390/safety4040043.

Nguyen HH, Krug S, Seitz J. Simulation of 3D signal propagation based on real world terrains for Ad-Hoc Network evaluation. In: 2016 9th IFIP Wireless and Mobile Networking Conference (WMNC). Colmar, France: IEEE; 2016. p. 131–7. doi:10.1109/WMNC.2016.7543980.

Olasupo TO, Otero CE. The impacts of node orientation on radio propagation models for airborne-deployed sensor networks in large-scale tree vegetation terrains. IEEE Trans Syst Man Cybern Syst. 2020 Jan;50(1):256–69. doi:10.1109/TSMC.2017.2737473.

Oroza CA, Zhang Z, Watteyne T, Glaser SD. A machine-learning-based connectivity model for complex terrain large-scale low-power wireless deployments. IEEE Trans Cogn Commun Netw. 2017 Dec;3(4):576–84. doi:10.1109/TCCN.2017.2741468.

Oroza CA, Zheng Z, Glaser SD, Tuia D, Bales RC. Optimizing embedded sensor network design for catchment-scale snow-depth estimation using LiDAR and machine learning. Water Resour Res. 2016 Oct;52(10):8174–89. doi:10.1002/2016WR018896.

Palarea-Albaladejo J, Martín-Fernández JA. zCompositions — R package for multivariate imputation of left-censored data under a compositional approach. Chemom Intell Lab Syst. 2015 Apr;143:85–96. doi:10.1016/j.chemolab.2015.02.019.

Papageorgiou C, Birkos K, Dagiuklas T, Kotsopoulos S. Modeling human mobility in obstacle-constrained ad hoc networks. Ad Hoc Netw. 2012 May;10(3):421–34. doi:10.1016/j.adhoc.2011.07.012.

Parker GG, Harmon ME, Lefsky MA, Chen J, Pelt RV, Weis SB, et al. Three-dimensional structure of an old-growth Pseudotsuga-Tsuga canopy and its implications for radiation balance, microclimate, and gas exchange. Ecosystems. 2004 May;7(5):440–53. doi:10.1007/s10021-004-0136-5.

Pathak PH, Dutta R. A survey of network design problems and joint design approaches in wireless mesh networks. IEEE Commun Surv Tutor. 2011;13(3):396–428. doi:10.1109/SURV.2011.060710.00062.

Pearse GD, Morgenroth J, Watt MS, Dash JP. Optimising prediction of forest leaf area index from discrete airborne lidar. Remote Sens Environ. 2017 Oct;200:220–39. doi:10.1016/j.rse.2017.08.002.

Pearse GD, Watt MS, Dash JP, Stone C, Caccamo G. Comparison of models describing forest inventory attributes using standard and voxel-based lidar predictors across a range of pulse densities. Int J Appl Earth Obs Geoinformation. 2019 Jun;78:341–51. doi:10.1016/j.jag.2018.10.008.

Phua M-H, Johari SA, Wong OC, Ioki K, Mahali M, Nilus R, et al. Synergistic use of Landsat 8 OLI image and airborne LiDAR data for above-ground biomass estimation in tropical lowland rainforests. For Ecol Manag. 2017 Dec;406:163–71. doi:10.1016/j.foreco.2017.10.007.

Pike RJ, Wilson SE. Elevation-relief ratio, hypsometric integral, and geomorphic area-altitude analysis. Geol Soc Am Bull. 1971 Apr;82(4):1079–84. doi:10.1130/0016-7606(1971)82[1079:ERHIAG]2.0.CO;2.

Pocewicz AL, Gessler P, Robinson AP. The relationship between effective plant area index and Landsat spectral response across elevation, solar insolation, and spatial scales in a northern Idaho forest. Can J For Res. 2004 Feb;34(2):465–80. doi:10.1139/x03-215.

Pope G, Treitz P. Leaf Area Index (LAI) estimation in boreal mixedwood forest of Ontario, Canada using light detection and ranging (LiDAR) and WorldView-2 imagery. Remote Sens. 2013 Oct;5(10):5040–63. doi:10.3390/rs5105040.

Popescu SC, Zhao K. A voxel-based lidar method for estimating crown base height for deciduous and pine trees. Remote Sens Environ. 2008 Mar;112(3):767–81. doi:10.1016/j.rse.2007.06.011.

Poudel KP, Temesgen H. Methods for estimating aboveground biomass and its components for Douglas-fir and lodgepole pine trees. Can J For Res. 2016 Jan;46(1):77–87. doi:10.1139/cjfr-2015-0256.

Poudel KP, Temesgen H, Radtke PJ, Gray AN. Estimating individual-tree aboveground biomass of tree species in the western U.S.A. Can J For Res. 2019 Jun;49(6):701–14. doi:10.1139/cjfr-2018-0361.

Puliti S, Gobakken T, Ørka HO, Næsset E. Assessing 3D point clouds from aerial photographs for species-specific forest inventories. Scand J For Res. 2017 Jan;32(1):68–79. doi:10.1080/02827581.2016.1186727.

R Core Team. R: A language and environment for statistical computing [Internet]. Vienna, Austria: R Foundation for Statistical Computing; 2021 [cited 2021 Nov 8]. Available from: https://www.r-project.org/

Rappaport TS. Wireless communications: principles and practice. 2nd ed. Upper Saddle River, New Jersey: Prentice Hall PTR; 2002. (Prentice Hall Communications Engineering and Emerging Technologies Series).

Risk Management Committee. NWCG report on wildland firefighter fatalities in the United States: 2007-2016 [Internet]. National Wildfire Coordinating Group; 2017 Dec. Report No.: PMS 841. Available from: https://www.nwcg.gov/publications/841

Roussel J-R, Auty D. lidR: Airborne LiDAR data manipulation and visualization for forestry applications [Internet]. 2021. Available from: https://cran.r-project.org/package=lidR

Royer EM, Toh C-K. A review of current routing protocols for ad hoc mobile wireless networks. IEEE Pers Commun. 1999 Apr;6(2):46–55. doi:10.1109/98.760423.

Schwamborn M, Aschenbruck N. Introducing geographic restrictions to the SLAW human mobility model. In: Proceedings of the 2013 IEEE 21st International Symposium on Modelling, Analysis & Simulation of Computer and Telecommunication Systems. San Francisco, CA, USA: IEEE; 2013. p. 264–72. doi:10.1109/MASCOTS.2013.34.

Smith DP, Messier GG, Wasson MW. Boreal forest low antenna height propagation measurements. IEEE Trans Antennas Propag. 2016 Sep;64(9):4004–11. doi:10.1109/TAP.2016.2583490.

Stepanov I, Rothermel K. On the impact of a more realistic physical layer on MANET simulations results. Ad Hoc Netw. 2008 Jan;6(1):61–78. doi:10.1016/j.adhoc.2006.08.001.

TAK Product Center. ATAK-CIV (Android Team Awareness Kit - Civil Use) [Internet]. 2018 [cited 2022 Apr 8]. Available from: https://play.google.com/store/apps/details?id=com.atakmap.app.civ

Teguh R, Murakami R, Igarashi H. Optimization of router deployment for sensor networks using genetic algorithm. In: Rutkowski L, Korytkowski M, Scherer R, Tadeusiewicz R, Zadeh LA, Zurada JM, editors. ICAISC 2014: Artificial Intelligence and Soft Computing. Zakopane, Poland: Springer International Publishing; 2014. p. 468–79. (Lecture Notes in Computer Science; vol. 8467). doi:10.1007/978-3-319-07173-2_40.

Tenneson K, Patterson MS, Mellin T, Nigrelli M, Joria P, Mitchell B. Development of a regional lidar-derived above-ground biomass model with Bayesian model averaging for use in Ponderosa pine and mixed conifer forests in Arizona and New Mexico, USA. Remote Sens. 2018 Mar;10(3):442. doi:10.3390/rs10030442.

Tseng Y-C, Ni S-Y, Chen Y-S, Sheu J-P. The broadcast storm problem in a mobile ad hoc network. Wirel Netw. 2002 Mar;8(2):153–67. doi:10.1023/A:1013763825347.

University of Chicago. Globus Web App [Internet]. 2022 [cited 2020 Oct 26]. Available from: https://app.globus.org/

U.S. Department of Agriculture. Dingell Act Resource Tracking (DART) [Internet]. U.S. Forest Service. 2020 [cited 2022 Apr 2]. Available from: http://www.fs.usda.gov/science-technology/fire/technology/law/tracking

U.S. Geological Survey. Landsat 8 Collection 2 (C2) Level 2 Science Product (L2SP) Guide [Internet]. 2020 Sep p. 37. Report No.: LSDS-1619 Version 2.0. Available from: https://www.usgs.gov/media/files/landsat-8-collection-2-level-2-science-product-guide

U.S. Geological Survey. EarthExplorer [Internet]. 2022 [cited 2021 Sep 3]. Available from: https://earthexplorer.usgs.gov/

Wang W, Guan X, Wang B, Wang Y. A novel mobility model based on semi-random circular movement in mobile ad hoc networks. Inf Sci. 2010 Feb;180(3):399–413. doi:10.1016/j.ins.2009.10.001.

Wang W, Wang J, Wang M, Wang B, Zhang W. A realistic mobility model with irregular obstacle constraints for mobile ad hoc networks. Wirel Netw. 2019 Feb;25(2):487–506. doi:10.1007/s11276-017-1569-z.

Weiss AD. Topographic position and landforms analysis [Internet]. Poster presented at: ESRI International User Conference; 2001. Available from: http://www.jennessent.com/downloads/TPI-poster-TNC_18x22.pdf

Wempe AM, Keefe RF. Characterizing rigging crew proximity to hazards on cable logging operations using GNSS-RF: Effect of GNSS positioning error on worker safety status. Forests. 2017 Sep;8(10):357. doi:10.3390/f8100357.

Wempe AM, Keefe RF, Newman SM, Paveglio TB. Intent to adopt location sharing for logging safety applications. Safety. 2019 Mar;5(1):7. doi:10.3390/safety5010007.

Wilson MFJ, O'Connell B, Brown C, Guinan JC, Grehan AJ. Multiscale terrain analysis of multibeam bathymetry data for habitat mapping on the continental slope. Mar Geod. 2007 May;30(1–2):3–35. doi:10.1080/01490410701295962.

Woods M, Lim K, Treitz P. Predicting forest stand variables from LiDAR data in the Great Lakes - St. Lawrence forest of Ontario. For Chron. 2008 Dec;84(6):827–39. doi:10.5558/tfc84827-6.

Wu S-L, Lin C-Y, Tseng Y-C, Sheu J-P. A new multi-channel MAC protocol with on-demand channel assignment for multi-hop mobile ad hoc networks. In: Proceedings of the International Symposium on Parallel Architectures, Algorithms and Networks (I-SPAN 2000). Dallas, TX, USA: IEEE; 2000. p. 232–7. doi:10.1109/ISPAN.2000.900290.

Zhao D, Kane M, Teskey R, Markewitz D. Modeling aboveground biomass components and volume-to-weight conversion ratios for loblolly pine trees. For Sci. 2016 Oct;62(5):463–73. doi:10.5849/forsci.15-129.

Zimbelman EG, Keefe RF. Real-time positioning in logging: Effects of forest stand characteristics, topography, and line-of-sight obstructions on GNSS-RF transponder accuracy and radio signal propagation. PLOS ONE. 2018 Jan;13(1):e0191017. doi:10.1371/journal.pone.0191017.

Zimbelman EG, Keefe RF. Development and validation of smartwatch-based activity recognition models for rigging crew workers on cable logging operations. PLOS ONE. 2021 May;16(5):e0250624. doi:10.1371/journal.pone.0250624.

Zimbelman EG, Keefe RF, Strand EK, Kolden CA, Wempe AM. Hazards in motion: Development of mobile geofences for use in logging safety. Sensors. 2017 Apr;17(4):822. doi:10.3390/s17040822.

Zou W, Jing W, Chen G, Lu Y, Song H. A survey of big data analytics for smart forestry. IEEE Access. 2019 Mar;7:46621–36. doi:10.1109/ACCESS.2019.2907999.

Zvoleff A. glcm: Calculate textures from grey-level co-occurrence matrices (GLCMs) [Internet]. 2020. Available from: https://CRAN.R-project.org/package=glcm

Chapter 5: Development and Validation of Smartwatch-based Activity Recognition Models for Rigging Crew Workers on Cable Logging Operations

Published In:

Zimbelman EG, Keefe RF. Development and validation of smartwatch-based activity recognition models for rigging crew workers on cable logging operations. PLOS ONE. 2021 May;16(5):e0250624. doi:10.1371/journal.pone.0250624.

5.1 Abstract

Analysis of high-resolution inertial sensor and global navigation satellite system (GNSS) data collected by mobile and wearable devices is a relatively new methodology in forestry and safety research that provides opportunities for modeling work activities in greater detail than traditional time study analysis. The objective of this study was to evaluate whether smartwatch-based activity recognition models could quantify the activities of rigging crew workers setting and disconnecting log chokers on cable logging operations. Four productive cycle elements (*travel to log*, *set choker*, *travel away*, *clear*) were timed for choker setters and four productive cycle elements (*travel to log*, *unhook*, *travel away*, *clear*) were timed for chasers working at five logging sites in North Idaho. Each worker wore a smartwatch that recorded accelerometer data at 25 Hz. Random forest machine learning was used to develop predictive models that classified the different cycle elements based on features extracted from the smartwatch acceleration data using 15 sliding window sizes (1 to 15 s) and five window overlap levels (0%, 25%, 50%, 75%, and 90%). Models were compared using multiclass area under the Receiver Operating Characteristic (ROC) curve, or AUC. The best choker setter model was created using a 3-s window with 90% overlap and had sensitivity values ranging from 76.95% to 83.59% and precision values ranging from 41.42% to 97.08%. The best chaser model was created using a 1-s window with 90% overlap and had sensitivity values ranging from 71.95% to 82.75% and precision values ranging from 14.74% to 99.16%. These results have demonstrated the feasibility of quantifying forestry work activities using smartwatch-based activity recognition models, a basic step needed to develop real-time safety notifications associated with high-risk job functions and to advance subsequent, comparative analysis of health and safety metrics across stand, site, and work conditions.

5.2 Introduction

Cable logging operations consist of felling, yarding, processing, and loading work phases [1], with the yarding phase often characterized as six distinct cycle elements (outhaul, lateral out, hookup, lateral in, inhaul, and unhook) [2]. Many of the yarding tasks, such as pulling the cable laterally as well as hooking and unhooking logs, are manual, which can cause physiological strain [3]. Logging workers are often fatally injured when struck by objects such as falling trees, limbs, or machines [4–10]. Contact with objects and equipment accounted for 70.9% of fatalities among logging workers in 2017 [9] and 82.1% of fatalities among logging workers in 2018 [10]. Hand fallers and choker setters are particularly susceptible to these "struck-by" incidents, which accounted for 51.3% of injuries among hand fallers and choker setters between July 2010 and June 2015 in Montana and Idaho [8]. In an analysis of cable logging accidents, Tsioras et al. [11] found that broken spar and anchor trees, bouncing cables, and falling objects contributed to the majority of accidents and most incidents occurred when workers were struck by or struck against an object. While the increased mechanization of logging has generally led to a decrease in injury rates, ground crew members working alongside machines, rigging crew workers, and hand fallers are still at risk [4,6,8,12] and may benefit from the use of a variety of positioning and wearable sensor-based technologies that increase situational awareness and reduce accidents.

Monitoring the current activities, safety status and location of individuals relative to workplace hazards on logging operations could be accomplished through (1) real-time location-sharing methods based on GNSS-RF (global navigation satellite system (GNSS) positioning paired with radio frequency (RF) transmission) for use in remote areas [13–17], (2) activity recognition modeling and incident detection, or (3) a combination of both. Human activity recognition involves using wearable sensors to distinguish between human physical activities. Most activity recognition models have been developed for everyday activities, such as walking, sitting, lying, standing, and other common physical movements referred to as activities of daily living (ADLs) [18–21], as well as for recreation and fitness applications [22–24]. Many smartphones and smartwatches are equipped with a variety of embedded sensors such as GNSS chips, accelerometers, gyroscopes, barometers, magnetometers, thermometers, decibel meters (microphones), and optical heart rate sensors [25–30]. Although a variety of purpose-built sensors have been developed, smartphones [26,28,31] and smartwatches [27,29,32–35] are popular for activity recognition modeling because they are ubiquitous and unobtrusive. Leveraging a variety of wearable and positioning sensors to develop occupational activity recognition models in forestry is a first step toward active monitoring that utilizes subsequent model predictions to help inform algorithms identifying falls or high-risk

activities. Real-time prediction of work cycle elements represents an initial step toward informing smart, location- and activity-aware algorithms and alerts associated with detecting incidents and periods of elevated health and safety concern.

Development of activity recognition models generally consists of data collection, preprocessing, feature extraction and selection, and model development (Figure 5.1) [28,36,37]. Due to the advent of microelectromechanical systems (MEMS), inertial sensors have become smaller, more accurate, and less expensive and have been integrated into a variety of wearable sensors [38]. Data from these sensors is collected while users perform the activities of interest and is typically annotated with observed start and stop times. Preprocessing commonly consists of median filtering to remove noise spikes [39] and low pass or high pass filtering to isolate acceleration due to gravity from body acceleration [39–41]. To extract features for model development, a moving, or sliding, window is advanced through the dataset, defining subsets of the data from which relevant time (e.g., mean, median, variance, standard deviation, range, skewness and kurtosis) or frequency (e.g., Fast Fourier Transform and Discrete Transform coefficients) domain features are calculated [30,31,42,43]. In order to reduce dimensionality and select the most useful features, a variety of techniques such as principal component analysis (PCA), singular value decomposition (SVD), linear discriminant analysis (LDA), or kernel discriminant analysis (KDA) can be used [41,44,45]. Finally, the extracted features are used to develop activity recognition models, often using machine learning algorithms such as Decision Trees, Random Forests (RFs), Support Vector Machines (SVMs), k-Nearest Neighbors (k-NN), Naïve Bayes, k-means, Hidden Markov Models (HMMs), Gaussian Mixture Models (GMMs), artificial neural networks (ANNs), and multilayer perceptron (MLP) [28,31,43,46]. More recently, deep learning methods such as Restricted Boltzmann Machine, Autoencoders, Convolutional Neural Networks, and Recurrent Neural Networks have been shown to improve human activity recognition model performance compared to classical machine learning algorithms [47–50]. While deep learning can overcome some of the drawbacks of traditional machine learning by automatically extracting features and using more complex features [48–50], they are generally more computationally expensive and thus have not been widely implemented on resource-limited devices such as smartwatches and smartphones [47].

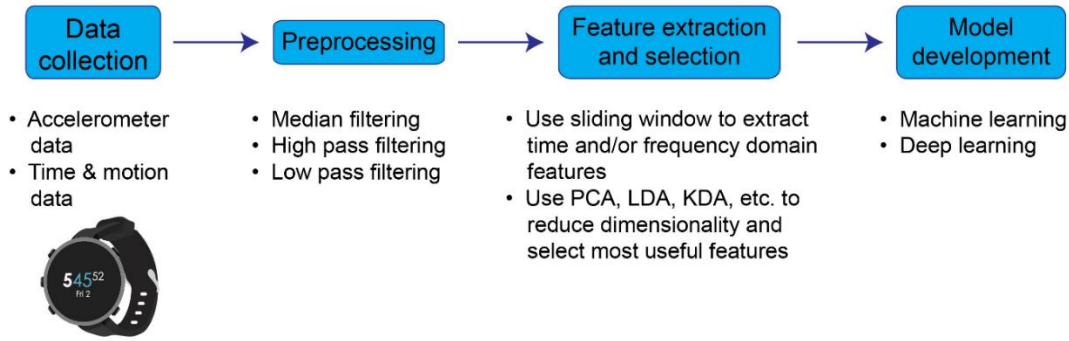

Figure 5.1. Outline of the general activity recognition model development process. Steps involved typically include (1) collecting time study data to pair with wearable sensor measurements, (2) preprocessing the data through filtering, (3) extracting time and/or frequency domain features using a sliding window and then selecting relevant features with which to build models, and (4) developing activity recognition models using machine learning or deep learning techniques. Ultimately, models may be programmed into apps on smartphones and smartwatches and subsequently used to characterize work activities in real-time to inform health and safety notifications.

Model accuracy is thus affected by a variety of factors, such as the type and quality of sensors in the devices, sampling rate, device location on the body, machine learning algorithms employed for model development, features used for classification, and sliding window size used to extract these features [31,42,51]. In terms of window size, there is a tradeoff between detection times and recognition performance since smaller windows allow faster recognition speed [51] but longer windows have been shown to improve recognition performance for more complex, less repetitive activities [34]. In evaluating this tradeoff, Banos et al. [51] compared activity recognition models created with windows ranging in size from 0.25 s to 7 s and found that windows of 1–2 s provided the best accuracy while allowing for quick detection times. The amount of overlap between successive sliding windows also affects model accuracy, with larger overlap often leading to better model performance but at the cost of increased computational load [45]. Models with 50% overlap are common [20,40,52–55], but high accuracies can be obtained using nonoverlapping windows [29,34,51,56]. Recently, “online” activity recognition, which refers to implementing the entire classification process (i.e., data collection and pre-processing, feature extraction, and classification) locally on the device, has been investigated to attain near real-time classifications [31,42]. Online recognition systems have been shown to have classification accuracies of 45.4–98.1% [42,57,58].

While most activity recognition models are specific to ADLs, the high-resolution data collected by these devices may also be useful for quantifying work activities. A limited number of studies have developed activity recognition for occupational activities based on wearable sensors, primarily for construction [59–63], while others have used visual observation or vision sensors to

detect activities in the workplace [64,65]. In natural resources, this approach has recently been proposed by Keefe et al. [30] and Pierzchała et al. [66] developed a method of automatically distinguishing between work phases in cable yarding by fusing data from multiple sensors. New GNSS-enabled smartwatches may offer lightweight alternatives to smartphone-based activity recognition models and may provide additional data that could supplement and improve these models. These types of wearable-based predictive models that quantify work activities on logging operations could inform loggers and equipment operators about their own or their coworkers' job activity status in near real-time, helping to increase situational awareness and safety on active timber sales. New, inexpensive mesh network communications technologies, such as those from goTenna Inc (Brooklyn, NY, USA), enable location- and data-sharing by connecting to smartphones via Bluetooth and allowing users to communicate through radio frequency. In addition to facilitating off-the-grid location-sharing, these devices may also be useful for sharing worker safety status derived from activity recognition models. The record of high-resolution data that results from activity recognition may also form the basis for quantifying occupational health and safety conditions in comparative analyses that span forest stand, site, and work conditions.

Time and motion studies [67] have been used extensively in conventional forest operations research to quantify productive work cycle elements and delay [2,68–73]. By defining and analyzing the individual work cycle elements performed by equipment or by individuals engaged in motor-manual operations, an objective of time study research is often to identify opportunities for improving occupational production rates and reducing delay time [1,2,71,72,74]. Time study analyses are used as the basis for regression [1,2,69,71,74,75] and machine learning [76,77] models that predict work cycle time as a function of stand or site conditions. In order to estimate logging costs per unit wood volume, machine rate estimates determined using methods outlined by Miyata [78] and Brinker et al. [79] are paired with these cycle time prediction models [1,71,74,75,80]. In recent years, GNSS has been used in time studies to automate the estimation of cycle times [81], calculate machine productivity [82], characterize machine movements [83], and improve operational monitoring [84]. Additionally, time and motion studies have been conducted using both GNSS receivers and accelerometers to monitor tree planting [85], characterize manual felling using brush cutters [86], distinguish between chipping tasks [87], and monitor tilt and motion of various harvesters and forwarders in order to analyze operating conditions [88]. The availability of high-resolution sensor data collected seamlessly from GNSS-enabled mobile and wearable devices in real-time provides an opportunity to further model forestry work activities in greater detail than has been done using

traditional methods, while simultaneously providing the basis for improved characterization of digital health and safety.

Prior research evaluating use of wearable sensors to monitor and model forestry work activities includes a small body of recent literature. Fitness and sleep bands have been used (1) to monitor the physical activity and sleep patterns of forestry workers in order to understand how these factors may contribute to workplace hazards [89], and (2) to predict forestry worker fatigue by comparing heart rate and step count data to reaction and decision-making times [90]. Smartwatches paired with heart rate monitor chest straps have been used to evaluate workload associated with manual tree felling [91], while external accelerometers attached to machines have been used to develop ANNs that classify the activities of manually-driven bandsaws [92] and recognize activities associated with manual felling [93]. Preliminary activity recognition models have been developed for cable yarding work phases using a combination of smartphone sensor (global positioning system (GPS) and inertial measurement unit (IMU)) and camera data [66]. However, activity recognition models have yet to be developed for other forestry work positions, such as rigging crew workers setting and disconnecting log chokers. Furthermore, smartwatches have not previously been used in forestry activity recognition, so it is unknown how the prediction accuracy of models developed using these devices will compare to smartphone-based models. Specifically, smartwatches may record different movement patterns than smartphones due in part to different device locations on the body (i.e., wrist vs. hip) [27,34]. In this study, we developed smartwatch-based activity recognition models for rigging crew workers on cable logging operations in order to address two specific research objectives. Our first objective was to develop models that predict choker setter rigging crew work activities with at least 80% sensitivity. Our second objective was to develop models that predict chaser rigging crew work activities with at least 80% sensitivity. Random forest machine learning was used to develop watch-based activity recognition models based on time and motion study data collected on five active timber sales in North Idaho, USA. Model accuracy was calculated based on the percent of time work elements were predicted correctly.

5.3 Materials and methods

5.3.1 Ethics statement

Fourteen loggers voluntarily participated in this study. Prior to data collection, the experimental protocol was approved by the University of Idaho Institutional Review Board (IRB number: 18-202). Participants received both oral and written information regarding the study design

and provided their written, informed consent. Participants were selected based on available, operational cable-logging activities occurring in the North Idaho region during the sampling period and reflect the general demographics of the study population. While we did not collect demographic information from our participants, recent sampling in the region has shown that 55.4% of the logging workforce in Idaho is 50 or more years of age [17]. However, rigging crew workers are generally younger than the median age.

5.3.2 Data collection and processing

Time and motion study (i.e., observational elemental time analysis) data was collected in conjunction with GNSS watch sensor data using two days of sampling on each of five timber sales. Timber sales occurred on state and industrial cable logging operations. Choker setters (who are responsible for setting chokers on logs to be yarded) and chasers (who are responsible for disconnecting chokers from yarded logs) were observed visually. Four productive cycle elements (*travel to log*, *set choker*, *travel away*, *clear*) were timed for the choker setters and four productive cycle elements (*travel to log*, *unhook*, *travel away*, *clear*) were timed for the chasers (Table 5.1). For the choker setter activities, *travel to log* began when the choker setter started walking toward the carriage to grab the chokers. *Set choker* began when the choker setter arrived at a log and began preparing chokers. *Travel away* began when the choker setter finished setting chokers and started to walk away from the log. *Clear* began when the choker setter stopped walking away from the log and was "in the clear". For the chaser activities, *travel to log* began when the chaser started walking toward the landed logs. *Unhook* began when the chaser reached for the chokers to begin unhooking them. *Travel away* began when the chaser finished unhooking the chokers and started to walk away from the log(s). *Clear* began when the chaser stopped walking away from the logs and was "in the clear". For both the choker setter and chaser, *clear* included everything workers did outside of the other three work elements. In order to develop a generalized model for functional use, minor delay events were included within the relevant work element during which they occurred. The clock on a Google Pixel smartphone was used to record the true start and stop times for each work activity cycle using the TimeStamp application (version 0.4.0) [94]. Workers wore Garmin Fenix 5S Plus watches, which record GNSS locations, heart rate, and raw accelerometer data, on their non-dominant wrist. All sensor data was recorded on the Garmin watches using the RawLogger application (version 1.0.20190520a) [95] from Garmin Connect. The accelerometer sensor data was collected at a 25-Hz frequency, while other sensors were recorded at a 1-Hz frequency, which are the default frequencies within the RawLogger application. All sensor data was exported as a Garmin FIT file and

subsequently converted into a **.csv* file. Only the watch accelerometer data, collected at 25 Hz and recorded in thousandths of a gravity (mgn), was used in model development.

Table 5.1. Summary of productive cycle elements for choker setter and chaser work activities.

Position	**Activity**	**Activity begins when subject:**
Choker setter	Travel to log	Initiates walking toward carriage to acquire chokers
	Set choker	Arrives at log
	Travel away	Finishes setting choker
	Clear	Stops walking away when safely "in the clear"
Chaser	Travel to log	Initiates walking toward the landed logs
	Unhook	Reaches for the chokers to begin unhooking
	Travel away	Finishes unhooking chokers
	Clear	Stops walking away when safely "in the clear"

All data processing, analysis and model development was done in the R statistical programming environment, version 4.0.0 [96]. After data collection, all observations in the datasets were labeled according to the manually recorded start and stop times. Specifically, each observation whose timestamp fell within the start and stop time for a particular activity cycle was assigned a label for that activity element (i.e., *travel to log*, *set choker*, *travel away*, *clear*, etc.). Delay times were included as the corresponding productive work element because the majority of delays fell within *clear*, included a diverse range of physical movements associated with the workers, and because of the intended final use of a general model in continuous, real-time prediction. After labeling, the raw acceleration values (in the x, y, and z dimensions) were filtered using a Finite Impulse Response (FIR) bandpass filter of order 8. Filter band edges were 0.5 and 0.9. Rather than using the x, y, and z values of the acceleration sensor, the acceleration magnitude was calculated using Eq (1) and used in an effort to reduce the effects of orientation on recognition performance:

$$A_{mag} = \sqrt{A_x^2 + A_y^2 + A_z^2} \tag{1}$$

Where A_{mag} is the filtered overall acceleration magnitude, and A_x, A_y, and A_z are the filtered acceleration sensor values in the x, y, and z dimensions, respectively.

5.3.3 Activity recognition model development

Ten time domain features (mean, standard deviation, maximum, minimum, median absolute deviation, mean absolute deviation, skewness, interquartile range, range, and kurtosis) were extracted

from the filtered acceleration magnitude values from both the choker setter and chaser work activity data using 15 different sizes of sliding windows (ranging from 1 to 15 s). For example, using a 3-s window and data recorded at 25 Hz, features were calculated using the previous 75 observations (representing 3 s of data) each time the window was advanced. Windows with 0%, 25%, 50%, 75%, and 90% overlap were used, resulting in five feature extraction methods for each window size. For instance, using 25% overlap meant that the next window did not begin until the current window was 75% complete. After filtering and applying sliding windows, the resulting datasets were separated into 2/3 training and 1/3 testing data. Data was separated randomly, but the relative ratios of each activity were preserved because the data was highly imbalanced. The randomForest function in the R randomForest package (version 4.6-14) [97] was used to create random forest models to predict the four work cycle elements of both the choker setter and chaser based on the sensor measurements (Figure 5.2). Because the data was imbalanced, models were created using stratified sampling according to activity, with sample size based on the number of instances of the least common activity. In terms of the choker setter models, the least common activity was *travel away*. The least common chaser activity was *travel to log*. Random forest models can be tuned via a variety of parameters, such as the number of trees to grow (n_{tree}) and the number of predictor variables randomly selected at each node (m_{try}) [97,98]. In this study, random forest models were created using 150 trees, since previous work has suggested that using 64–128 trees is appropriate for balancing performance and processing time [99]. Because varying m_{try} generally does not have a significant effect on model performance [97,100], models in this study were built with the default value of m_{try} (the square root of the total number of variables). The relationship between the number of trees and model accuracy was evaluated using the out-of-bag (OOB) sample error rates calculated internally by the random forest algorithm.

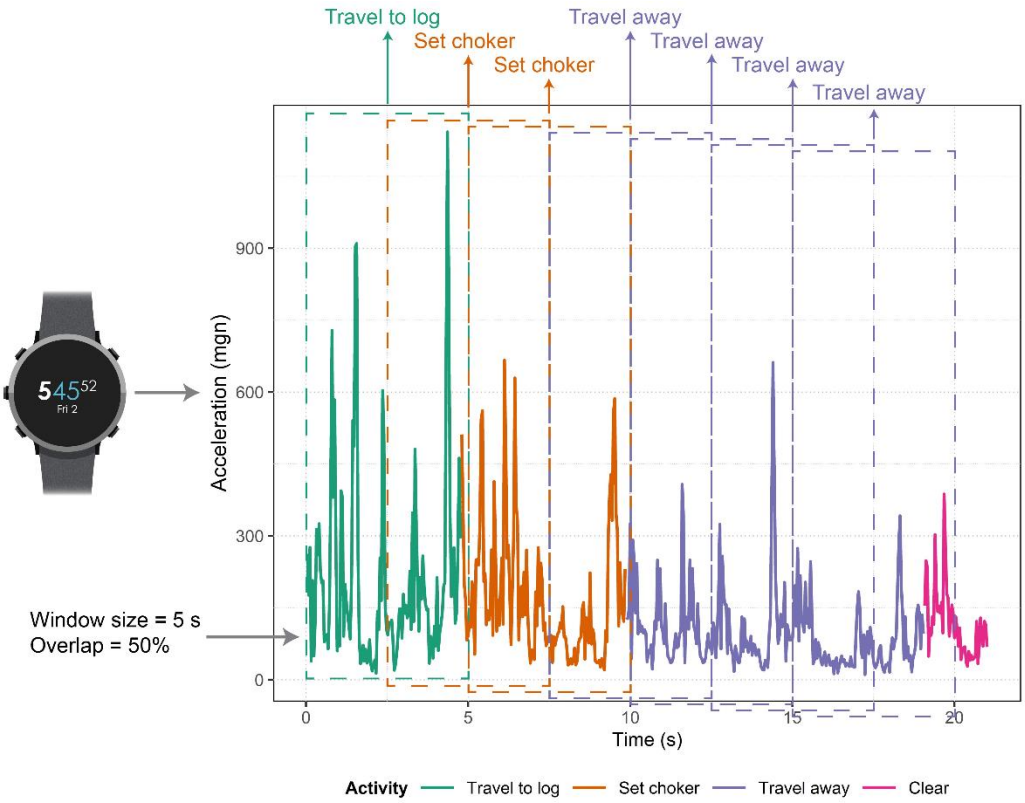

Figure 5.2. Overview of a hypothetical choker setter activity recognition model running on a smartwatch. The activity recognition model depicted is using a 5-s window with 50% overlap to predict the four work activities. The figure shows filtered acceleration magnitude data, which is colored according to the actual work cycles. Each time a window (shown as rectangles with dashed lines) is used to extract features, the model predicts the work cycle (shown as labels above the windows).

Initially, choker setter and chaser models were created for the 15 window sizes using 90% overlap and all ten features, but model accuracy was poor. Thus, principal component analysis (PCA) was used to reduce the number of features in the models. The same ten time domain features described above were calculated for each activity cycle for both the choker setter and chaser datasets using the filtered acceleration magnitude values. PCA was performed on these ten features for both the choker setter and chaser datasets. Principal components (PCs) that accounted for > 95% of the variation in each dataset were considered and individual variables with loadings > |0.4| within these PCs were used as predictors in the final models.

After selecting model predictors, a total of 75 choker setter models and 75 chaser models were created using the 15 window sizes for each of the five levels of overlap. Models were created using the training datasets and the confusionMatrix function in the R caret package (version 6.0-85)

[101] was used to calculate a variety of model accuracy metrics based on the testing datasets. All models were initially evaluated using sensitivity, specificity, and precision to compare the effects of overlap levels and window sizes. Sensitivity, specificity, and precision were calculated using Eqs (2–4):

$$Se = \frac{TP}{TP + FN} \tag{2}$$

$$Sp = \frac{TN}{TN + FP} \tag{3}$$

$$Pr = \frac{TP}{TP + FP} \tag{4}$$

Where *Se* is the sensitivity, *Sp* is the specificity, and *Pr* is the precision. *TP* is the number of true positives (i.e., the number of correctly classified instances of a given class), *TN* is the number of true negatives (i.e., for a given class, the number of instances of all other classes that are classified as anything other than the class of interest), *FP* is the number of false positives (i.e., the number of instances that are incorrectly classified as belonging to a given class), and *FN* is the number of false negatives (i.e., the number of instances of a given class that are incorrectly classified as a different class). Sensitivity, specificity, and precision were then converted to and reported as percentages. Sensitivity, or recall, is the true positive rate and represents the percentage of correctly identified activities of a particular class [102]. Specificity is the true negative rate and measures the percentage of correctly detected negative occurrences of a particular class [102]. Precision, or positive predictive value, measures the percentage of detected instances of an activity that represents a real occurrence [102]. Finally, the multiclass area under the Receiver Operating Characteristic (ROC) curve, or AUC, was calculated for each model. The AUC corresponds to the probability that a classifier will rank a randomly chosen positive instance higher than a randomly chosen negative instance, with higher AUC values indicating better performance [103]. AUC is a common criterion for evaluating the performance of classification algorithms [104,105]. It has also been shown to be relatively robust to data imbalance [106–108]. The multiclass.roc function in the R pROC package (version 1.16.2) [109] was used to compute the multiclass AUC according to the method defined by Hand and Till [110]. The multiclass AUC value was then used to compare models and choose the best window size and overlap level for the choker setter and chaser models. Final models were evaluated based on the three metrics described previously (sensitivity, specificity, and precision) as well as F_1 values and balanced accuracy. F_1 values and balanced accuracy were calculated using Eqs (5–6):

$$F_1 = \frac{2 * Pr * Se}{Pr + Se} \quad (5)$$

$$BA = \frac{Se + Sp}{2} \quad (6)$$

Where F_1 is the F_1 value and *BA* is the balanced accuracy. *Pr* is the precision, *Se* is the sensitivity, and *Sp* is the specificity. The F_1 value represents the harmonic mean of precision and recall (sensitivity) and is generally thought to be more robust when dealing with imbalanced classes [51]. It ranges from zero to one, with zero representing no capacity for recognition and one corresponding to perfect recognition [51]. The F_1 value was calculated using the rate of precision and sensitivity (rather than the percent). Balanced accuracy is simply the mean of sensitivity and specificity and was calculated using the percentage values of these two metrics.

5.4 Results

5.4.1 Work activity cycle times

For the choker setter work activities, *travel to log* averaged 17.27 s (s = 12.30 s), *set choker* averaged 19.80 s (s = 16.06 s), *travel away* averaged 13.11 s (s = 6.83 s), and *clear* averaged 220.31 s (s = 519.17 s) (Table 5.2). For the chaser work activities, *travel to log* averaged 4.59 s (s = 4.42 s), *unhook* averaged 8.00 s (s = 6.42 s), *travel away* averaged 6.69 s (s = 3.73 s), and *clear* averaged 264.48 s (s = 481.49 s) (Table 5.2). Mean work activity cycle times for the chaser were generally shorter than the mean cycle times for the choker setter, and the maximum cycle times tended to be slightly longer for the choker setter activities compared to the chaser activities (Table 5.2). When expressed as a percentage of the mean elemental time for individual work cycles other than *clear*, the coefficient of variation (CV) ranged from 52.11% to 81.09% for the choker setter and from 55.70% to 96.28% for the chaser (Table 5.2). *Clear* was the only element for which the CV > 100% for both the choker setter and chaser (Table 5.2).

Table 5.2. Summary statistics (in seconds) of cycle times for choker setter and chaser work activities.

Position	Activity	Mean (s)	SD (s)	CV (%)	Range (s)	Median (s)	1st Quartile (s)	3rd Quartile (s)
Choker setter	Travel to log	17.27	12.30	71.23	0.72-105.56	13.96	9.06	21.82
	Set choker	19.80	16.06	81.09	1.14-188.21	14.73	9.46	24.61
	Travel away	13.11	6.83	52.11	2.5-55.74	11.87	8.74	15.44
	Clear	220.31	519.17	235.65	5.7-8441.34	120.22	93.55	166.14
Chaser	Travel to log	4.59	4.42	96.28	0.54-89.92	3.85	2.74	5.49
	Unhook	8.00	6.42	80.31	0.86-71.58	6.52	4.17	10.07
	Travel away	6.69	3.73	55.70	1.19-26.14	5.61	3.95	8.85
	Clear	264.48	481.49	182.06	4.93-8238.2	174.55	144.49	229.41

5.4.2 Participant data

Due to the observational nature of data collection, the amount of data used to train and test the random forest models varied between participants. The average amount of data per choker setter ranged from 0.80 hrs (s = 0.01 hrs) to 6.74 hrs (s = 0.05 hrs) for training and from 0.40 hrs (s = 0.01 hrs) to 3.31 hrs (s = 0.05 hrs) for testing. The average amount of data per chaser ranged from 0.80 hrs (s = 0.02 hrs) to 4.59 hrs (s = 0.04 hrs) for training and from 0.39 hrs (s = 0.02 hrs) to 2.26 hrs (s = 0.04 hrs) for testing. When expressed as a percentage of the mean training and testing sample times for individual choker setters, the standard deviation ranged from 0.69% to 1.65% of the training sample times and from 1.39% to 3.34% of the testing sample times. Similarly, for individual chasers, the standard deviation ranged from 0.93% to 2.04% of the training sample times and from 1.90% to 4.10% of the testing sample times.

5.4.3 Principal component analysis

In terms of the choker setter, the first PC accounted for 98.13% of the variation in the dataset and the only variables with loadings > |0.4| in the first PC were the acceleration maximum and range (Table 5.3). Similarly, in terms of the chaser, the first PC accounted for 97.92% of the variation in the dataset and the only variables with loadings > |0.4| in the first PC were the acceleration maximum and range (Table 5.3). Thus, acceleration maximum and range were selected as predictors in the final models for both workers. Biplots of the first two PCs for both the choker setter and chaser datasets illustrate the strong effect of acceleration maximum and range on the two datasets (Figure 5.3).

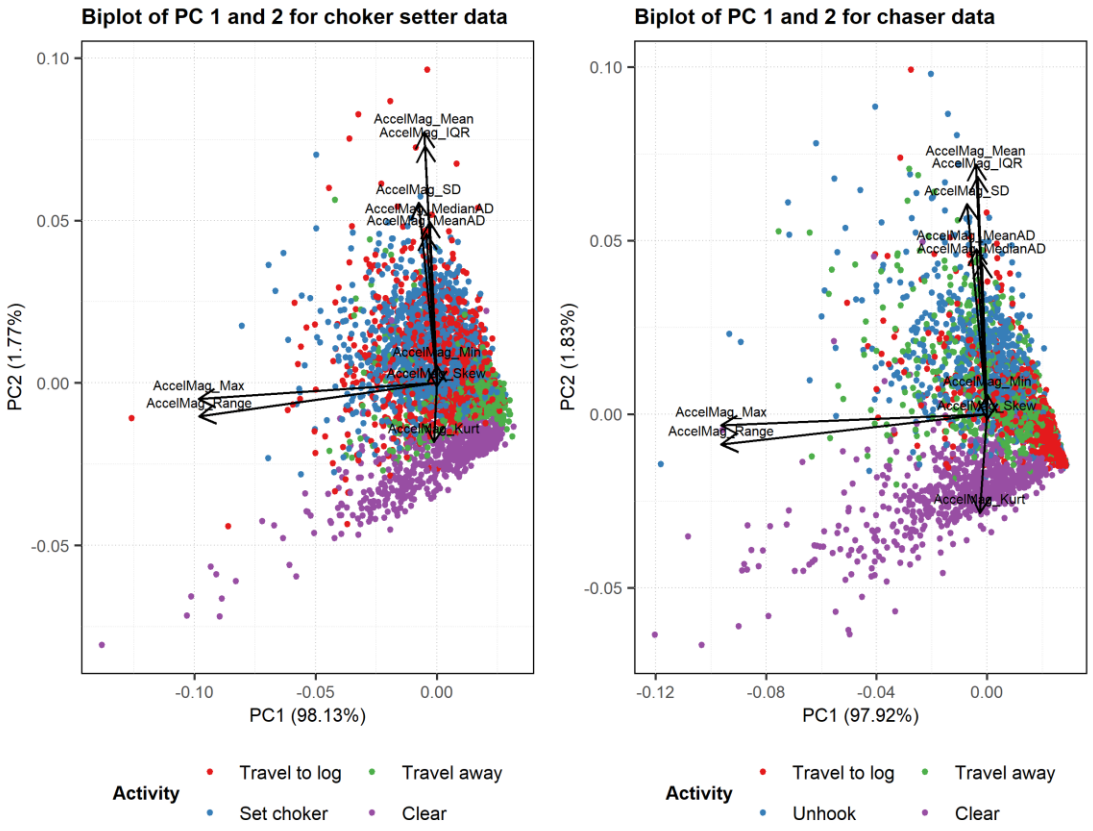

Figure 5.3. Biplots of PCs 1 and 2 for the choker setter and chaser datasets. The color of points on each plot indicates work cycle element categories.

Table 5.3. Summary of choker setter and chaser PCA results.

	Position	**Choker setter**				**Chaser**			
	PC	**PC1**	**PC2**	**PC3**	**PC4**	**PC1**	**PC2**	**PC3**	**PC4**
	Percent of Variance	***98.13%***	***1.77%***	***0.05%***	***0.03%***	***97.92%***	***1.83%***	***0.14%***	***0.08%***
Variable	Mean	-0.038	**0.554**	0.235	-0.303	-0.030	**0.527**	-0.221	0.029
	Standard deviation	-0.054	0.398	**-0.686**	-0.353	-0.053	**0.443**	0.395	**-0.624**
	Maximum	**-0.705**	-0.036	0.056	-0.062	**-0.705**	-0.024	-0.014	0.028
	Minimum	0.000	0.039	0.092	-0.158	0.000	0.041	-0.042	-0.002
	Median absolute deviation	-0.021	0.356	0.354	0.163	-0.014	0.321	-0.299	0.285
	Mean absolute deviation	-0.031	0.329	-0.264	-0.063	-0.028	0.349	0.125	-0.278
	Skewness	-0.001	-0.009	0.010	-0.036	-0.001	-0.011	-0.020	-0.022
	Interquartile range	-0.035	**0.524**	0.296	0.345	-0.025	**0.501**	-0.323	0.284
	Kurtosis	-0.009	-0.131	**0.422**	**-0.771**	-0.020	-0.208	**-0.763**	**-0.607**
	Range	**-0.705**	-0.074	-0.036	0.096	**-0.705**	-0.064	0.028	0.030

The percentages of variance for the first four PCs as well as the individual loadings for each variable for the first four PCs are shown. Numbers in **bold** indicate variables with loadings > |0.4|.

5.4.4 Number of trees

At the 90% overlap level, the classification accuracies determined internally by the random forest algorithm for both the choker setter and chaser models leveled off after 25–50 trees for most window sizes (Figure 5.4), and similar trends were observed for the other overlap levels (not shown). This suggests that building our models with 150 trees was sufficient.

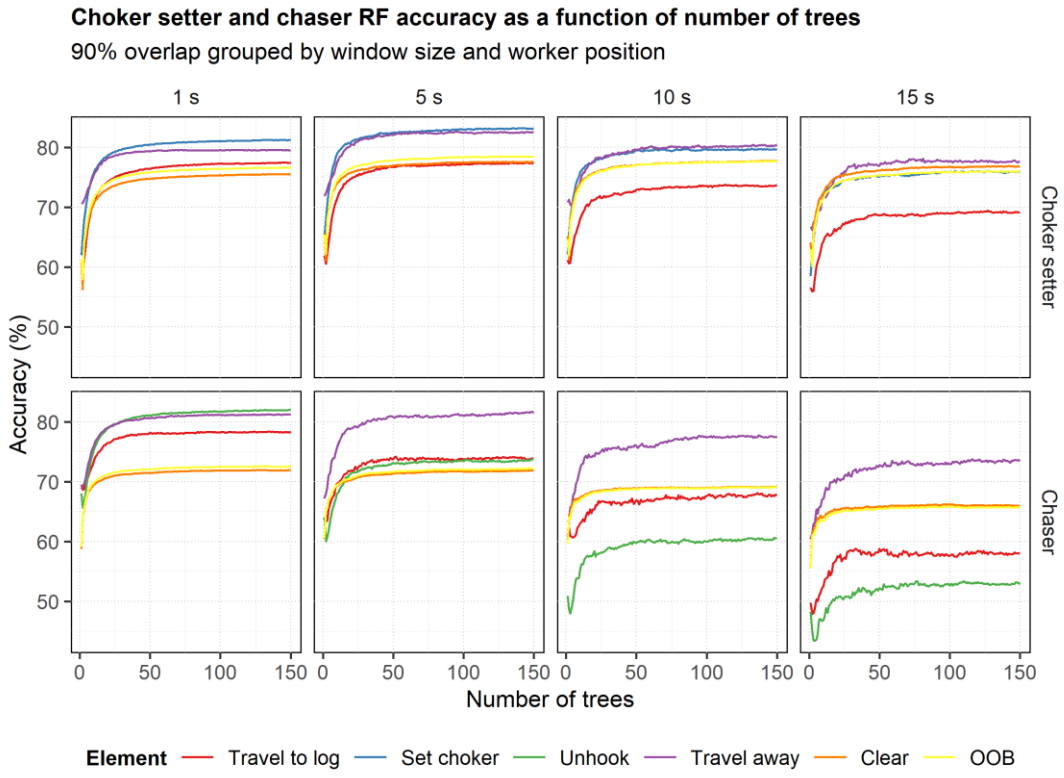

Figure 5.4. Choker setter and chaser random forest model accuracy as a function of the number of trees. The plots are grouped by worker type (choker setter or chaser) and window size. Line color indicates overall model (OOB) accuracy as well as accuracy for the work cycle elements. Only the 90% overlap of the 1-, 5-, 10- and 15-s windows are shown.

5.4.5 Choker setter models

The sensitivity, specificity, and precision of the choker setter models were highest when using sliding windows with 90% overlap for all activities and window sizes (Figure 5.5). Using sliding windows with 75% overlap resulted in the second-highest values of these same metrics for all

activities and window sizes (Figure 5.5). The remaining overlap levels (50%, 25%, and 0%) resulted in the lowest values of these metrics (Figure 5.5). Finally, sensitivity, specificity, and precision generally did not vary noticeably between window sizes for most activities (Figure 5.5).

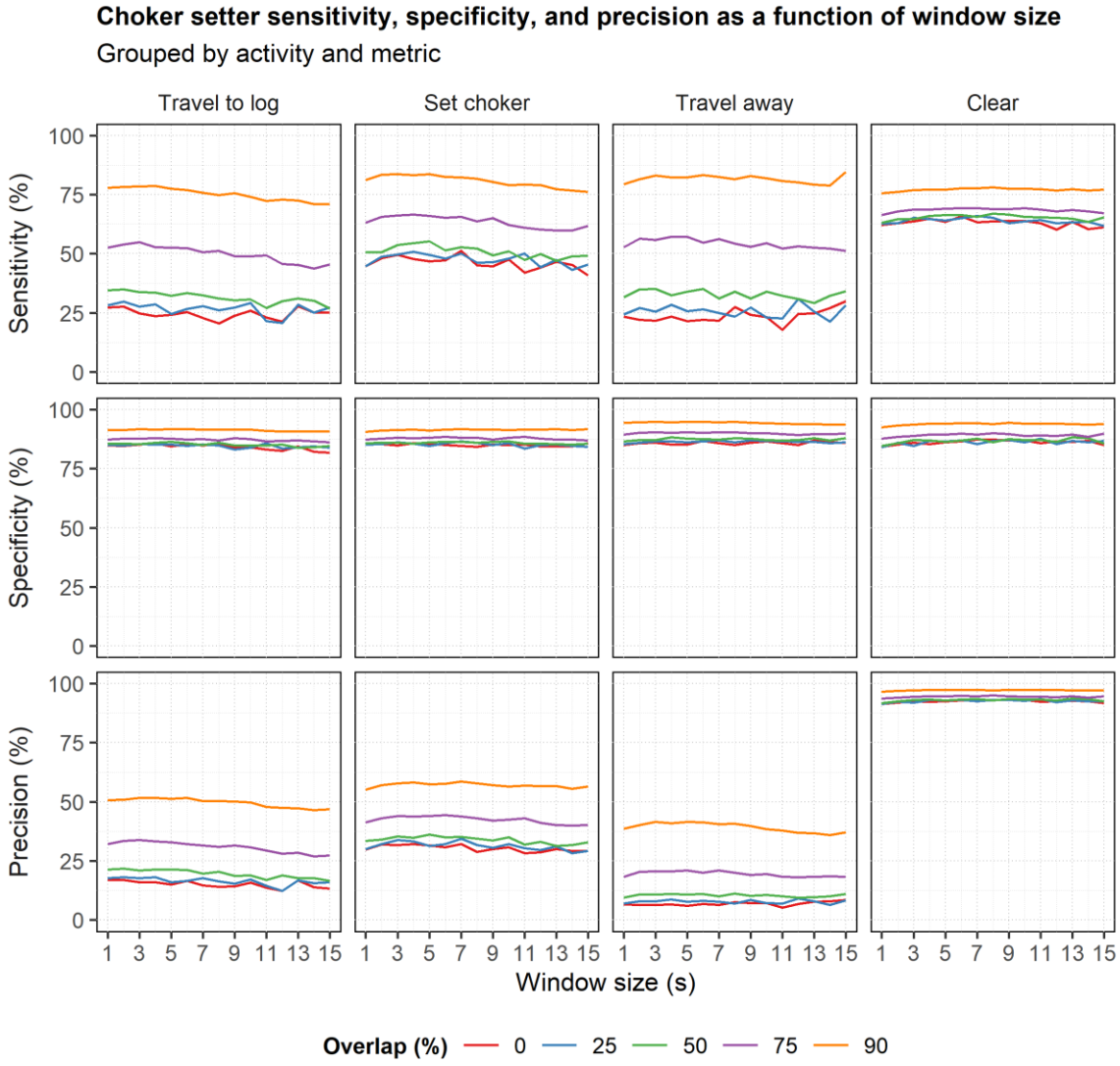

Figure 5.5. Choker setter sensitivity, specificity, and precision as a function of window size. The plots are grouped by metric and work activity. Line color indicates window overlap level.

5.4.6 Chaser models

The sensitivity, specificity, and precision of the chaser models were highest when using sliding windows with 90% overlap for all activities and window sizes (Figure 5.6). Using sliding windows with 75% overlap resulted in the second-highest values of these same metrics for many

activities and window sizes (Figure 5.6). The remaining overlap levels (50%, 25%, and 0%) generally resulted in the lowest values of these metrics Figure 5.6). Additionally, sensitivity tended to decrease as window size increased for most activities (Figure 5.6, first row) while specificity decreased slightly with increasing window size for the *travel to log* activity but did not show much variation with window size for the other three activities (Figure 5.6, second row). Precision decreased with increasing window size for the *travel to log* and *unhook* activities at the higher overlap levels but did not vary as noticeably for the *travel away* and *clear* activities (Figure 5.6, third row).

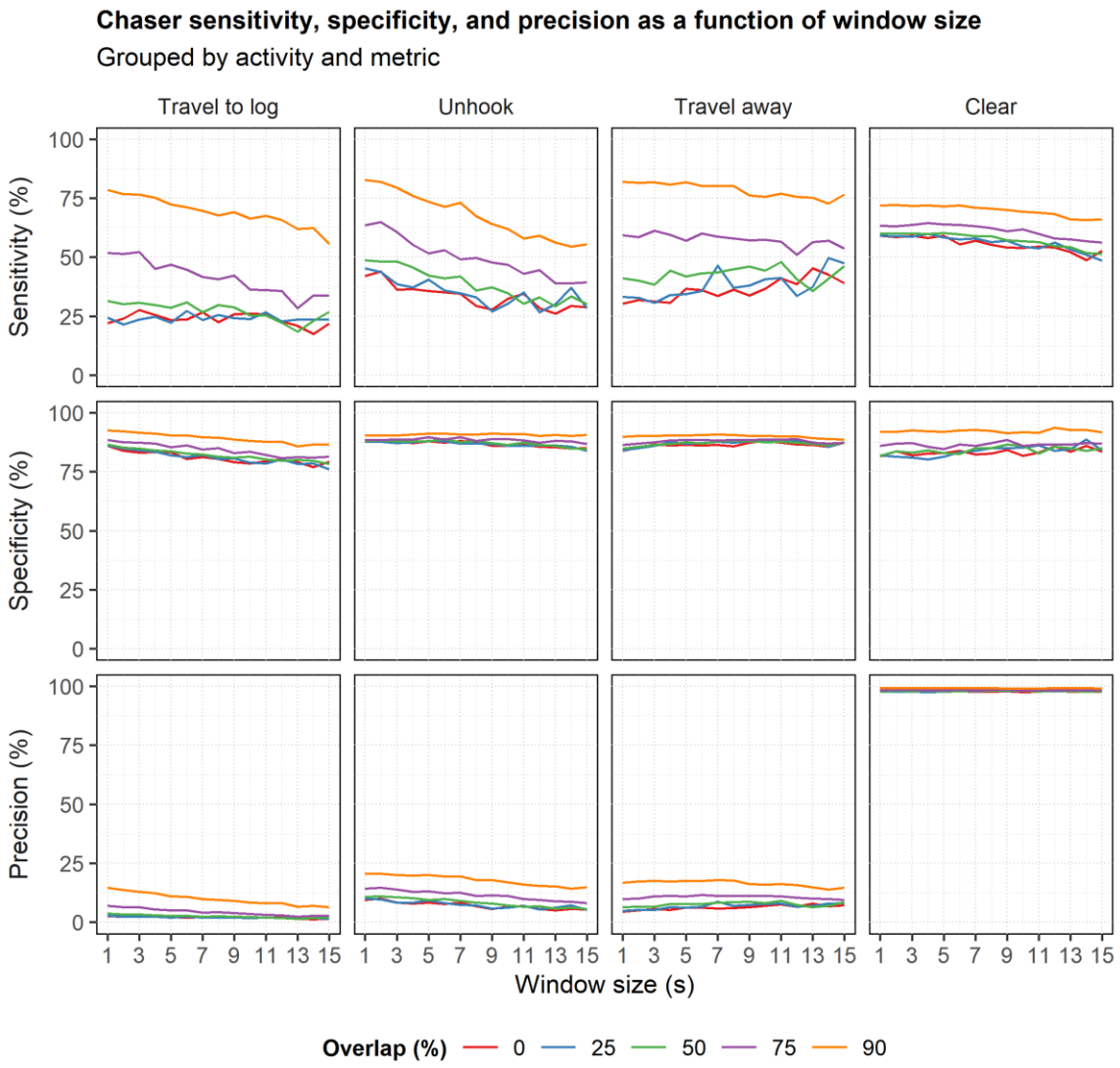

Figure 5.6. Chaser sensitivity, specificity, and precision as a function of window size. The plots are grouped by metric and work activity. Line color indicates window overlap level.

5.4.7 Model selection

The multiclass AUC plot indicates that the 90% overlap level resulted in the highest AUC values across all window sizes for both the choker setter and chaser models (Figure 5.7). AUC did not vary much with window size for the choker setter models (Figure 5.7, top row). For the chaser models, AUC decreased with increasing window size for the 90% and 75% overlap levels but varied less with window size for the other overlap levels (Figure 5.7, bottom row). A 3-s window with 90% overlap had the highest AUC (94.42%) for the choker setter models (Figure 5.7, top row) and a 1-s window with 90% overlap had the highest AUC (93.62%) for the chaser models (Figure 5.7, bottom row). Thus, these two models were chosen as the optimal choker setter and chaser models.

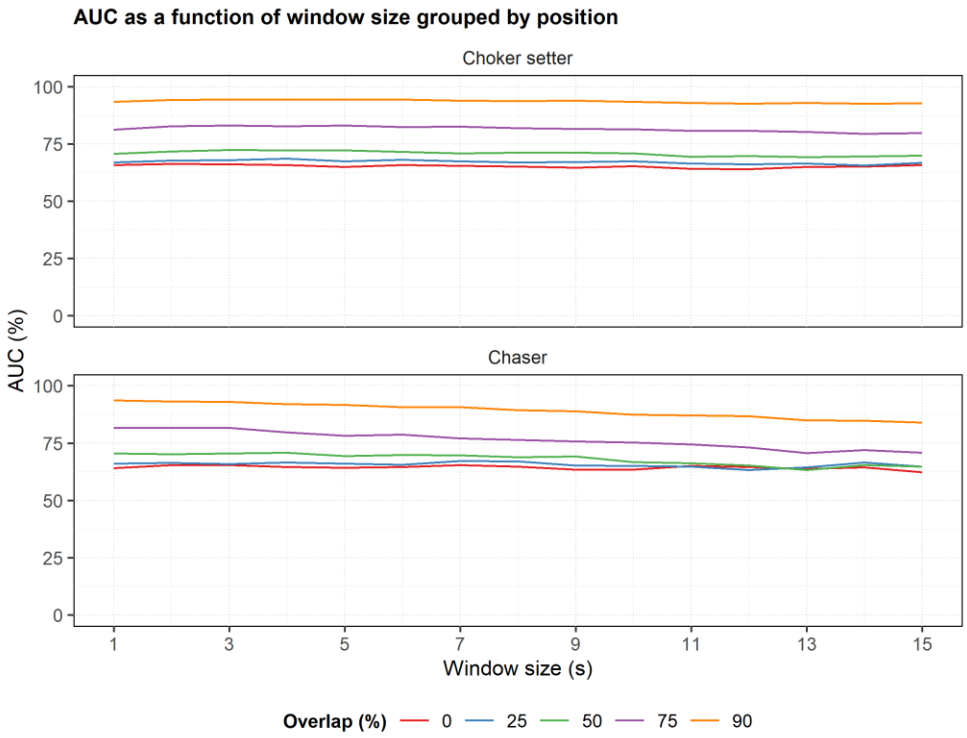

Figure 5.7. Choker setter and chaser multiclass AUC as a function of window size. The plots are grouped by worker type (choker setter or chaser). Line color indicates window overlap level.

Sensitivity for the selected choker setter model (3-s window, 90% overlap) ranged from 76.95% to 83.59% for the four activities (Table 5.4). Precision for this model ranged from 41.42% to 97.08% for the four activities, specificity ranged from 91.36% to 94.73%, F_1 values ranged from 0.55 to 0.86, and balanced accuracy ranged from 85.02% to 88.90% (Table 5.4). The confusion matrix for the selected choker setter model (3-s window, 90% overlap) illustrates that the *set choker* activity was

most often confused with *travel to log* (Table 5.5). *Travel away* was somewhat equally confused with the other three activities (*set choker*, *travel to log*, and *clear*), while *travel to log* was most often confused with either *set choker* or *clear* (Table 5.5). Finally, *clear* was most often confused with either *set choker* or *travel to log* (Table 5.5).

Table 5.4. Accuracy metrics for the best choker setter model (created with a 3-s window and 90% overlap).

Activity	**Sensitivity (%)**	**Precision (%)**	**Specificity (%)**	**F_1**	**Balanced Accuracy (%)**
Travel to log	78.42	51.68	91.63	0.62	85.02
Set choker	83.59	57.82	91.36	0.68	87.48
Travel away	83.06	41.42	94.73	0.55	88.90
Clear	76.95	97.08	93.72	0.86	85.33

Table 5.5. Confusion matrix for the best choker setter model (created with a 3-s window and 90% overlap).

		Actual			
		Set choker	**Travel away**	**Travel to log**	**Clear**
Predicted	**Set choker**	18655	455	1898	11254
	Travel away	888	6409	554	7622
	Travel to log	1743	365	14455	11407
	Clear	1031	487	1526	101095

Sensitivity for the selected chaser model (1-s window, 90% overlap) ranged from 71.95% to 82.75% for the four activities (Table 5.6). Precision for this model ranged from 14.74% to 99.16% for the four activities, specificity ranged from 89.76% to 92.43%, F_1 values ranged from 0.25 to 0.83, and balanced accuracy ranged from 81.97% to 86.54% (Table 5.6). The confusion matrix for the selected chaser model (1-s window, 90% overlap) shows that *clear* was most often confused with *travel away* but was also frequently mistaken for *unhook* (Table 5.7). *Travel away* was most often confused with either *unhook* or *clear*, while *travel to log* was most often mistaken for *clear* (Table 5.7). Finally, *unhook* was most often confused with either *clear* or *travel away* (Table 5.7).

Table 5.6. Accuracy metrics for the best chaser model (created with a 1-s window and 90% overlap).

Activity	**Sensitivity (%)**	**Precision (%)**	**Specificity (%)**	**F_1**	**Balanced Accuracy (%)**
Travel to log	78.53	14.74	92.43	0.25	85.48
Unhook	82.75	20.66	90.34	0.33	86.54

Travel away	81.93	16.75	89.76	0.28	85.84
Clear	71.95	99.16	91.99	0.83	81.97

Table 5.7. Confusion matrix for the best chaser model (created with a 1-s window and 90% overlap).

		Actual			
		Clear	**Travel away**	**Travel to log**	**Unhook**
Predicted	**Clear**	366814	972	1022	1099
	Travel away	53458	11028	372	978
	Travel to log	39715	409	7061	714
	Unhook	49828	1052	536	13385

5.5 Discussion

Our results show that activity recognition models based on smartwatch accelerometers can characterize work activities for rigging crew workers setting and disconnecting log chokers on cable logging operations, with the best model sensitivities ranging from 76.95% to 83.59% for choker setters and from 71.95% to 82.75% for chasers. While not all activities met our objective of 80% sensitivity, these values are consistent with models based on smartwatches and wrist-worn accelerometers developed for other activities in previous studies [27,29,32,33,35,54–56]. The benchmark of 80% sensitivity was established ahead of time as part of project development. While we recognize that a combination of metrics may be more suitable for future use, particularly when dealing with imbalanced datasets, this was a pilot study intended to help establish methods prior to a larger modeling effort.

In contrast to the fairly high sensitivity values, precision was poor for most activities for both the choker setter and chaser models. This may be due to the imbalanced nature of the data. The proportions of choker setter activities were 10.26% *travel to log*, 12.41% *set choker*, 4.29% *travel away*, and 73.04% *clear*. The proportions of chaser activities were 1.64% *travel to log*, 2.95% *unhook*, 2.45% *travel away*, and 92.95% *clear*. Furthermore, the high CV values in Table 5.2 suggest there was high variability within individual work cycle elements, especially within the *clear* activity for both the choker setters (CV = 235.65%) and chasers (CV = 182.06%), which likely resulted at least in part from the inclusion of delay time in work elements. Additional variability may have been introduced to the *clear* activity due to the fact that *clear* encompassed everything workers did outside of the other three work elements. The combination of this variability with the large proportion of time workers spent in the clear likely reduced prediction accuracy and could account for the generally low

precision and F_1 values. Since this form of analysis is very new in natural resources work, there is relatively little prior research on how delay, misclassified activities, or low precision in general may impact real-time summaries of work, or worker health and safety considerations, when interpreted in practice. Rather than a shortcoming of our study, we feel this is an important consideration for subsequent research and for development of wearable-based digital health and safety analytics for operational forestry. Additionally, conventional time study analysis distinguishes between quantifying individual productive cycle elements and quantifying overall productive and delay components of occupational work. Future modeling studies may benefit from distinguishing sampling efforts to quantify these separately. This may influence the way in which low precision and high false positive rates affect metrics such as productivity that may be calculated from model predictions in real-time. Thus, future work should consider how *clear* is defined and whether delay times are included in sampling and developed models in an effort to improve precision. Future work should also address issues of low precision through improved data collection, processing, and modeling (e.g., utilizing video recording, faster sampling rates, different sensors, deep learning, additional features, etc.), all of which are discussed below.

The best model performance metrics for both workers were obtained using the highest level of window overlap (90%) and smaller window sizes. The increasing accuracy we obtained with higher levels of window overlap is consistent with previous work [45]. However, many wrist-based models developed with either no overlap [27,29,56] or 50% overlap [54,55] have achieved high accuracies. In terms of window size, previous work has suggested that simpler, more repetitive activities may be accurately captured with shorter windows, while more complex, less repetitive activities may need longer windows [34,55]. In general, we observed slightly decreasing performance metrics with increasing window size. While some previous studies have found improved accuracies with increasing window size [34,56], others have observed that increasing window size did not result in significant model improvement [55] and have developed accurate wrist-based models using smaller window sizes [35,54,55].

Smartwatches, smartphones, and other wearables generally have limited resources in terms of battery power, memory, storage, and computational power, so the effects of window size, window overlap, and sampling rate must be considered when designing and implementing occupational activity recognition models [31,42,111,112]. For instance, using longer windows [45,111], higher levels of window overlap [45], and faster sampling rates [31,42] requires more computational resources during implementation. In our study, the difference between the 90% and 75% overlap

levels was noticeable for many of the model accuracy metrics. While lower levels of overlap may be preferable for real-time implementation on resource-limited devices such as smartwatches, the improved accuracies observed with the higher overlap levels seem to justify the additional computational power needed. On the other hand, our results suggest that the highest accuracies for both the choker setter and chaser models can be obtained with smaller window sizes, which indicates real-time implementation may be achieved with relatively minimal computational complexity and fast detection rates. Finally, future work should evaluate the effects of different sampling rates. While previous work has shown that higher frequencies can lead to improved accuracies [42,111], others have achieved high performance using lower sampling rates such as 2-Hz [111] and 10-Hz [30]. The RawLogger application used to record the watch sensor data in this study did not allow us to adjust the sampling frequency, and Garmin Connect allows a maximum rate of 25-Hz for the accelerometer. However, different devices could be used in future work to assess whether higher frequencies may improve performance and whether lower sampling frequency may achieve similar performance, as this would have the benefit of reducing power consumption on the device.

Other considerations related to performance and resource consumption on wearable devices are the types of features used for classification and the tradeoffs between classical machine learning and deep learning methods. We chose to use time domain features primarily because they are less computationally complex and consume less energy during implementation [42,113]. Additionally, it has been shown that the use of frequency domain features should be paired with faster sampling rates in order to achieve high model performance [42]. However, the use of frequency domain features should be investigated as a potential method of improving model performance [114]. Similarly, we chose to use a traditional machine learning approach because deep learning methods are generally more computationally expensive [47]. As devices become more powerful, deep learning offers opportunities to overcome some of the limitations of classical machine learning [48–50].

Activity recognition models based on wearables such as smartphones and smartwatches have practical applications for quantifying productivity and reporting work analytics to support digital health and safety. In terms of rigging crew productivity, models may inform the real-time reporting of productive work elements such as mean time per turn, number of chokers set or disconnected per turn, and related analytics. Models developed using conventional time studies in forestry have been limited to very specific operations and time periods under consideration, or deployed broadly in generalized predictive models (e.g., Bell et al. [115]). Utilizing our activity recognition models and subsequent, improved models using similar approaches makes it possible to quantify work day-in,

day-out over the course of the work week and indefinitely in the future when incorporated into predictive apps on smartwatches. This is a major advancement and opens new possibilities for analysis of big data accumulated over time. For example, when summarized at the individual and group level, this information could be used to improve productivity, reduce costs, and enhance work quality and worker safety by allowing workers to adapt treatment methods in near real-time. Furthermore, in broader meta-analysis, use of wearables to quantify productivity with greater temporal resolution than traditional time study techniques may provide opportunities for improving estimates of work productivity and treatment costs across various stand and site conditions and spatial scales. To better quantify worker health and safety, activity recognition model predictions may be paired simultaneously with fall detection algorithms to inform smart alerts indicating lack of movement associated with potential incidents. These alerts may then be sent to coworkers at the jobsite using emerging technologies designed to facilitate communication and data-sharing to improve safety in remote work areas. Model predictions may also be combined with other health-related data, such as heart rate, heat stress, and sleep metrics, to develop alerts that would be triggered when demanding work activities occur in conjunction with high physical exertion levels, increased heat stress, excess workload, or a combination of these factors. Finally, pairing activity recognition model predictions with real-time location information may be used to inform safety alerts related to proximity to coworkers, jobsite hazards such as snags or falling trees, and heavy equipment. This information could also be used in post-hoc analyses to better characterize the activities and other location- and health-related factors preceding accidents and near miss events.

One limitation to our study was reduced visibility when observing workers. Choker setters commonly work on steep hillsides, often among shrubs and other vegetation. At times, this made it difficult to visually observe start and stop times for component work cycle elements with precision. Chasers working at the landing were occasionally difficult to see when the yarder's movement shielded the chaser from view. A related limitation was a slight difference between the internal clocks of the smartwatches and the phones used to record the start and stop times for each activity. While these differences were small, there was no practical way to correct them in the field as they occasionally shift within a 24-hour period. This introduced additional error when assigning labels to the watch sensor data and is an important consideration in future remote occupational digital health applications, particularly for mobile and wearable devices that sync National Institute of Standards and Technology (NIST) time via internet connectivity.

Another limitation to the study was the short duration of many of the work activity cycles, primarily for the chaser. The chaser often runs in to and away from the yarded logs (both of which may last only a few seconds), and unhooking can be very quick (i.e., 3–5 s). This makes it difficult to visually detect and record accurate start and stop times for the rapid cycle elements that result. While this may explain why the shorter window lengths generally resulted in higher accuracies, it also made the activities more difficult to capture and model. Development of subsequent wearable- and mobile-based activity recognition for occupational safety may benefit from use of video concurrently with smartwatch sensor data collection rather than direct visual observation, in order to improve work element detection and support model training. For example, use of body camera videography coupled with post-hoc analysis to quantify work elements for low visibility tasks in forestry may improve model development.

A few areas that should be considered in future research include evaluating additional sensors, utilizing devices on different body parts, and incorporating more mechanistic approaches to modeling. The Garmin watches used in this study were only capable of recording raw accelerometer data. However, the incorporation of gyroscope sensor measurements into model development in future studies could potentially help to strengthen predictive power. While previous research has indicated that watch accelerometers perform better than watch gyroscopes for activity recognition [29], others have found that using both accelerometers and gyroscopes increases accuracy for smartphone-based models [52] and watch-based models [32]. Additionally, previous studies have shown that hip-mounted accelerometers may recognize activities like running better than wrist-mounted accelerometers [27] and that using sensors in multiple positions, such as the wrist and pocket, can improve model performance [34]. Thus, future work should evaluate how placing devices on different body parts affects model predictions. For instance, it is possible that using sensors on the torso or feet may more accurately recognize the movements of choker setters and chasers as they travel to and from logs, while wrist-based sensors may be better suited to detecting activities that involve hand motions, like setting and disconnecting chokers. Another consideration when evaluating device locations is that previous research has shown that participants may prefer wrist-worn devices compared to hip-worn devices [116], which has implications for designing a relatively unobtrusive system for real-world adoption. Lastly, use of the random forest machine learning algorithm to model the occupational activities of rigging crew workers is highly empirical and doesn’t necessarily help to foster understanding of the underlying processes affecting work productivity and safety. In future studies, a more mechanistic approach to modeling work movements may better lend itself to identifying causal relationships associated with safety incidents and possible interventions.

Because logging operations are highly variable and our sampling was observational, the amount of data collected from each participant varied. We chose to randomly separate the entire dataset into 2/3 training and 1/3 testing since utilizing either leave-one-subject-out or k-fold cross-validation implemented at the participant level would have meant creating models with varying quantities of data in each iteration. Thus, because our validation methods may randomly include data from participants in both training and testing, the quality of predictive models presented may be overly optimistic. Future research developing similar models may benefit from a different approach that avoids cross-over of participant data in training and testing subsets. Additionally, traditional time and motion and actigraphy analysis in forestry work has generally been based on relatively small studies. Because use of IMU sensors to quantify work in real-time is relatively new, it is unknown whether the mean and variability of data in our study would be fully representative of the broad range of field sites, forest stand conditions, equipment, and weather impacts that affect worker movements in the profession overall. While we believe the quantity of data from each participant used to train and test the models was sufficient, future studies may benefit from collecting a more balanced sample of data from a wider variety of participants. Our goals in this study were to evaluate, at a broad level, the potential for wearable devices to model real-time occupational rigging crew work activities and to provide an example of the methods, modeling approaches, and sampling considerations that are important for developing libraries of generalized forestry work activity recognition models. Prior to use in occupational settings, predictions from real-time models developed, regardless of the statistical validation methodology used in model fitting and analysis, should be further evaluated using data collected independently as part of different field operations reflecting variability in site conditions, weather, workers, and other factors.

Ultimately, future work should include coding the best models developed in this study into a smartwatch application to support real-time characterization of work activities and further validate model predictions in a variety of conditions. Pairing of fall detection with activity recognition model predictions may help to inform development of improved smart alerts to coworkers notifying them of potential jobsite incidents, particularly when paired with real-time GNSS mapping in remote forestry work environments. To advance digital health and safety more broadly, the data resulting from our predictive models, as well as from models developed subsequently for other common forestry work tasks, may be used to quantify day-to-day occupational forestry job functions in high resolution. The resulting work effort data provide a fundamental mechanism through which it may be possible to better quantify factors associated with incident occurrence across forest stand, site, weather, air

quality, and other work conditions, particularly when paired with readily available, wearable-based personal health metrics such as sleep activity, heart rate, and heat stress.

5.6 References

1. Hartley DS, Han H-S. Effects of alternative silvicultural treatments on cable harvesting productivity and cost in western Washington. West J Appl For. 2007;22: 204–212. doi: 10.1093/wjaf/22.3.204
2. Huyler NK, LeDoux CB. Cycle-time equation for the Koller K300 cable yarder operating on steep slopes in the Northeast. Radnor, PA, USA: U.S. Department of Agriculture, Forest Service, Northeastern Forest Experiment Station; 1997 Mar. Report No.: Res. Pap. NE-705. doi: 10.2737/NE-RP-705
3. Kirk PM, Sullman MJM. Heart rate strain in cable hauler choker setters in New Zealand logging operations. Appl Ergon. 2001;32: 389–398. doi: 10.1016/S0003-6870(01)00003-5
4. Shaffer RM, Milburn JS. Injuries on feller-buncher/grapple skidder logging operations in the Southeastern United States. For Prod J. 1999;49: 24–26.
5. Bell JL. Changes in logging injury rates associated with use of feller-bunchers in West Virginia. J Safety Res. 2002;33: 463–471. doi: 10.1016/S0022-4375(02)00048-8
6. Lefort AJ Jr, de Hoop CF, Pine JC, Marx BD. Characteristics of injuries in the logging industry of Louisiana, USA: 1986 to 1998. Int J For Eng. 2003;14: 75–89. doi: 10.1080/14942119.2003.10702480
7. Scott DF. A study of logger fatalities from 1992–2000. Inj Prev. 2004;10: 239–243. doi: 10.1136/ip.2003.004663
8. Lagerstrom E, Magzamen S, Rosecrance J. A mixed-methods analysis of logging injuries in Montana and Idaho. Am J Ind Med. 2017;60: 1077–1087. doi: 10.1002/ajim.22759
9. U.S. Bureau of Labor Statistics. Fatal occupational injuries by occupation and event or exposure, all United States, 2017. 2018. Available from: https://www.bls.gov/iif/oshwc/cfoi/cftb0317.htm
10. U.S. Bureau of Labor Statistics. Fatal occupational injuries by occupation and event or exposure, all United States, 2018. 2019. Available from: https://www.bls.gov/iif/oshwc/cfoi/cftb0326.htm
11. Tsioras PA, Rottensteiner C, Stampfer K. Analysis of accidents during cable yarding operations in Austria 1998–2008. Croat J For Eng. 2011;32: 549–560.

12. Bordas RM, Davis GA, Hopkins BL, Thomas RE, Rummer RB. Documentation of hazards and safety perceptions for mechanized logging operations in East Central Alabama. J Agric Saf Health. 2001;7: 113–123. doi: 10.13031/2013.2673
13. Wempe AM, Keefe RF. Characterizing rigging crew proximity to hazards on cable logging operations using GNSS-RF: effect of GNSS positioning error on worker safety status. Forests. 2017;8: 357. doi: 10.3390/f8100357
14. Zimbelman EG, Keefe RF, Strand EK, Kolden CA, Wempe AM. Hazards in motion: Development of mobile geofences for use in logging safety. Sensors. 2017;17: 822. doi: 10.3390/s17040822
15. Newman SM, Keefe RF, Brooks RH, Ahonen EQ, Wempe AM. Human factors affecting logging injury incidents in Idaho and the potential for real-time location-sharing technology to improve safety. Safety. 2018;4: 43. doi: 10.3390/safety4040043
16. Zimbelman EG, Keefe RF. Real-time positioning in logging: Effects of forest stand characteristics, topography, and line-of-sight obstructions on GNSS-RF transponder accuracy and radio signal propagation. PLoS ONE. 2018;13: e0191017. doi: 10.1371/journal.pone.0191017
17. Wempe AM, Keefe RF, Newman SM, Paveglio TB. Intent to adopt location sharing for logging safety applications. Safety. 2019;5: 7. doi: 10.3390/safety5010007
18. Bao L, Intille SS. Activity recognition from user-annotated acceleration data. In: Ferscha A, Mattern F, editors. Proceedings of the Second International Conference on Pervasive Computing; 2004 Apr 21-23; Linz/Vienna, Austria. Springer, Berlin, Heidelberg; 2004. pp. 1–17. doi: 10.1007/978-3-540-24646-6_1
19. Mathie MJ, Celler BG, Lovell NH, Coster ACF. Classification of basic daily movements using a triaxial accelerometer. Med Biol Eng Comput. 2004;42: 679–687. doi: 10.1007/BF02347551
20. Wu W, Dasgupta S, Ramirez EE, Peterson C, Norman GJ. Classification accuracies of physical activities using smartphone motion sensors. J Med Internet Res. 2012;14: e130. doi: 10.2196/jmir.2208
21. Micucci D, Mobilio M, Napoletano P. UniMiB SHAR: a dataset for human activity recognition using acceleration data from smartphones. Appl Sci. 2017;7: 1101. doi: 10.3390/app7101101
22. Ermes M, Pärkkä J, Mäntyjärvi J, Korhonen I. Detection of daily activities and sports with wearable sensors in controlled and uncontrolled conditions. IEEE Trans Inf Technol Biomed. 2008;12: 20–26. doi: 10.1109/TITB.2007.899496

23. Mitchell E, Monaghan D, O'Connor NE. Classification of sporting activities using smartphone accelerometers. Sensors. 2013;13: 5317–5337. doi: 10.3390/s130405317
24. Stöggl T, Holst A, Jonasson A, Andersson E, Wunsch T, Norström C, et al. Automatic classification of the sub-techniques (gears) used in cross-country ski skating employing a mobile phone. Sensors. 2014;14: 20589–20601. doi: 10.3390/s141120589
25. Lane ND, Miluzzo E, Lu H, Peebles D, Choudhury T, Campbell AT. A survey of mobile phone sensing. IEEE Commun Mag. 2010;48: 140–150. doi: 10.1109/MCOM.2010.5560598
26. Kwapisz JR, Weiss GM, Moore SA. Activity recognition using cell phone accelerometers. ACM SIGKDD Explor Newsl. 2011;12: 74–82. doi: 10.1145/1964897.1964918
27. Trost SG, Zheng Y, Wong W-K. Machine learning for activity recognition: hip versus wrist data. Physiol Meas. 2014;35: 2183–2189. doi: 10.1088/0967-3334/35/11/2183
28. del Rosario MB, Redmond SJ, Lovell NH. Tracking the evolution of smartphone sensing for monitoring human movement. Sensors. 2015;15: 18901–18933. doi: 10.3390/s150818901
29. Weiss GM, Timko JL, Gallagher CM, Yoneda K, Schreiber AJ. Smartwatch-based activity recognition: A machine learning approach. Proceedings of the 2016 IEEE-EMBS International Conference on Biomedical and Health Informatics (BHI); 2016 Feb 24-27; Las Vegas, NV, USA. IEEE; 2016. pp. 426–429. doi: 10.1109/BHI.2016.7455925
30. Keefe RF, Zimbelman EG, Wempe AM. Use of smartphone sensors to quantify the productive cycle elements of hand fallers on industrial cable logging operations. Int J For Eng. 2019;30: 132–143. doi: 10.1080/14942119.2019.1572489
31. Shoaib M, Bosch S, Incel OD, Scholten H, Havinga PJM. A survey of online activity recognition using mobile phones. Sensors. 2015;15: 2059–2085. doi: 10.3390/s150102059
32. Mortazavi BJ, Pourhomayoun M, Alsheikh G, Alshurafa N, Lee SI, Sarrafzadeh M. Determining the single best axis for exercise repetition recognition and counting on smartwatches. Proceedings of the 2014 11th International Conference on Wearable and Implantable Body Sensor Networks; 2014 Jun 16-19; Zurich, Switzerland. IEEE; 2014. pp. 33–38. doi: 10.1109/BSN.2014.21
33. Moschetti A, Fiorini L, Esposito D, Dario P, Cavallo F. Recognition of daily gestures with wearable inertial rings and bracelets. Sensors. 2016;16: 1341. doi: 10.3390/s16081341
34. Shoaib M, Bosch S, Incel OD, Scholten H, Havinga PJM. Complex human activity recognition using smartphone and wrist-worn motion sensors. Sensors. 2016;16: 426. doi: 10.3390/s16040426

35. Cvetković B, Szeklicki R, Janko V, Lutomski P, Luštrek M. Real-time activity monitoring with a wristband and a smartphone. Inf Fusion. 2018;43: 77–93. doi: 10.1016/j.inffus.2017.05.004
36. Lara OD, Labrador MA. A survey on human activity recognition using wearable sensors. IEEE Commun Surv Tutor. 2013;15: 1192–1209. doi: 10.1109/SURV.2012.110112.00192
37. Saha J, Chowdhury C, Roy Chowdhury I, Biswas S, Aslam N. An ensemble of condition based classifiers for device independent detailed human activity recognition using smartphones. Information. 2018;9: 94. doi: 10.3390/info9040094
38. Chen Y, Shen C. Performance analysis of smartphone-sensor behavior for human activity recognition. IEEE Access. 2017;5: 3095–3110. doi: 10.1109/ACCESS.2017.2676168
39. Karantonis DM, Narayanan MR, Mathie M, Lovell NH, Celler BG. Implementation of a real-time human movement classifier using a triaxial accelerometer for ambulatory monitoring. IEEE Trans Inf Technol Biomed. 2006;10: 156–167. doi: 10.1109/TITB.2005.856864
40. Bayat A, Pomplun M, Tran DA. A study on human activity recognition using accelerometer data from smartphones. Procedia Comput Sci. 2014;34: 450–457. doi: 10.1016/j.procs.2014.07.009
41. Khan AM, Tufail A, Khattak AM, Laine TH. Activity recognition on smartphones via sensor-fusion and KDA-based SVMs. Int J Distrib Sens Netw. 2014;10: 503291. doi: 10.1155/2014/503291
42. Khan AM, Siddiqi MH, Lee S-W. Exploratory data analysis of acceleration signals to select light-weight and accurate features for real-time activity recognition on smartphones. Sensors. 2013;13: 13099–13122. doi: 10.3390/s131013099
43. Attal F, Mohammed S, Dedabrishvili M, Chamroukhi F, Oukhellou L, Amirat Y. Physical human activity recognition using wearable sensors. Sensors. 2015;15: 31314–31338. doi: 10.3390/s151229858
44. Davila JC, Cretu A-M, Zaremba M. Wearable sensor data classification for human activity recognition based on an iterative learning framework. Sensors. 2017;17: 1287. doi: 10.3390/s17061287
45. Janidarmian M, Roshan Fekr A, Radecka K, Zilic Z. A comprehensive analysis on wearable acceleration sensors in human activity recognition. Sensors. 2017;17: 529. doi: 10.3390/s17030529
46. Mehrang S, Pietilä J, Korhonen I. An activity recognition framework deploying the random forest classifier and a single optical heart rate monitoring and triaxial accelerometer wrist-band. Sensors. 2018;18: 613. doi: 10.3390/s18020613

47. Bhattacharya S, Lane ND. From smart to deep: Robust activity recognition on smartwatches using deep learning. Proceedings of the 2016 IEEE International Conference on Pervasive Computing and Communication Workshops (PerCom Workshops); 2016 Mar 14-18; Sydney, NSW, Australia. IEEE; 2016. pp. 1–6. doi: 10.1109/PERCOMW.2016.7457169
48. Ronao CA, Cho S-B. Human activity recognition with smartphone sensors using deep learning neural networks. Expert Syst Appl. 2016;59: 235–244. doi: 10.1016/j.eswa.2016.04.032
49. Nweke HF, Teh YW, Al-garadi MA, Alo UR. Deep learning algorithms for human activity recognition using mobile and wearable sensor networks: State of the art and research challenges. Expert Syst Appl. 2018;105: 233–261. doi: 10.1016/j.eswa.2018.03.056
50. Wang J, Chen Y, Hao S, Peng X, Hu L. Deep learning for sensor-based activity recognition: A survey. Pattern Recognit Lett. 2019;119: 3–11. doi: 10.1016/j.patrec.2018.02.010
51. Banos O, Galvez J-M, Damas M, Pomares H, Rojas I. Window size impact in human activity recognition. Sensors. 2014;14: 6474–6499. doi: 10.3390/s140406474
52. Dernbach S, Das B, Krishnan NC, Thomas BL, Cook DJ. Simple and complex activity recognition through smart phones. Proceedings of the 2012 Eighth International Conference on Intelligent Environments; 2012 Jun 26-29; Guanajuato, Mexico. IEEE; 2012. pp. 214–221. doi: 10.1109/IE.2012.39
53. Siirtola P, Röning J. Ready-to-use activity recognition for smartphones. Proceedings of the 2013 IEEE Symposium on Computational Intelligence and Data Mining (CIDM); 2013 Apr 16-19; Singapore, Singapore. IEEE; 2013. pp. 59–64. doi: 10.1109/CIDM.2013.6597218
54. Shoaib M, Bosch S, Incel OD, Scholten H, Havinga PJM. Fusion of smartphone motion sensors for physical activity recognition. Sensors. 2014;14: 10146–10176. doi: 10.3390/s140610146
55. Shoaib M, Bosch S, Scholten H, Havinga PJM, Incel OD. Towards detection of bad habits by fusing smartphone and smartwatch sensors. Proceedings of the 2015 IEEE International Conference on Pervasive Computing and Communication Workshops (PerCom Workshops); 2015 Mar 23-27; St. Louis, MO, USA. IEEE; 2015. pp. 591–596. doi: 10.1109/PERCOMW.2015.7134104
56. Mannini A, Intille SS, Rosenberger M, Sabatini AM, Haskell W. Activity recognition using a single accelerometer placed at the wrist or ankle. Med Sci Sports Exerc. 2013;45: 2193–2203. doi: 10.1249/MSS.0b013e31829736d6
57. Miluzzo E, Lane ND, Fodor K, Peterson R, Lu H, Musolesi M, et al. Sensing meets mobile social networks: the design, implementation and evaluation of the CenceMe application.

Proceedings of the 6th ACM Conference on Embedded Network Sensor Systems (SenSys '08); 2008 Nov 5-7; Raleigh, NC, USA. ACM; 2008. pp. 337–350. doi: 10.1145/1460412.1460445

58. Reddy S, Mun M, Burke J, Estrin D, Hansen M, Srivastava M. Using mobile phones to determine transportation modes. ACM Trans Sens Netw. 2010;6: 13. doi: 10.1145/1689239.1689243
59. Ward JA, Lukowicz P, Tröster G, Starner TE. Activity recognition of assembly tasks using body-worn microphones and accelerometers. IEEE Trans Pattern Anal Mach Intell. 2006;28: 1553–1567. doi: 10.1109/TPAMI.2006.197
60. Stiefmeier T, Roggen D, Ogris G, Lukowicz P, Tröster G. Wearable activity tracking in car manufacturing. IEEE Pervasive Comput. 2008;7: 42–50. doi: 10.1109/MPRV.2008.40
61. Joshua L, Varghese K. Accelerometer-based activity recognition in construction. J Comput Civ Eng. 2011;25: 370–379. doi: 10.1061/(ASCE)CP.1943-5487.0000097
62. Akhavian R, Behzadan AH. Smartphone-based construction workers' activity recognition and classification. Autom Constr. 2016;71: 198–209. doi: 10.1016/j.autcon.2016.08.015
63. Valero E, Sivanathan A, Bosché F, Abdel-Wahab M. Musculoskeletal disorders in construction: A review and a novel system for activity tracking with body area network. Appl Ergon. 2016;54: 120–130. doi: 10.1016/j.apergo.2015.11.020
64. Sánchez D, Tentori M, Favela J. Activity recognition for the smart hospital. IEEE Intell Syst. 2008;23: 50–57. doi: 10.1109/MIS.2008.18
65. Zhao W, Lun R, Gordon C, Fofana A-BM, Espy DD, Reinthal MA, et al. A human-centered activity tracking system: toward a healthier workplace. IEEE Trans Hum-Mach Syst. 2017;47: 343–355. doi: 10.1109/THMS.2016.2611825
66. Pierzchała M, Kvaal K, Stampfer K, Talbot B. Automatic recognition of work phases in cable yarding supported by sensor fusion. Int J For Eng. 2018;29: 12–20. doi: 10.1080/14942119.2017.1373502
67. Barnes RM. Motion and time study. 4th ed. New York: Wiley; 1958.
68. Olsen ED, Kellogg LD. Comparison of time-study techniques for evaluating logging production. Trans ASAE. 1983;26: 1665–1668. doi: 10.13031/2013.33821
69. Lortz D, Kluender R, McCoy W. Manual felling time and productivity in southern pine forests. For Prod J. 1997;47: 59–63.
70. Wang J, McNeel J, Baumgras J. A computer-based time study system for timber harvesting operations. For Prod J. 2003;53: 47–53.

71. Adebayo AB, Han H-S, Johnson L. Productivity and cost of cut-to-length and whole-tree harvesting in a mixed-conifer stand. For Prod J. 2007;57: 59–69.
72. Spinelli R, Visser R. Analyzing and estimating delays in harvester operations. Int J For Eng. 2008;19: 36–41. doi: 10.1080/14942119.2008.10702558
73. Magagnotti N, Kanzian C, Schulmeyer F, Spinelli R. A new guide for work studies in forestry. Int J For Eng. 2013;24: 249–253. doi: 10.1080/14942119.2013.856613
74. Wang J, Long C, McNeel J, Baumgras J. Productivity and cost of manual felling and cable skidding in central Appalachian hardwood forests. For Prod J. 2004;54: 45–51.
75. Spinelli R, Nati C, Magagnotti N. Using modified foragers to harvest short-rotation poplar plantations. Biomass Bioenergy. 2009;33: 817–821. doi: 10.1016/j.biombioe.2009.01.001
76. Rossit DA, Olivera A, Viana Céspedes V, Broz D. A Big Data approach to forestry harvesting productivity. Comput Electron Agric. 2019;161: 29–52. doi: 10.1016/j.compag.2019.02.029
77. Proto AR, Sperandio G, Costa C, Maesano M, Antonucci F, Macrì G, et al. A three-step neural network artificial intelligence modeling approach for time, productivity and costs prediction: a case study in Italian forestry. Croat J For Eng. 2020;41: 35–47. doi: 10.5552/crojfe.2020.611
78. Miyata ES. Determining fixed and operating costs of logging equipment. St. Paul, MN, USA: U.S. Department of Agriculture, Forest Service, North Central Forest Experiment Station; 1980. Report No.: General Technical Report NC-55. Available from: https://www.nrs.fs.fed.us/pubs/gtr/gtr_nc055.pdf
79. Brinker RW, Kinard J, Rummer R, Lanford B. Machine rates for selected forest harvesting machines. Auburn, AL, USA: Alabama Agricultural Experiment Station; 2002 Sep. Report No.: Circular 296 (revised). Available from: https://www.fs.usda.gov/treesearch/pubs/33467
80. Bolding MC, Lanford BL. Wildfire fuel harvesting and resultant biomass utilization using a cut-to-length/small chipper system. For Prod J. 2005;55: 181–189.
81. Strandgard M, Mitchell R. Automated time study of forwarders using GPS and a vibration sensor. Croat J For Eng. 2015;36: 175–184.
82. Olivera A, Visser R, Acuna M, Morgenroth J. Automatic GNSS-enabled harvester data collection as a tool to evaluate factors affecting harvester productivity in a Eucalyptus spp. harvesting operation in Uruguay. Int J For Eng. 2016;27: 15–28. doi: 10.1080/14942119.2015.1099775
83. Becker RM, Keefe RF, Anderson NM. Use of real-time GNSS-RF data to characterize the swing movements of forestry equipment. Forests. 2017;8: 44. doi: 10.3390/f8020044

84. Gallo R, Grigolato S, Cavalli R, Mazzetto F. GNSS-based operational monitoring devices for forest logging operation chains. J Agric Eng. 2013;44: 140–144. doi: 10.4081/jae.2013.269
85. McDonald TP, Fulton JP, Darr MJ, Gallagher TV. Evaluation of a system to spatially monitor hand planting of pine seedlings. Comput Electron Agric. 2008;64: 173–182. doi: 10.1016/j.compag.2008.04.011
86. Borz SA, Talagai N, Cheţa M, Gavilanes Montoya AV, Castillo Vizuete DD. Automating data collection in motor-manual time and motion studies implemented in a willow short rotation coppice. BioResources. 2018;13: 3236–3249.
87. Talagai N, Cheţa M, Gavilanes Montoya AV, Castillo Vizuete DD, Borz SA. Predicting time consumption of chipping tasks in a willow short rotation coppice from GPS and acceleration data. Proceedings of the 8th Edition of the Biennial International Symposium: "Forest and Sustainable Development"; 2018 Oct 25-27; Brașov, Romania. Transilvania University Press; 2018. pp. 1–12.
88. Cadei A, Mologni O, Proto AR, D'Anna G, Grigolato S. Using high-frequency accelerometer to detect machine tilt. Proceedings of the 19th International Scientific Conference: Engineering for Rural Development; 2020 May 20-22; Jelgava, Latvia. Latvia University of Life Sciences and Technologies; 2020. pp. 1865–1870. doi: 10.22616/ERDev2020.19.TF512
89. Bowen J, Hinze A, Cunningham SJ, Parker R. Evaluating low-cost activity trackers for use in large-scale data gathering of forestry workers. Proceedings of the Annual Meeting of the Australian Special Interest Group for Computer Human Interaction (OzCHI '15); 2015 Dec 7-10; Parkville, Australia. ACM; 2015. pp. 474–482. doi: 10.1145/2838739.2838741
90. Bowen J, Hinze A, Griffiths C. Investigating real-time monitoring of fatigue indicators of New Zealand forestry workers. Accid Anal Prev. 2019;126: 122–141. doi: 10.1016/j.aap.2017.12.010
91. Cheţa M, Marcu MV, Borz SA. Workload, exposure to noise, and risk of musculoskeletal disorders: a case study of motor-manual tree feeling and processing in poplar clear cuts. Forests. 2018;9: 300. doi: 10.3390/f9060300
92. Cheţa M, Marcu MV, Iordache E, Borz SA. Testing the capability of low-cost tools and artificial intelligence techniques to automatically detect operations done by a small-sized manually driven bandsaw. Forests. 2020;11: 739. doi: 10.3390/f11070739
93. Cheţa M, Marcu MV, Borz SA. Effect of training parameters on the ability of artificial neural networks to learn: a simulation on accelerometer data for task recognition in motor-manual

felling and processing. Bull Transilv Univ Braşov. 2020;13: 19–36. doi: 10.31926/but.fwiafe.2020.13.62.1.2

94. m_c8bit. TimeStamp. m_c8bit; 2019. Version 0.4.0. Available from: https://play.google.com/store/apps/details?id=jp.m_c8bit.timestamp
95. Dufour C. RawLogger. 2019. Version 1.0.20190520a. Available from: http://apps.garmin.com/en-US/apps/bd37beed-35e1-4ffc-a9fc-9297723d6c72
96. R Core Team. R: a language and environment for statistical computing. Vienna, Austria: R Foundation for Statistical Computing; 2020. Available from: https://www.r-project.org/
97. Liaw A, Wiener M. Classification and regression by randomForest. R News. 2002;2: 18–22.
98. Genuer R, Poggi J-M, Tuleau-Malot C. Variable selection using random forests. Pattern Recognit Lett. 2010;31: 2225–2236. doi: 10.1016/j.patrec.2010.03.014
99. Oshiro TM, Perez PS, Baranauskas JA. How many trees in a random forest? In: Perner P, editor. MLDM 2012: Machine Learning and Data Mining in Pattern Recognition; 2012 Jul 13-20; Berlin, Germany. Springer, Berlin, Heidelberg; 2012. pp. 154–168. doi: 10.1007/978-3-642-31537-4_13
100. Svetnik V, Liaw A, Tong C, Culberson JC, Sheridan RP, Feuston BP. Random Forest: A classification and regression tool for compound classification and QSAR modeling. J Chem Inf Comput Sci. 2003;43: 1947–1958. doi: 10.1021/ci034160g
101. Kuhn M. caret: classification and regression training. 2020. R package version 6.0-85. Available from: https://CRAN.R-project.org/package=caret
102. Minnen D, Westeyn T, Starner T, Ward JA, Lukowicz P. Performance metrics and evaluation issues for continuous activity recognition. Proceedings of the Performance Metrics for Intelligent Systems Workshop; 2006 Aug 21-23; Gaithersburg, MD, USA. NIST; 2006. pp. 141–148.
103. Fawcett T. An introduction to ROC analysis. Pattern Recognit Lett. 2006;27: 861–874. doi: 10.1016/j.patrec.2005.10.010
104. Hanley JA, McNeil BJ. The meaning and use of the area under a receiver operating characteristic (ROC) curve. Radiology. 1982;143: 29–36. doi: 10.1148/radiology.143.1.7063747
105. Bradley AP. The use of the area under the ROC curve in the evaluation of machine learning algorithms. Pattern Recognit. 1997;30: 1145–1159. doi: 10.1016/S0031-3203(96)00142-2
106. Weiss GM, Provost F. Learning when training data are costly: the effect of class distribution on tree induction. J Artif Intell Res. 2003;19: 315–354. doi: 10.1613/jair.1199

107. Boughorbel S, Jarray F, El-Anbari M. Optimal classifier for imbalanced data using Matthews Correlation Coefficient metric. PLoS ONE. 2017;12: e0177678. doi: 10.1371/journal.pone.0177678
108. Luque A, Carrasco A, Martín A, de las Heras A. The impact of class imbalance in classification performance metrics based on the binary confusion matrix. Pattern Recognit. 2019;91: 216–231. doi: 10.1016/j.patcog.2019.02.023
109. Robin X, Turck N, Hainard A, Tiberti N, Lisacek F, Sanchez J-C, et al. pROC: an open-source package for R and S+ to analyze and compare ROC curves. BMC Bioinformatics. 2011;12: 77. doi: 10.1186/1471-2105-12-77
110. Hand DJ, Till RJ. A simple generalisation of the area under the ROC curve for multiple class classification problems. Mach Learn. 2001;45: 171–186. doi: 10.1023/A:1010920819831
111. Liang Y, Zhou X, Yu Z, Guo B. Energy-efficient motion related activity recognition on mobile devices for pervasive healthcare. Mob Netw Appl. 2014;19: 303–317. doi: 10.1007/s11036-013-0448-9
112. Rehman MH ur, Liew CS, Wah TY, Shuja J, Daghighi B. Mining personal data using smartphones and wearable devices: a survey. Sensors. 2015;15: 4430–4469. doi: 10.3390/s150204430
113. Figo D, Diniz PC, Ferreira DR, Cardoso JMP. Preprocessing techniques for context recognition from accelerometer data. Pers Ubiquitous Comput. 2010;14: 645–662. doi: 10.1007/s00779-010-0293-9
114. Erdaş ÇB, Atasoy I, Açıcı K, Oğul H. Integrating features for accelerometer-based activity recognition. Procedia Comput Sci. 2016;98: 522–527. doi: 10.1016/j.procs.2016.09.070
115. Bell CK, Keefe RF, Fried JS. Validation of the OpCost logging cost model using contractor surveys. Int J For Eng. 2017;28: 73–84. doi: 10.1080/14942119.2017.1313488
116. Scott JJ, Rowlands AV, Cliff DP, Morgan PJ, Plotnikoff RC, Lubans DR. Comparability and feasibility of wrist- and hip-worn accelerometers in free-living adolescents. J Sci Med Sport. 2017;20: 1101–1106. doi: 10.1016/j.jsams.2017.04.017

Conclusion

The use of real-time positioning information available from global navigation satellite system - radio frequency (GNSS-RF) devices and data from wearable sensors offers opportunities for improving occupational safety in forestry. Geofences are an important component of GNSS-RF location sharing systems and can alert workers of jobsite hazards. Results from Chapter 2 indicated that the angle of approach among geofences affects the timing of associated alerts. The field experiment and simulation showed that alert latency was closest to 0 s when a mobile geofence approached a stationary geofence or point of interest straight on (i.e., at a 0° angle). When the mobile geofence approached alongside a stationary point or geofence (i.e., at a 90° angle), the delay decreased, meaning that an earlier alert was triggered. This effect appears to result from the relationship between the angle of approach and the proportion of possible GNSS error directions that can trigger early warnings. This suggests that the accuracy of geofence alerts varies as worker or equipment positions move around one another at different angles, which has important implications for using geofences to define safe work areas on logging operations. Future work should focus on developing correction methods that account for the effect of intersection angle. While our results did not show a significant effect of either walking pace or GNSS-RF transmission interval, future work advancing the use of mobile geofences should consider integrating these factors into potential correction methods. For example, in practice, early warning thresholds may be established by integrating approach angle correction methods, pace, transmission interval, and GNSS location in order to provide equipment operators or ground workers with sufficient time to slow down or change course. Thus, while uncorrected mobile geofences may be useful for increasing general situational awareness (SA) among workers at coarse spatial scales, they are not advised for delineating safe work areas at high resolution unless correction methods are applied.

GNSS-RF accuracy depends on both the GNSS positioning quality and the successful propagation of radio signals between devices. To address this, in Chapter 3 we evaluated the effects of forest stand characteristics, topography, and line-of-sight (LOS) obstructions on 1) the odds of missed signals sent between Atlas PT GNSS-RF devices; 2) the root mean squared error (RMSE) of Atlas PTs; and 3) the time-to-signal accuracy of safety geofence crossings in forests. Results from this chapter showed that stand characteristics, topography, and LOS obstructions affected the odds of missed radio signals. Only stand characteristics affected RMSE and both stand and topographic variables affected the accuracy of geofence alerts. This suggests that the accuracy and successful sharing of GNSS coordinates depends on stand conditions and topography. Because both of these

characteristics vary on active timber sales, high-resolution safety applications of consumer-grade GNSS-RF devices such as geofencing are not yet advisable in mature forests. However, utilizing this technology on logging operations may allow ground workers and equipment operators to view the relative positions of nearby workers and machines in real-time to improve general SA and communication. In order to advance the use of GNSS-RF real-time positioning for additional safety applications in natural resources, future research should develop and assess methods that correct for the effects of forest stand characteristics on both GNSS accuracy and geofence alert delay. One important consideration regarding Chapter 3 is that the Atlas PT GNSS-RF devices only receive coordinates from Global Positioning System (GPS) satellites while many newer devices communicate with multiple satellite constellations, which may improve accuracy and reliability in forests. Ultimately, correction methods that account for stand characteristics and geofence intersection angle, as well as the use of multi-constellation GNSS-RF devices, may enable a broader range of GNSS-RF safety applications in natural resources.

While conventional GNSS-RF positioning relies on direct LOS connection between radios, mesh networking allows each device in the network to relay data to other nodes, enabling communication between users who do not have a direct LOS connection. The recent development of Bluetooth-based devices that form GNSS-RF mesh networks when paired with smartphones offers new opportunities to facilitate real-time location- and data-sharing in off-grid forested environments. In Chapter 4, I developed Dirichlet regression models to predict the connectivity of goTenna smartphone-based mesh networks using lidar- and satellite-derived terrain and vegetation metrics in order to determine the factors affecting connectivity and to evaluate overall network performance across a range of forest and topographic conditions. On average the full network was connected only 32.6% of the time and the mobile goTenna was disconnected from all other devices 18.2% of the time. Vegetation-related metrics affected connectivity more than topography in all final models, which was a somewhat unexpected result. One potential explanation for this may be that using a network of six devices in sections that were approximately 260 ha in size overcame significant radio signal attenuation due to topography. Future work should consider how connectivity may depend on the number of devices and study area size. The models developed in Chapter 4 could be used to predict connectivity beyond the study area using lidar and satellite remote sensing data in order to provide information regarding the expected performance of these networks. Ultimately, this technology has a range of applications in wildland firefighting, forestry, natural resources, and public safety by enabling communication in remote settings where traditional infrastructure is absent.

In addition to real-time positioning utilizing GNSS-RF systems and geofences, wearable sensor data offers additional opportunities for monitoring the current activities, safety status, and location of individuals relative to workplace hazards. In Chapter 5, we used random forest machine learning to develop smartwatch-based activity recognition models for rigging crew workers on cable logging operations. We showed that these models could predict choker setter work activities with sensitivity values ranging from 76.95% to 83.59% and precision values ranging from 41.42% to 97.08%. Our results also showed that these models could predict chaser work activities with sensitivity values ranging from 71.95% to 82.75% and precision values ranging from 14.74% to 99.16%. In order to advance the development of wearable-based human activity recognition modeling for occupational safety, future studies should consider quantifying individual productive cycle elements separately from the overall productive and delay components of work. This may impact the interpretation of real-time summaries of work and the analysis of worker health and safety metrics. Additional considerations for future work include utilizing video recording of worker activities to overcome visibility issues when sampling in settings common on cable logging operations as well as coding predictive models into a smartwatch application to support real-time characterization of work activities. This application could facilitate the collection of independent datasets to further validate model predictions in a variety of site conditions. This study is among the first to demonstrate the feasibility of quantifying forestry work activities using smartwatch-based human activity recognition. Ultimately, the future pairing of activity recognition model predictions, personal health metrics such as sleep activity, heart rate, and heat stress, and real-time location sharing could foster the development of real-time smart safety notifications associated with high-risk job functions.

GNSS-RF real-time positioning, geofencing, mesh networking, and wearable-based human activity recognition modeling are emerging technologies that provide a range of opportunities for increasing the safety, efficiency, and productivity of forestry and natural resource professionals through increased situational awareness. Together with the widespread availability of remote sensing and big data in forestry, these mobile technologies represent aspects of smart forestry and enable advances in digitalization and automation as well as improved precision. The work presented in this dissertation provides an assessment of the factors affecting the performance and accuracy of a variety of location sharing networks and demonstrates the feasibility of using wearable sensors to quantify forestry work activities. In the case of smartwatch-based human activity recognition and closely related smartphone-based activity recognition not included in the dissertation, these contributions represent the first uses of human activity recognition in natural resources for smartwatch and smartphone devices, respectively. Integrating real-time positioning with activity recognition model

predictions has strong potential to improve occupational safety in off-grid forested environments and to advance the way fundamental work tasks in forestry are quantified and evaluated, opening new possibilities for analyzing big data related to health and safety that is accumulated over time through longitudinal surveillance. For this reason, the methodologies presented in this work contribute to both near-term solutions to reduce incidents, such as real-time safety alerts for lone forestry workers, and the creation of long-term surveillance data that can be used to identify longitudinal and population-level health and safety trends at resolutions and scales not previously possible.

Appendix A: Lidar Metrics for Chapter 4

Table A.1. Lidar DEM-, point cloud-, and voxel-derived metrics. RT: all = all vegetation returns ≥ 0.27 m; first = first vegetation returns ≥ 0.27 m; last = last vegetation returns ≥ 0.27 m

Variable	Description	Source	Classification
DEM-based			
Rumple_index	DEM was used to calculate a rumple index for each section using the rumple_index function in the R lidR package (Roussel and Auty 2021)	DEM	Topography
SRR	DEM was used to calculate the surface relief ratio (SRR) for the entirety of each section as: (mean(x) - min(x)) / (max(x) - min(x)), where x represents the DEM elevation values (Pike and Wilson 1971)	DEM	Topography
Slope_Mean and Slope_SD	DEM was used to create slope rasters for each section in degrees using eight neighbors using the terrain function in the R terra package (Hijmans 2021), then the mean and standard deviation of these rasters were calculated for each section	DEM	Topography
TPI_Mean and TPI_SD	DEM was used to create topographic position index (TPI) rasters for each section using the terrain function in the R terra package (Hijmans 2021), then the mean and standard deviation of these rasters were calculated for each section. TPI is the difference between the value of a cell and the mean value of its eight surrounding cells (Weiss 2001; Wilson et al. 2007; Hijmans 2021)	DEM	Topography
TRI_Mean and TRI_SD	DEM was used to create terrain ruggedness index (TRI) rasters for each section using the terrain function in the R terra package (Hijmans 2021), then the mean and standard deviation of these rasters were calculated for each section. TRI is the mean of the absolute differences between the value of a cell and the value of its eight surrounding cells (Wilson et al. 2007; Hijmans 2021)	DEM	Topography
Rough_Mean and Rough_SD	DEM was used to create roughness rasters for each section using the terrain function in the R terra package (Hijmans 2021), then the mean and standard deviation of these rasters were calculated for each section. Roughness is the difference between the maximum and the minimum value of a cell and its eight surrounding cells (Wilson et al. 2007; Hijmans 2021)	DEM	Topography
Flow_Mean and Flow_SD	DEM was used to create flow direction (of water) rasters for each section using the terrain function in the R terra package (Hijmans 2021), then the mean and standard deviation of these rasters were calculated for each section. Flow direction is the direction of the greatest drop in elevation (or the smallest rise if all neighbors are higher) (Hijmans 2021)	DEM	Topography

HSP_Mean and HSP_SD	DEM was used to create hierarchical slope position (HSP) rasters for each section using the hsp function in the R spatialEco package (Evans 2021), then the mean and standard deviation of these rasters were calculated for each section. HSP is the hierarchical scale decomposition of the topographic position index and was calculated using rectangular windows ranging in size from 3 cells to 27 cells in 4-cell increments (Murphy et al. 2010; Evans 2021)	DEM	Topography
Curv_Mean and Curv_SD	DEM was used to create McNab's curvature rasters for each section using the curvature function in the R spatialEco package (Evans 2021), then the mean and standard deviation of these rasters were calculated for each section. This is a variant of the surface curvature (concavity/convexity) index and is confined to the view of a 3 x 3 window (McNab 1989; Evans 2021)	DEM	Topography
HLI_Mean and HLI_SD	DEM was used to create heat load index (HLI) rasters for each section using the hli function in the R spatialEco package (Evans 2021), then the mean and standard deviation of these rasters were calculated for each section. This function calculates the McCune and Keon 2002 heat load index which estimates potential annual direct incident radiation (McCune and Keon 2002; Evans 2021)	DEM	Topography
Diss_Mean and Diss_SD	DEM was used to create dissection rasters for each section using a window size of three and the dissection function in the R spatialEco package (Evans 2021), then the mean and standard deviation of these rasters were calculated for each section. This function calculates Martone's modified dissection (Evans 1972, 2021)	DEM	Topography
CHM-based			
rumple_index_chm	Point cloud was used to create a 0.5 m pit-free canopy height model (CHM) using the lidR grid_canopy function, using only first vegetation returns ≥ 0.27 m in height. The lidR rumple_index function was then used with the resulting CHM to calculate a rumple index for the canopy (Roussel and Auty 2021)	CHM	Height
Point cloud-based			
pground_veg27	Percentage of returns classified as "ground" calculated using the lidR cloud_metrics function using all vegetation returns ≥ 0.27 m (Roussel and Auty 2021)	Point cloud	Point density
LAD_x_RT	lidR LAD function was used to calculate leaf area density using 1 m height bins (x = 2.5, 3.5, 4.5, …, 30.5 m) for a given return type (RT = all, first, last) (Roussel and Auty 2021)	Point cloud	Point density
Point cloud-based, calculated using std_cloud function from Blackburn et al. (Blackburn 2021; Blackburn et al. 2021)			
per_RN_x_RT	Percent of points from a given return number (x = return numbers 1–7) and return type (RT = all, last) (Blackburn et al. 2021)	Point cloud	Point density

zstat_RT	Height-based descriptive statistics of the point cloud within a section for a given return type (RT). Statistics (stat) = max, mode, mean, quadratic mean, standard deviation, variance, coefficient of variation, IQR, average absolute deviation, skewness, kurtosis, entropy, L-Moments (2-4), L-moment skewness, and L-moment kurtosis. RT = all, first (except for max), last (except for mode) (Blackburn et al. 2021)	Point cloud	Height
qHt_x_RT	Height quantiles (x = 1, 5, 10, 15, 20, 25 …, 95, 99) for a given return type (RT = all, first, last) (Blackburn et al. 2021)	Point cloud	Height
decilex_RT	Deciles (x = 2, 3, …, 9) for height distributions within a section for a given return type (RT = all, first, last) (Woods et al. 2008; Pearse et al. 2019; Blackburn et al. 2021)	Point cloud	Height
dcumx_RT	Cumulative deciles (x = 1, 2, …, 9) for height distributions within a section for a given return type (RT = all, first, last) (Woods et al. 2008; Pearse et al. 2019; Blackburn et al. 2021)	Point cloud	Height
pHtBin_x_RT	Percent of points within height bins (x = ≤ 5, 5-10, 10-15, 15-20, …, > 50) for a given return type (RT = all, first, last) (Pearse et al. 2019; Blackburn et al. 2021)	Point cloud	Point density
pz_1r_RT	Percent of first returns above a given height (z = 2m, 10m, 20m, mean height, mode height) for a given return type (RT = all, last [except for percent above mode height]) (Blackburn et al. 2021)	Point cloud	Point density
pz_RT	Percent of all returns above a given height (z = 2m, 10m, 20m, mean height, mode height) for a given return type (RT = all, first, last [except for percent above mode height]) (Blackburn et al. 2021)	Point cloud	Point density
istat_RT	Intensity-based descriptive statistics of the point cloud within a section for a given return type (RT). Statistics (stat) = total, min, mean, quadratic mean, standard deviation, variance, coefficient of variation, IQR, average absolute deviation, skewness, kurtosis, and entropy. RT = all, first, last (Blackburn et al. 2021)	Point cloud	Intensity
icum_qHt_x_RT	Cumulative intensity returned below quantiles (x = 1, 5, 10, 15, 20, 25 …, 95, 99) for a given return type (RT = all, first, last) (Blackburn et al. 2021)	Point cloud	Intensity
LCV_RT	Coefficient of L-variation for a given return type (RT = all, first, last). Calculated as: LCV = second L-moment of heights / first L-moment of heights	Point cloud	Height
Voxel-based, calculated using std_voxel and vox_mt functions from Blackburn et al. (Blackburn 2021; Blackburn et al. 2021)			
z_ s1_s2_res	Height-based descriptive statistics within a voxel (s1) and summarized at the section level (s2) for a given resolution (res = 3m, 4m, 5m). Statistics (s1 and s2) = median, mean, variance, standard deviation, coefficient of variation, IQR, skewness, and kurtosis (Pearse et al. 2019; Blackburn et al. 2021)	Voxel	Height

i_s1_s2_res	Intensity-based descriptive statistics within a voxel (s1) and summarized at the section level (s2) for a given resolution (res = 3m, 4m, 5m). Statistics (s1 and s2) = median, mean, variance, standard deviation, coefficient of variation, IQR, skewness, and kurtosis (Pearse et al. 2019; Blackburn et al. 2021)	Voxel	Intensity
P_Di_s2_res	Section-level descriptive statistics (s2) of the number of returns below each voxel for a given resolution (res = 3m, 4m, 5m). Statistics (s2) = median, mean, variance, standard deviation, coefficient of variation, IQR, skewness, and kurtosis (Pearse et al. 2019; Blackburn et al. 2021)	Voxel	Point density
npoints_above_s2_res	Section-level descriptive statistics (s2) of the number of returns above each voxel for a given resolution (res = 3m, 4m, 5m). Statistics (s2) = mean, variance, standard deviation, coefficient of variation, IQR, skewness, and kurtosis (Kim et al. 2016; Blackburn et al. 2021).	Voxel	Point density
FR_Di_s2_res	Section-level descriptive statistics (s2) for the frequency ratio of the number of returns above a voxel to the total returns for a given resolution (res = 3m, 4m, 5m). Statistics (s2) = mean, variance, standard deviation, and IQR (Kim et al. 2016; Pearse et al. 2019; Blackburn et al. 2021)	Voxel	Point density
pct_fill_vox_res	Percent of voxels with at least one point in the section for a given resolution (res = 3m, 4m, 5m) (Blackburn et al. 2021)	Voxel	Point density
ENL_HN_res	Effective number of layers (ENL) measured through different Hill-Numbers (HN = 0D, 1D, 2D) for a given resolution (res = 3m, 4m, 5m) to quantify vertical structure (Ehbrecht et al. 2016; Pearse et al. 2019; Blackburn et al. 2021). Computing ENL consists of classifying voxels as empty/not empty and then calculating various diversity indices based on the proportion of filled voxels in each layer in relation to all filled voxels (Ehbrecht et al. 2016; Pearse et al. 2019)	Voxel	Point density
cc_abovez_res	Canopy closure at different heights based on the percentage of empty voxels above different heights for a given resolution (res = 3m, 4m, 5m) (Pope and Treitz 2013; Pearse et al. 2019; Blackburn et al. 2021). Height thresholds for 3-m resolution (z) = 3, 6, 9, ..., 24 m. Height thresholds for 4-m resolution (z) = 4, 8, 12, ..., 24 m. Height thresholds for 5-m resolution (z) = 5, 10, 15, 20, 25 m.	Voxel	Point density
p_cc_res	Mean percentage canopy closure based on the ratio of height bin point density to the overall point density within a section for a given resolution (res = 3m, 4m, 5m) (Griffin et al. 2008; Pearse et al. 2019; Blackburn et al. 2021). Height bins for 3-m resolution = 1, 3, 6, 9, …, 21 m. Height bins for 4-m resolution = 1, 4, 8, 12, 16, 20 m. Height bins for 5-m resolution = 1, 5, 10, 15, 20 m	Voxel	Point density